creative commons

COMMONS DEED

저작자표시-비영리-동일조건변경허락 2.0 대한민국

이용자는 아래의 조건을 따르는 경우에 한하여 자유롭게

- 이 저작물을 복제, 배포, 전송, 전시, 공연 및 방송할 수 있습니다.
- 이차적 저작물을 작성할 수 있습니다.

다음과 같은 조건을 따라야 합니다:

저작자표시. 귀하는 원저작자를 표시하여야 합니다.

비영리. 귀하는 이 저작물을 영리 목적으로 이용할 수 없습니다.

동일조건변경허락. 귀하가 이 저작물을 개작, 변형 또는 가공했을 경우에는, 이 저작물과 동일한 이용허락조건하에서만 배포할 수 있습니다.

- 귀하는, 이 저작물의 재이용이나 배포의 경우, 이 저작물에 적용된 이용허락조건을 명확하게 나타내어야 합니다.
- 저작권자로부터 별도의 허가를 받으면 이러한 조건들은 적용되지 않습니다.

저작권법에 따른 이용자의 권리는 위의 내용에 의하여 영향을 받지 않습니다.

이것은 이용허락규약(Legal Code)을 이해하기 쉽게 요약한 것입니다.

Disclaimer

dCollection

Doctoral Thesis

A Study on the Surface State of Catalytic Chemistry Using First-Principles calculation

Yongchul Kim

Department of Chemistry

Ulsan National Institute of Science and Technology

2023

A Study on the Surface State of Catalytic Chemistry Using First-Principles calculation

Yongchul Kim

Department of Chemistry

Ulsan National Institute of Science and Technology

A Study on the Surface State of Catalytic Chemistry Using First-Principles calculation

A thesis/dissertation submitted to
Ulsan National Institute of Science and Technology
in partial fulfillment of the
requirements for the degree of
Doctor of Philosophy

Yongchul Kim

11.30.2022 of submission
Approved by

Advisor
Geunsik Lee

A Study on the Surface State of Catalytic Chemistry Using First-Principles calculation

Yongchul Kim

This certifies that the thesis/dissertation of Yongchul Kim is approved.

11.30.2022 of submission

Signature

Advisor: Geunsik Lee

Signature

Kwang Soo Kim

Kwang S. Kim: Thesis Committee member #1

Signature

Rodney Ruoff: Thesis Committee member #2

Signature

Seung Kyu Min: Thesis Committee member #3

Signature

Myung Jong Kim: Thesis Committee member #4

Abstract

A catalyst refers to that accelerates a chemical reaction without being consumed during the chemical reactions. This property is usually referred to as the catalytic activity. For a multi-step chemical reaction with multiple possible products, a catalyst can promote the production of a specific chemical compound, which is related to the rate-determining step of the reaction. Heterogeneous catalytic reactions mainly occur on the surface of solid catalysts with accompanying elementary surface chemical processes such as adsorption of reactants from a reaction mixture, surface diffusion and reaction of adsorbed species, and desorption of reaction products. The promotion of a chemical reaction is originated from the high reactivity of surface atoms that facilitates bond breaking and bond rearrangement of adsorbed molecules. In order to increase the yield of a desired reaction, the demand for catalysts showing high activity is growing throughout modern industries. Beyond simple chemical reactions, the complex and multi-step reactions have been important in various fields that require effective catalyst. However, research is needed in many cases to understand the detailed bond rearrangement of the reaction on the catalyst surface or the diffusion or dissolution process of the interface. As the demand for catalyst design or material synthesis increases, the first-principles calculations are required to understand a detailed catalysis.

One area where catalyst is highly required is hydrogen production. As the use of fossil fuels increases, the world faces a climate crisis due to carbon dioxide emissions, and as a promising substitute for fossil fuels, hydrogen has emerged as a clean and renewable energy. In particular, green hydrogen production without CO_2 emission can be achieved through electrocatalytic water splitting. In water splitting reactions, the commercial electrocatalysts composed of rare metals such as Ir, Pt and Ru has a problem with their price. Besides, sluggish multi-step oxygen evolution reaction (OER) is another hindrance for efficient water splitting. To overcome these problems, development of cheap electrocatalysts with high performance is necessary. First-principles calculations using density functional theory (DFT) has been used to describe and predict the intrinsic activity of catalysts. The adsorption energies of intermediates determine the activity of the catalyst. The surface electronic structure is highly correlated with intermediate species adsorption energies which determine the catalytic activity.

In Chapter 2, we investigated the influence of cation mixing on the oxygen evolution reaction (OER) activity of $La_xSr_{1-x}Co_yFe_{1-y}O_3$ (LSCF) double perovskite in the perspective of surface electronic structure. Based on projected density of states and wavefunction analysis, the minority spin d_{xy} electrons of surface layer metal atoms are significant due to their stability, where the antibonding states between d_{xy} and the lattice oxygen p become occupied when Co atoms with one d electron more than Fe are

present. Thus, by additionally considering the d_{xy} band center, surface electronic descriptor ($E_{2p} - 0.4 E_{dxy}$) excellently describes the binding energy of the OER intermediates and the stability against oxygen vacancy formation, which also explains the enhanced OER stability and efficient Fe–Co mixing. Based on the computational analysis, several efficient perovskite electrocatalysts were presented, and it was confirmed that the electronic structure analysis could provide guidance for electrocatalysts design.

Another area in which catalysts play an important role, is the synthesis and etching of low-dimensional carbon materials through the 3d transition metal surface. Graphene is produced from amorphous sp^3 carbon through Ni junction, and the surface of diamond is etched under high-temperature conditions. In order to control these interfacial reactions, accurate understanding and mechanism analysis are required, and detailed bond dissociation and forming processes can be identified through first-principles DFT simulations.

In Chapter 3, we analyze the kinetics of dissolution of single crystal diamond (100) and (110), “D(100)” and “D(110)”, into thin films of nickel (Ni) and cobalt (Co). This dissolution occurs at the metal-D(100) or metal-D(110) interface and was studied in the presence and also absence of water vapor at temperatures near 1000 °C. Based on the first-principles calculation, the mechanism of why the diamond surface carbon can diffuse through Ni or Co despite the low activation energy of the reverse reaction were unveiled.

Contents

Abstract .... **i**

Contents .... **iv**

List of Figures .... **vi**

List of Tables .... **xiv**

I. Introduction **1**

- 1.1 General Information 1
    - 1.1.1 Water Splitting for Hydrogen Production 1
    - 1.1.2 Carbon Control for Material Synthesis 3
- 1.2 DFT simulations for OER Electrocatalysts 4
    - 1.2.1 Computational Standard Hydrogen Electrode 4
    - 1.2.2 Electrochemical Half-Reaction of Water Splitting, OER 4
    - 1.2.3 OER Electrolysis on Perovskite Oxide 6
- 1.3 Carbon Control via Metal Surface 8
    - 1.3.1 Carbon Diffusion 8
    - 1.3.2 Growth of Carbon 9
- 1.4 Outline of Dissertation 11
- 1.5 References 12

II. Theoretical Investigation for Rational Design of the OER Elecatalysts **14**

- 2.1 Introduction 14
- 2.2 Methods 15
    - 2.2.1 Calculation Information 15
    - 2.2.2 Explicit Solvent and Minima Hopping Methods 16
- 2.3 Results and Discussion 18
    - 2.3.1 OER Mechanism and Intermediates Binding Strength 18
    - 2.3.2 Correlation of Surface Electronic Structure and Surface Stability 22
    - 2.3.3 Descriptor ($E_{2p} – 0.4\ E_{dxy}$) 26
    - 2.3.4 OER activity and Electrocatalyst Design 30
- 2.4 Conclusion 37
- 2.5 References 38

III. DFT Simulation for the Interface Carbon Diffusion **42**

- 3.1 Introduction 42
- 3.2 Methods 43

3.3 Results and Discussion 44
3.3.1 Experimental Findings 44
3.3.2 Theoretical Modeling of Reaction Pathways and Potential Energy Barriers 48
3.3.3 Surface Exchange Mechanism 55
3.4 Conclusion 57
3.5 References 58

IV. Summary **61**

Appendix

Acknowledgements **62**
List of Publications **63**

List of Figures

Figure 1.1 Yearly evolution and percentage distribution of publications from 2000 to date containing terms ‘‘hydrogen’’ AND ‘‘storage’’ AND ‘‘material’’, ‘‘hydrogen’’ AND ‘‘energy storage system’’ NOT ‘‘tank’’, ‘‘hydrogen’’ AND ‘‘power-to-gas’’, ‘‘hydrogen’’ AND ‘‘transportation’’, ‘‘hydrogen’’ AND (‘‘co-generation’’ OR ‘‘tri-generation’’). The search was made on the 2th June 2020.Copyright © 2021 M. Yue et al. Published by Elsevier Ltd.[4]

Figure 1.2 Yearly evolution and percentage distribution of publications from 2000 to date containing terms ‘‘hydrogen’’ AND (‘‘cost’’ OR ‘‘economy’’), ‘‘hydrogen’’ AND ‘‘efficiency’’, ‘‘hydrogen’’ AND (‘‘durability’’ OR ‘‘lifetime’’ OR ‘‘degradation’’). The search was made on the 2th June 2020. Copyright © 2021 M. Yue et al. Published by Elsevier Ltd.[4]

Figure 1.3 L. P. Ding et al. reveal the fundamental aspect of the CNT-catalyst interface, viz., that the interfacial energy of the CNT−catalyst edge is contact angle-dependent. This angle dependence can give a rationale why the CNTs grow.[5] Copyright © 2022 American Chemical Society.

Figure 1.4 (a) Hydrogen evolution reaction (HER) and oxygen evolution reaction (OER) of electrocatalytic water splitting and (b) Schematic representation of HER and OER overpotentials.[11] Copyright © 2021 Published by Elsevier B.V.

Figure 1.5 Conceptual illustration of concerted four step adsorbate evolution reaction (AEM) mechanism.

Figure 1.6 In Ni-based perovskite, schematic illustration of the competition between the Adsorbate Evolution Mechanism (AEM) and Lattice-Oxygen Participation Mechanism (LOM).[14] Copyright © 2018 American Chemical Society.

Figure 1.7 Illustration of C dissolution at the interstitial (a) O-site and (b) T-site in bulk Ni. Large balls denote Ni atoms and small balls denote C atoms.[15] Copyright © 2006 Elsevier Ltd.

Figure 1.8 Some 3d transition metals can induce layer exchange to turn amorphous carbon into graphene.[20] Copyright © 2018 American Chemical Society

Figure 1.9 (a,b) Schematic representations of growth of CNWs. (c) AFM image of bare Cu (111) surface. (d, e) SEM images of CNWs deposited at -1.25 V for (d) 0.5 h and (e) 5h.[7] Copyright © 2022 Elsevier Ltd.

Figure 1.10 (a) The optimized structure of the Cu(111) with a two-atom step running along the <110> slip direction; (b) The optimized structure of the first carbon atom adsorbed at an edge of the step and the lower terrace; The optimized structures following (c1 and d1) in-plane carbon growth or (c2 and d2) vertical carbon growth; (e) Calculated formation energy per carbon atom according to equations (1) and (2). (Each step shown corresponds to these structures: a, b, c1, d1, c2, d2).[7] Copyright © 2022 Elsevier Ltd.

Figure 2.1 Rock-salt ordered slab model of $La_{0.5}Sr_{0.5}Co_{0.5}Fe_{0.5}O_3$. *A*- and *B*-site are described as highly isotropic chemical environment. Copyright © 2022 American Chemical Society.

Figure 2.2 Optimized $LaCoO_3$ structure with the explicit solvent. The explicit water molecule initial positions were given by atomic simulation environment (ASE) package global optimization. *OH and *OOH intermediate form hydrogen bond with water molecule. The different colors indicate each atom (La = white, Co = blue, O = red, intermediate O = green, H = pink). Copyright © 2022 American Chemical Society.

Figure 2.3 According to the R. Jacob. report, catalytic activity of perovskite correlates with bulk oxygen p-band center. Reprinted from ref. 15. Copyright © 2019, American Chemical Society.

Figure 2.4 Calculated binding energies of HO* (ΔE_{OH}) and O* (ΔE_{O}) on the (001) surface as a function of O p-band center for $La_xSr_{1-x}Co_yFe_{1-y}O_3$ with x, y = 0.0, 0.5, or 1.0. The color of the symbols indicates the species of the active metal site (red = Fe and blue = Co). The binding energies of *A*FeO_3 (*A*F) and *A*CoO_3 (*A*C) are represented with open circles, where the mixed case (y = 0.5) are denoted by upward- and downward-facing triangles. Both of notation *A*CF and *A*FC represent *A*$Co_{0.5}Fe_{0.5}O_3$ composition, the last abbreviation alphabet (C or F) indicates the active *B*-site element. Copyright © 2022 American Chemical Society.

Figure 2.5 The PDOS of the minority spin d_{yz} and d_{xy} orbitals of the active metal site for La*B*O_3 before (Clean) and after adsorption of O (O*), which are represented by the dashed and solid lines, respectively. Copyright © 2022 American Chemical Society.

Figure 2.6 The $d_{yz/xz}$ minority spin projected band of $LaCoO_3$ and $LaFeO_3$ for clean surface and O*. In order to show some band characters, the wavefunctions of several representative bands related to d_{yz} at the Γ point are also shown in left of each band. The abbreviation capital alphabet represents L = La, C = Co, F = Fe, respectively. The band of the entire slab is shown in gray, active site $d_{yz/xz}$ and the surface oxygen band are shown in blue and black, respectively. After O was adsorbed to the surface, the band of intermediate O was shown in red. The wavefunction of each band shows that $d_{yz/xz}$ mainly forms a surface state before intermediate adsorption and mainly forms π bond with O after the adsorption. In O*, $d_{yz/xz}$ formed wavefunctions that mainly overlaps with O intermediate states, and it can be seen that it makes π-, π^*-bond. Bonding wavefunction is indicated by a solid box, and antibonding is indicated by a dashed box. Copyright © 2022 American Chemical Society.

Figure 2.7 (Top) Orbital configurations of *A*CoO_3 and *A*FeO_3 for clean and O*. Before O intermediate adsorbed, the clean surface has C_{4v} symmetry. The blue arrow indicates the additional electron in Co active site compared with Fe active site. The gray arrows represent the other electron from *B* metal and red arrows indicate the electrons from intermediate O. The black dashed arrow shows the variation of electron number from Sr to La *A*-site substitution. (Bottom) The PDOSs after O adsorption are presented only for the minority spin $d_{yz/xz}$ (light blue sold line) or d_{xy} (red solid line) orbitals in π hybridization with $p_{x/y}$ of the adsorbate or surface-layer O, respectively, where the vertical dashed line denotes the Fermi level (E_F) shifting rightward upon changing Sr to La, with the occupied states denoted by filled color for La*B*O_3.

Figure 2.8 The d_{xy} minority spin projected band of $LaCoO_3$ and $LaFeO_3$ for clean surface and O*. Except that d_{xy} is expressed in green, the other notation and color is the same as in Figure 2.6. Through the wavefunction images, dxy electrons form a bond with surface oxygen, and it can be seen that there is almost no overlap with O intermediate states (red projected band). Copyright © 2022 American Chemical Society.

Figure 2.9 Schematic illustration of surface d_{xy} projected DOS of $LaCoO_3$ with its wavefunction image. The wavefunction image near the Fermi level shows that d_{xy} and intermediate O of the active site metal have no overlap (which means non-bonding), and that d_{xy} mainly has antibonding character with surface lattice oxygen. Since the d_{xy} has the antibonding character with surface lattice oxygen, additional electron in Co active site can affect to the surface stability and the intermediate binding strength even though the d_{xy} doesn't form bonding nor antibonding with intermediate species.

Figure 2.10 The binding energies of HO* and O* as in Figure 2.4 plotted against a new descriptor ($E_{2p} - 0.4\ E_{dxy}$). The color of the symbols indicates the species of the active metal site (red = Fe and blue = Co). The binding energies of *A*FeO_3 (*A*F) and *A*CoO_3 (*A*C) are represented with open circles, where the mixed case (y = 0.5) are denoted by upward- and downward-facing triangles. Both of notation *A*CF and *A*FC represent *A*$Co_{0.5}Fe_{0.5}O_3$ composition, the last abbreviation alphabet (C or F) indicates the active *B*-site element. Copyright © 2022 American Chemical Society.

Figure 2.11 (a) Surface structure of the second reaction step (O*) in AEM (upper image) and O vacancy involved surface structure with adsorbate O (V_O+OO*) in LOM (lower image). The green balls represent the adsorbate O and associated lattice O. (b) Correlation between the newly suggested descriptor ($E_{2p} - 0.4\ E_{dxy}$) and the Gibbs free energy difference $\Delta G = G_{V_O+OO*} - G_{O*}$ of V_O+OO* and O* for *AB*O_3 without (open circle) or with (upper and lower triangle) Fe–Co mixing for the *B*-site. The blue and red colors denote Co and Fe for the active site metal, respectively. The variation of ΔG with the *A*-site composition, such as x = 0.0, 0.5, and 1.0 for La_xSr_{1-x}, follows the lines with the associated color for the active site type. AEM is favored for a more positive value of ΔG ($G_{V_O+OO*} - G_{O*}$). Copyright © 2022 American Chemical Society.

Figure 2.12 (a) Binding energies of HO* and O* versus the new bulk descriptor $E_{2p} - 0.4\ E_{t2g}$, where E_{2p} and E_{t2g} are the O 2p band energy level and t_{2g} minority spin band center relative to E_F, respectively, from the 2 × 2 × 2 cubic supercell calculations. (b) The AEM overpotentials

of *A*C, *A*F, *A*FC, and *A*CF (*A* = Sr, $La_{0.5}Sr_{0.5}$, and La) plotted against the descriptor ($E_{2p} - 0.4\ E_{t2g}$). Lines in (a) and (b) are added for guidance. Copyright © 2022 American Chemical Society.

Figure 2.13 In $La_xSr_{1-x}Co_yFe_{1-y}O_3$ (x=0.0, 0.5, 1.0, y=0.0, 0.5), the OER overpotential is plotted by binding energy difference between O* and HO* ($\Delta\mathbf{E_O} - \Delta\mathbf{E_{OH}}$). The OER overpotential is based on AEM 4 step reaction (Section 1.2.3). Copyright © 2022 American Chemical Society.

Figure 2.14 Gibbs free energy of HOO* plotted against the Gibbs free energy of HO* calculated for $La_xSr_{1-x}Co_yFe_{1-y}O_3$ (x, y = 0.0, 0.25, 0.5, 0.75, or 1.0) (a) without explicit solvent condition and (b) with explicit solvent. The solid lines indicate the lines fitting by (a) $\Delta G_{OOH} = 0.82\Delta G_{OH} + 3.397$ and (b) $\Delta G_{OOH} = 0.79\Delta G_{OH} + 3.173$. To differentiate the OER reaction path favored for each material, the AEM and LOM types are denoted by filled and open circles, respectively. Copyright © 2022 American Chemical Society.

Figure 2.15 (a) Overpotential contour map based on the scaling relation ($\Delta G_{OOH} = 0.79\Delta G_{OH} + 3.173$). The gray filled circles and line correspond to $La_xSr_{1-x}FeO_3$ calculated for x = 0.0, 0.5, or 1.0 and the guidance to eye, respectively. Similarly, the black open circles and line denote the case for $La_xSr_{1-x}Co_{0.5}Fe_{0.5}O_3$. The former and latter are denoted as *A*F and *A*CF, respectively, with the left- and right-end corresponding to Sr and La, respectively, for the *A*-site. The pink star indicates the most optimal point with an overpotential of 0.21 V. The black dashed line represents the $\Delta G_O = 3.0$ eV corresponding to the boundary of the two regions favoring AEM (lower-right) and LOM (upperleft). (b) Overpotential contour map based on the scaling relation as same with (a). The gray filled circle and line show the points of $La_xSr_{1-x}CoO_3$ (x=0.0, 0.5, 1.0) and its trend line. Fe-Co half mixed cases are represented as the black open circle and the trend of the *A*$Fe_{0.5}Co_{0.5}O_3$ is denoted by the black solid line as denoted by *A*C and *A*FC. Among the 6 points, LSFC (η_{LSFC} = 0.43 V) is closest to the optimal point (pink star, $\boldsymbol{\eta}$ = 0.21 V). Copyright © 2022 American Chemical Society.

Figure 2.16 Gibbs free energy difference (ΔG) as function of x and y in $La_xSr_{1-x}Co_yFe_{1-y}O_3$. Top boxes present the results for the Co active site, while the remaining bottom boxes present the results for the Fe active site. The highest ΔG is a PDS and the discrepancy between the highest free energy step and 1.23 V (gray dashed line) determines the theoretical overpotential. The lowest overpotential according to *A* variation is indicated by a gray double arrow in each *B* composition with its value. For all the plotted free energies, the water solvent is explicitly included. In each active site, the lowest overpotential is denoted by red rectangle. Copyright © 2022 American Chemical Society.

Figure 2.17 (a) Oxygen evolution reaction via the lattice-oxygen participation mechanism on the LSC surface. Red, pink, bright green, and dark green spheres represent oxygen, hydrogen, lanthanum, and strontium atoms, respectively. The top-left, bottom-left, bottom-right, and top-

right structures indicate OH*, (V_O+OO)*, (V_O+OH)*, and (H_O+OH)* adsorbed on the LSC (001) surface, respectively. Nature Communications, Copyright © 2021, Nam Khen Oh et al. (b) Gibbs free energy difference ($G_{V_{O+OO*}} - G_{OH}$) as function of suggested new descriptor (E_{2p} – 0.4 E_{dxy}). The Gibbs free energy difference is mainly related to potential determining step (PDS) of the lattice oxygen participated mechanism (LOM). Black solid line indicates potential of 1.23 V which could be the reference for optimal LOM materials in order to satisfy the Sabatier principle. Copyright © 2022 American Chemical Society.

Figure 2.18 Calculated binding energies of O* as a function of (a) O p-band center and (b) new descriptor E_{2p} - 0.4 E_{dxy}. The binding energy for AFeO$_3$/ACoO$_3$ and ACo$_y$Fe$_{1-y}$O$_3$ (A=La$_x$Sr$_{1-x}$; x, y = 0.0, 0.5, 1.0) are shown in open circles and triangles, respectively. The color of open circles and triangles indicates the species of active metal site (red = Fe, blue = Co). The additional calculated binding energies of O* for $LaCrO_3$ (pink star), $LaMnO_3$ (purple star), $LaNiO_3$ (gray star), $LaCuO_3$ (brown star) and $LaNi_{0.5}Fe_{0.5}O_3$ (gray and red open star) are shown together. In LaBO$_3$ (B = Cr, Mn, Fe, Co, Ni, and Cu), surface B-atom d_{xy} down spin orbital projected DOS for (c) clean surface and (d) O*. As O intermediate is adsorbed, d_{xy} down orbital starts to be filled in Mn and completely filled in Ni. However, in Cr, d_{xy} down orbital is not filled in both the clean surface and O*. Conversely, in Cu, even from the clean surface, d_{xy} orbital is fully filled. This means that the Cr and Cu OER intermediate binding strengths are independent of d_{xy}. This is the reason why $LaCrO_3$ and $LaCuO_3$ cannot be described by our new descriptor.

Figure 2.19 Based on our calculation results, the AEM and LOM boundary line according to *A*-/*B*-mixing is presented. The upper left green area composition is expected to follow LOM and the lower right purple area is expected to follow AEM. The dashed line in each area represents the line where optimal overpotential could appear. The *A*-mixing can correspond to the effect of hole (or electron) doping through the hetero stack, where the amount of non-local or free carriers determines the doping concentration. Whereas, the *B*-mixing can explain the local effect of oxygen vacancy as it affects the amount of local 3d electrons. The AEM optimal line is estimated from Figure 2.12b and the LOM optimal line is deducted by the Figure 2.17b results. (Reference information, [5], [43], [44])

Figure 3.1 (a) Raman spectra after experiment without water vapor that were measured at the open metal surface (upper spectrum) and at the diamond surface after removal of the Ni film (lower spectrum). (b) Schematic of the Ni−diamond system; the green arrows show the diffusion direction of the C atoms. (c) SEM image of the graphite film formed on the open Ni surface. (d) Raman spectra obtained after the experiment with water vapor present in the quartz chamber, which were measured at the open metal surface (upper spectrum) and at the diamond surface after the removal of the Ni_xO_y/Ni film (lower spectrum). (e) Schematic of C diffusion through a Ni film and oxidation of C atoms at the open Ni surface. (f) SEM image of the nickel (oxide) surface. Copyright © 2022, American Chemical Society.

Figure 3.2 (a, b) Arrhenius plots of the dissolution rates of single-crystal diamonds with (100) surfaces coated with a (a) 500 nm-thick Ni film and (b) 500 nm-thick Co film, at different water bubbler temperatures. (c, d) Arrhenius plots of the dissolution rates of single-crystal diamond with (110) surfaces coated with a (c) 500 nm-thick Ni film and (d) 500 nm-thick Co film, at different water bubbler temperatures. (e) Real-time residual gas analyzer (RGA) analysis of water vapor－Ni－diamond reaction products. (f) Schematic of diamond dissolution with water vapor present: the surface reaction [regime I when this is rate-limiting, step (iii)] and the metal diamond interface where diamond dissolves into the metal through breaking of C－C bonds at the M－D interface [regime II when this is rate-limiting, step (i)]. Step (ii) represents diffusion of C atoms through the Ni film-this is never rate-limiting for our study. Copyright © 2022, American Chemical Society.

Figure 3.3 (a,b) Potential energy curves calculated for (a) H_2O molecule reacting with Ni(100) (green) or Co(100) (blue) and (b) for C－C bond breaking at the Ni(100)/D(100) (green) or Co(100)/D(100) (blue) interfaces. The corresponding atomic structures of the initial, intermediate, and final configurations are shown as insets. (c,d) Potential energy curves calculated for a C atom diffusing from (c) Ni(100)/D(100) interface (green) through the octahedral site (O*) or (d) Co(110)/D(110) interface (blue) through the tetrahedral site (T*). The corresponding atomic structures of the initial, intermediate, and final configurations are shown as insets. Copyright © 2022, American Chemical Society.

Figure 3.4 (left) Potential energy curves for an H_2O molecule reacting with the Ni(100) or Co(100) surfaces; (right) atomic structures of the initial physisorbed molecule (x= 0.0), the transition state (x= 0.4) and other intermediate configurations. Copyright © 2022, American Chemical Society.

Figure 3.5 Potential energy curve for the surface reaction on Ni(100). **(a)** Potential energy curve for C atom migration from an octahedral (O*) site at the subsurface to an O* site at the surface, as shown in the inserted schematic image, which shows the reaction process from x= 0.0 to 1.0 (1). The O atom migrates from the original O* site to the O* site that the C atom had occupied yielding formation of -Ni-C-O (2), followed by release of one CO into the atmosphere (3). **(b)** Potential energy curve for C atom migration from an O* site at the subsurface to an O* site at the surface, as shown in the inserted schematic diagram, which shows the reaction process from x= 0.0 to 1.0 (1). The O atom migrates from the original O* site to an O* site that the C atom had occupied forming -Ni-C-O (2), followed by release of one CO into the atmosphere (3). Note that there are two possible paths for the migration of the

O atom at the metal surface because there are two inequivalent half-octahedral sites that the C atom occupied relative to the position of the O atom at the surface. We calculated the two paths and provide the potential energy curve for both. The energy barriers at each step for these two paths are lower than the energy barrier of the surface reaction between a Ni atom and a H_2O molecule. Copyright © 2022, American Chemical Society.

Figure 3.6 Potential energy curve for the surface reaction on Co(100). Potential energy curve for one C atom migration from an octahedral site (O*) at the subsurface to an O* site at the surface, as shown in the inserted schematic, which shows the reaction process from x= 0.0 to 1.0 (1). The oxygen atom migrates from the original O* site to the O* site that the C atom had occupied and forms the -Co-C-O state (2), and the -Co-C-O state decomposes and releases a CO(g) molecule into the atmosphere (3). The path calculated is the same as that calculated in **Figure 3.5a**, which has a lower energy barrier in steps (1) and (2) compared with the energy barrier for steps (1) and (2) in **Figure 3.5b**. The energy barriers at each step for this path are lower than the energy barrier of the surface reaction between a Co atom and a H_2O molecule. Copyright © 2022, American Chemical Society.

Figure 3.7 (left) Potential energy curves for a H_2O molecule reacting with the Ni(110) or Co(110) surface; (right) atomic structures of the initial physisorbed (x= 0.0) state, the transition state (x= 0.4) and other intermediate configurations. Copyright © 2022, American Chemical Society.

Figure 3.8 Potential energy curve for the surface reaction on (a) Ni(110) and (b) Co(110). One C atom jumps from an octahedral (O*) site at the subsurface to a tetrahedral (T*) site, then to the surface, as shown in the inserted schematic; from x= 0.0 to 1.0 (1), the O atom migrates from the original O* site to the T* site that the C atom occupied and forms -M-C-O (2), and the -M-C-O then releases a CO molecule into the atmosphere (3). Thus: From x= 0.0 to 1.0 the indicated C atom moves to the surface, from x= 1.0 to 2.0 a surface O atom and that same surface C atom migrate and react, and from x= 2.0 to 3.0 CO desorbs. The appearance of a C atom on the M(110) surface thus occurs in two steps, as shown in the inserted schematic: from x= 0.0 to 0.5, a C atom in the sublayer moves to a T* site just below the open surface, and from x= 0.5 to 1.0, this C atom moves from the T* site to the open surface. For Ni(110), this diffusion from subsurface to the surface has the highest energy barrier (161 kJ/mol) when the C atom migrates to the open surface. For Co(110) the highest energy barrier (165 kJ/mol) is for the C atom passing through the T* site. Copyright © 2022, American Chemical Society.

Figure 3.9 (left) Potential energy curves for C atom diffusion at the Ni(110)/D(110) (green curve) and Co(110)/D(110) (blue curve) interfaces through the (a) *tetrahedral* and (b) *octahedral* interfacial sites; (right) atomic structures of the initial (x= 0.0), intermediate (x= 0.2, 0.4, 0.6, and 0.8), and final (x= 1.0) configurations. Copyright © 2022 American Chemical Society.

Figure 3.10 Potential energy curves of carbon diffusion barriers in fcc-Ni and fcc-Co. The C atom diffuses from an octahedral site to a tetrahedral site, then back to the octahedral site (O* → T* → O*). We show the C atom diffusion energy barrier from the O* site to T* site only, due to symmetry. Copyright © 2022 American Chemical Society.

Figure 3.11 (left) Potential energy curves for C atom diffusion at the Ni(100)/D(100) (green curve) and Co(100)/D(100) (blue curve) interfaces; (right) atomic structures of the initial (x= 0.0), intermediate, and final (x= 1.0) configurations. Copyright © 2022 American Chemical Society.

Figure 3.12 (a) Schematic comparison of interface dissolution and bulk FCC metal carbon diffusion. Due to the higher activation barrier of bulk diffusion, backward reaction may occur in this scheme. (b) Actual calculated activation barrier (T = 1386 K) of the process which is described in (a). Red circle indicates the surface Ni atom that move onto the carbon vacancy site in diamond. The first bulk carbon diffusion shows very low activation barrier (15.4 kJ/mol) compared to the reverse reaction barrier of interface carbon dissolution.

Figure 3.13 The location of transferred Ni at (left) the bird-eye view, and (right) bottom-up direction view.

List of Tables

Table 2.1 The solvation free energy among the SC, SF, LC and LF. In our results, we applied the solvation energy of $La_xSr_{1-x}BO_3$ as function of x which is denoted in eq (2.5). (Unit: eV) Copyright © 2022 American Chemical Society.

Table 2.2 Intermediate binding energy table. For convenience, like $La_{0.25}Sr_{0.75}Co_{0.75}Fe_{0.25}O_3$, 1:3 ratio mixing of A-/B-site is expressed as L1S3C3F1 and the last abbreviation indicates the active B-site metal. (Unit: eV) Copyright © 2022 American Chemical Society.

Table 2.3 Gibbs free energy table with explicit solvent. The abbreviation capital alphabet represents L = La, S = Sr, C = Co, F = Fe. For convenience, like $La_{0.25}Sr_{0.75}Co_{0.75}Fe_{0.25}O_3$, 1:3 ratio mixing of *A*-/*B*-site is expressed as L1S3C3F1 and the last abbreviation indicates the active *B*-site metal. (Unit: eV) Copyright © 2022 American Chemical Society.

Table 3.1 The detailed parameters of the simulation model. Copyright © 2022, American Chemical Society.

Table 3.2 $\Delta H^{\ddagger}$ and Prefactor *A* Values, from a Study of the Dissolution of D(100) and D(110) Coated with a 500 nm-Thick Ni or Co Film. Copyright © 2022, American Chemical Society.

Table 3.3 Energy Barrier Values (kJ/mol) Describing the Formation of −Ni−C−O or −Co−C−O States on Ni/Co(100) and Ni/Co(110) Surfaces and the Decomposition to Release CO into the Gas Phase. Copyright © 2022, American Chemical Society.

I. Introduction

1.1 General Information

Since the industrial use of catalysts in the production of sulfuric acid by John Roebuck in 1746, catalysts are used in many industries by lowering the potential energy barrier of difficult or necessary reactions and by increasing the yield of products. Catalysts are used for biofuel[1], hydrocarbon reforming[2], water splitting[3], nitrogen oxide and fine dust removal, material synthesis, etc., and their usage is increasing. In order to find and utilize new catalysts, it is necessary to know how the catalyst forms and breaks bonds with chemicals and what physical properties are important to be controlled.

1.1.1 Water Splitting for Hydrogen Production

Recently, theoretical research is being actively conducted in the catalyst chemistry used in eco-friendly energy production and synthesis of new materials. With the increasing demand for sustainable energy, human beings put forward higher requirements for the preparation of clean energy. For an alternative to fossil fuels, hydrogen production is in the limelight. As shown in Figure 1.1, since 2000 hydrogen-related publications have grown very rapidly.[4] Most of them were studies on materials (deep blue) or systems (orange) that store hydrogen itself, but since 2010, research on power-to-gas (gray) has increased a lot. Research on hydrogen is receiving great attention as a means to effectively store electricity, and the most interesting research keyword for hydrogen powered systems was efficiency (Figure 1.2).

Electrocatalytic water splitting has become a promising way to solve the energy crisis because of the characteristics of high efficiency and cleanliness. The catalyst of oxygen evolution reaction (OER), an important part of electrocatalytic water splitting, plays a critical role in water splitting to increase reaction kinetics, efficiency, and reaction selectivity. Due to its importance, the development of OER electrocatalysts is required.

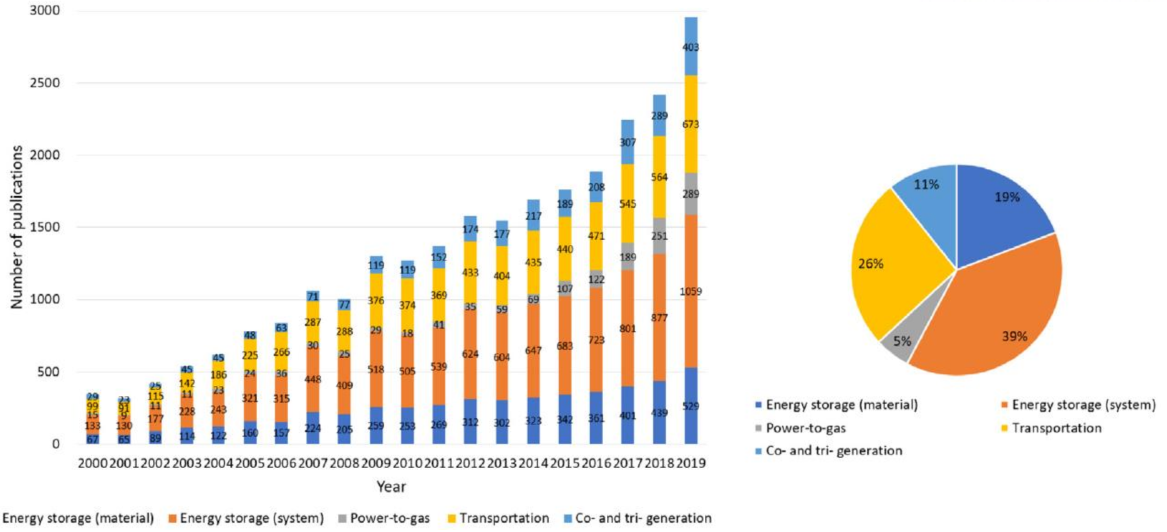

Figure 1.1 Yearly evolution and percentage distribution of publications from 2000 to date containing terms ‘‘hydrogen’’ AND ‘‘storage’’ AND ‘‘material’’, ‘‘hydrogen’’ AND ‘‘energy storage system’’ NOT ‘‘tank’’, ‘‘hydrogen’’ AND ‘‘power-to-gas’’, ‘‘hydrogen’’ AND ‘‘transportation’’, ‘‘hydrogen’’ AND (‘‘co-generation’’ OR ‘‘tri-generation’’). The search was made on the 2th June 2020.Copyright © 2021 M. Yue et al. Published by Elsevier Ltd.[4]

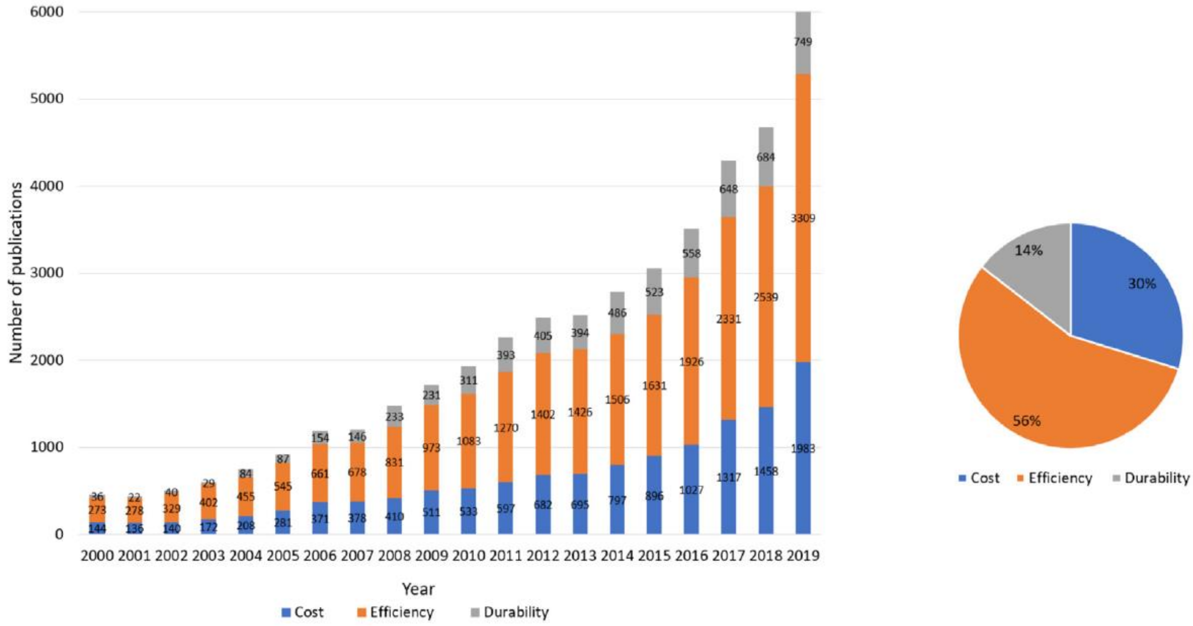

Figure 1.2 Yearly evolution and percentage distribution of publications from 2000 to date containing terms ‘‘hydrogen’’ AND (‘‘cost’’ OR ‘‘economy’’), ‘‘hydrogen’’ AND ‘‘efficiency’’, ‘‘hydrogen’’ AND (‘‘durability’’ OR ‘‘lifetime’’ OR ‘‘degradation’’). The search was made on the 2th June 2020. Copyright © 2021 M. Yue et al. Published by Elsevier Ltd.[4]

1.1.2 Carbon Control for Material Synthesis

Catalysts are important in the synthesis of carbon materials. An advantage of carbon materials is that they can be configured in a variety of ways from simple graphite sp^2 structure to complex bio-organic molecules. In addition, there are various allotropes made only of carbon, such as diamond, graphite, lonsdaleite, Buckminsterfullerene, C_{540}, C_{70}, amorphous carbon, and carbon nanotube. Aside from the possibilities of various carbon materials, it is very difficult to synthesize and control the structure of a desired material. It has been carried out through theoretical and experimental research for the synthesis of practical materials. For instance, the mechanism of forming the carbon nanotubes (CNTs) has been revealed, recently.[5] Through the density functional theory (DFT) simulations, L. P. Ding et al. found that the CNT-catalyst interface has an important role in CNT growth (Figure 1.3). Several experimental and theoretical collaborations have revealed the fabrication of graphene flakes[6] or graphene nanowall[7] on the metal surface edge. For the development of new carbon materials, understanding the mechanism of bond breaking and formation through metal catalysis becomes important.

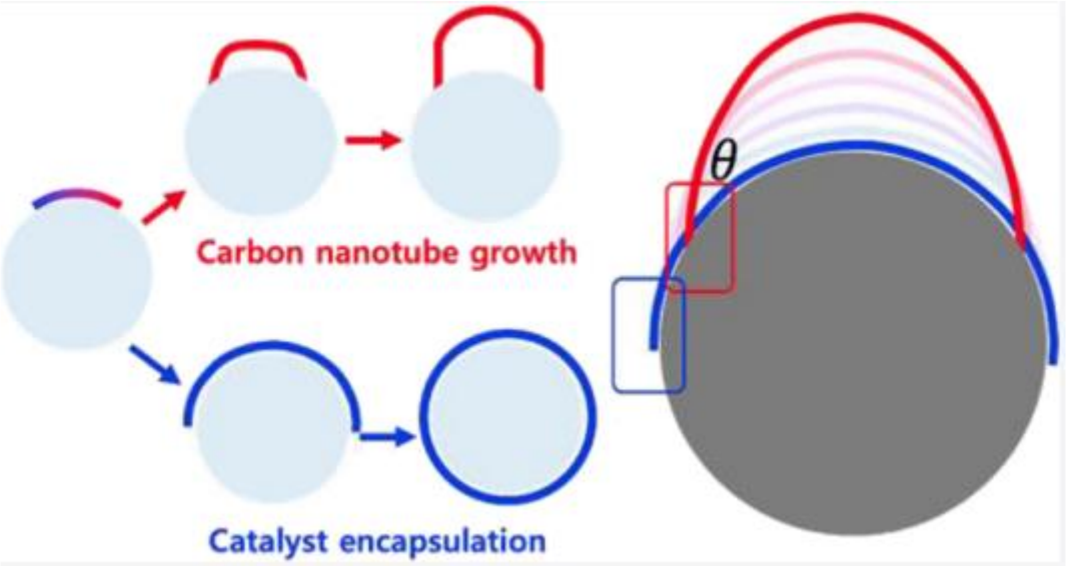

Figure 1.3 L. P. Ding et al. reveal the fundamental aspect of the CNT-catalyst interface, viz., that the interfacial energy of the CNT–catalyst edge is contact angle-dependent. This angle dependence can give a rationale why the CNTs grow.[5] Copyright © 2022 American Chemical Society.

1.2 DFT simulations for OER Electrocatalysts

To develop a high-performance electrocatalyst, we can increase the intrinsic activity of the catalyst or increase the number of active sites. The density functional theory (DFT) simulation can give a rationale of the intrinsic activity of catalyst by showing the adsorption energies and activation energies of the reactions.[8,9] As suggested by Nørskov, the theoretical activity of electrocatalyst can be obtained from Gibbs free energy of the reaction intermediates.[10]

1.2.1 Computational Standard Hydrogen Electrode

The computational standard hydrogen electrode (CHE) suggested by Nørskov et al.[10] is extensively used to calculate theoretical electrochemical potentials based on the DFT. According to CHE method, the hydrogen electrode is assumed to be in equilibrium, i.e. the solvated protons and electrons are in equilibrium with the hydrogen in the gas phase:

$$H^+(aq) + e^- \rightleftarrows \frac{1}{2}H_2(g) \qquad (1.1)$$

$$\mu_{H^+} + \mu_{e^-} = 1/2\mu_{H_2(g)} \qquad (1.2)$$

The chemical potential of proton, electron and hydrogen as follows:

$$\mu_{H^+} = \mu_{H^+}^0 + k_B T \ln a_{H^+} \qquad (1.3)$$

$$\mu_{e^-} = \mu_{e^-}^0 - eU \qquad (1.4)$$

$$\mu_{H_2(g)} = \mu_{H_2(g)}^0 + k_B T \ln p_{H_2} \qquad (1.5)$$

where a_{H^+} represents the activity of the protons, eU represents the shift in electron energy when a bias is applied and p_{H_2} is the partial pressure of hydrogen. $\mu_{H^+}^0$, $\mu_{e^-}^0$, $\mu_{H_2(g)}^0$ represent the chemical potential of protons, electrons and hydrogen at standard conditions (p_{H_2} = 1 bar, a_{H^+} = 1, T = 298.15 K). Therefore, the relation can be written as:

$$\mu_{H^+}^0 + \mu_{e^-}^0 = \frac{1}{2}\mu_{H_2(g)}^0 \qquad (1.6)$$

Then, we can calculate $\mu_{H_2(g)}^0$ as the Gibbs free energies of hydrogen gas:

$$G_{H_2} = E_{H_2}^{DFT} + ZPE - TS \qquad (1.7)$$

where the ZPE and S indicate zero-point energy and calculated entropy of the hydrogen.

1.2.2 Electrochemical Half-Reaction of Water Splitting, OER

Based on the CHE method, the theoretical reaction barrier of electrochemical reactions can be calculated, which is called as overpotential. In water splitting, there are two half-reactions. One is the hydrogen evolution reaction (HER) and the other one is the oxygen evolution reaction (OER) which generates hydrogen molecule and oxygen molecule, respectively. From an electrochemical point of view, the standard reduction potential for water splitting is 1.23 V, but in reality a higher voltage is required for the electrochemical reaction and the additional voltage is called as overpotential. As described in Figure 1.4, each half-reaction has its overpotential and the total overpotential of water splitting is given by:

$$\eta_{water-splitting} = \eta_{HER} + \eta_{OER} \qquad (1.8)$$

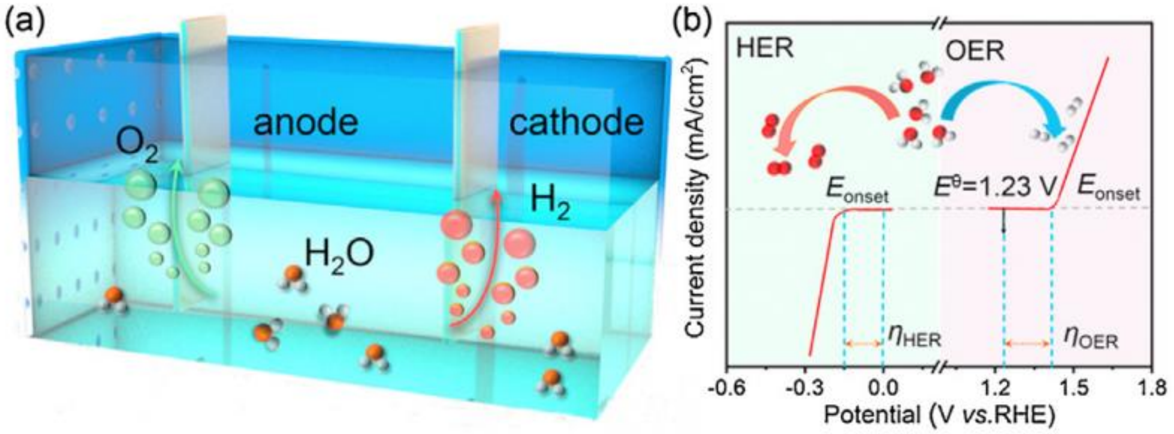
(a)
anode
cathode
O_2
H_2
H_2O
(b)
HER
OER
E_{onset}
E^{θ}=1.23 V
E_{onset}
η_{HER}
η_{OER}
Current density (mA/cm^2)
-0.6
-0.3
0.0
1.2
1.5
1.8
Potential (V vs.RHE)

Figure 1.4 (a) Hydrogen evolution reaction (HER) and oxygen evolution reaction (OER) of electrocatalytic water splitting and (b) Schematic representation of HER and OER overpotentials.[11] Copyright © 2021 Published by Elsevier B.V.

Appropriate electrochemical catalysts are required to minimize the overpotential. However, the overpotential mainly increases due to the sluggish OER that accompanies the multi-step reaction (see Section 1.2.3). Therefore, a good OER electrocatalyst to be applied to the anode is necessary.

1.2.3 OER Electrolysis on Perovskite Oxide

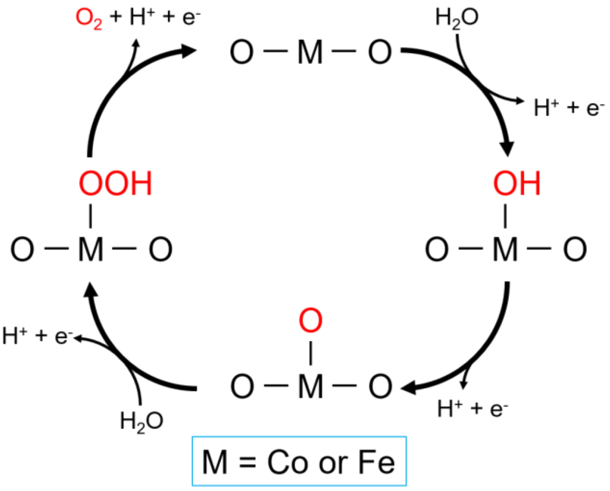

Figure 1.5 Conceptual illustration of concerted four step adsorbate evolution reaction (AEM) mechanism.

As introduced by I. C. Man et al.,[12] the oxygen evolution reaction follows the four concerted reaction path on the electrocatalyst surface as followed:

$$* + H_2O \rightleftarrows * OH + H^+ + e^- \qquad (1.9)$$

$$* OH \rightleftarrows * O + H^+ + e^- \qquad (1.10)$$

$$* O + H_2O \rightleftarrows * OOH + H^+ + e^- \qquad (1.11)$$

$$* OOH \rightleftarrows * + O_2(g) + H^+ + e^- \qquad (1.12)$$

The four step reaction is called the adsorbate evolution reaction (AEM) and mainly occurs on the surface of a metal oxide catalyst (Figure 1.5). AEM is often seen on ABO_3 perovskite oxide surface. Using CHE, which we discussed in Section 1.2.1, we can calculate the Gibbs free energy of each step of the OER of the perovskite surface. Starting with eq (1.2), we postulate the OER at standard conditions (U = 0V, pH = 0, p = 1 bar, T = 298.15K) and chemical potential of hydrogen molecule and water molecule are approximately equal to DFT total energies where ZPE indicates zero-point energy of denoted molecules.

$$\mu_{H_2(g)} = E_{DFT}^{H_2(g)} + ZPE_{H_2(g)} - TS_{H_2(g)}^0 \quad (6)$$

$$\mu_{H_2O(g)} = E_{DFT}^{H_2O(g)} + ZPE_{H_2O(g)} - TS_{H_2O(g)}^0 \quad (7)$$

Thereby the free energies of (1), (2), (3), and (4) are given by followed paragraph:

$$\Delta G_1 = G_{*OH} + \mu_{H^+} + \mu_{e^-} - G_* - \mu_{H_2O} \quad (8)$$

$$G_{*OH} = E_{DFT}^{*OH} + ZPE_{*OH} - TS_{*OH}^0 \quad (9)$$

$$G_* = E_{DFT}^* \quad (10)$$

From equation (5), (6), (7), (9), and (10), ΔG_1 is given by:

$\Delta G_1 = E_{DFT}^{*OH} + \frac{1}{2}E_{DFT}^{H_2(g)} - E_{DFT}^{*} - E_{DFT}^{H_2O(g)} + \Delta ZPE - T\Delta S^0$ (11)

As similar way, other reactions are:

$\Delta G_2 = G_{*O} + \mu_{H^+} + \mu_{e^-} - G_{*OH}$ (12)

$\Delta G_2 = E_{DFT}^{*O} + \frac{1}{2}E_{DFT}^{H_2(g)} - E_{DFT}^{*OH} + \Delta ZPE - T\Delta S^0$ (13)

$\Delta G_3 = G_{*OOH} + \mu_{H^+} + \mu_{e^-} - G_{*O} - \mu_{H_2O}$ (14)

$\Delta G_3 = E_{DFT}^{*OOH} + \frac{1}{2}E_{DFT}^{H_2(g)} - E_{DFT}^{*O} - E_{DFT}^{H_2O(g)} + \Delta ZPE - T\Delta S^0$ (15)

$\Delta G_4 = G_{*} + G_{O_2(g)} + \mu_{H^+} + \mu_{e^-} - G_{*OOH}$ (16)

$\Delta G_4 = E_{DFT}^{*} - E_{DFT}^{*OOH} + 2E_{DFT}^{H_2O(g)} - \frac{1}{2}E_{DFT}^{H_2(g)} + 4.92 + \Delta ZPE - T\Delta S^0$ (17)

DFT intermediate binding energies are given by:

$\Delta E_{OH} = E_{DFT}^{*OH} - E_{DFT}^{*} + \frac{1}{2}E_{DFT}^{H_2(g)} - E_{DFT}^{H_2O(g)}$ (18)

$\Delta E_{O} = E_{DFT}^{*O} - E_{DFT}^{*} + E_{DFT}^{H_2(g)} - E_{DFT}^{H_2O(g)}$ (19)

$\Delta E_{OOH} = E_{DFT}^{*OOH} - E_{DFT}^{*} + \frac{3}{2}E_{DFT}^{H_2(g)} - 2E_{DFT}^{H_2O(g)}$ (20)

However, another mechanism has also been suggested for *AB*O_3 perovskite.[13] When the oxygen in the lattice of *AB*O_3 is unstable, the lattice oxygen on the surface also participates in the OER reaction as described in Figure 1.6 and the mechanism is called the lattice oxygen mechanism (LOM). It can be assumed that the stability of surface lattice oxygen determines the mechanism, and when designing an OER catalyst, it is necessary to quickly determine which mechanism to follow. The Gibbs free energy in each state can be obtained from LOM as well as from AEM.

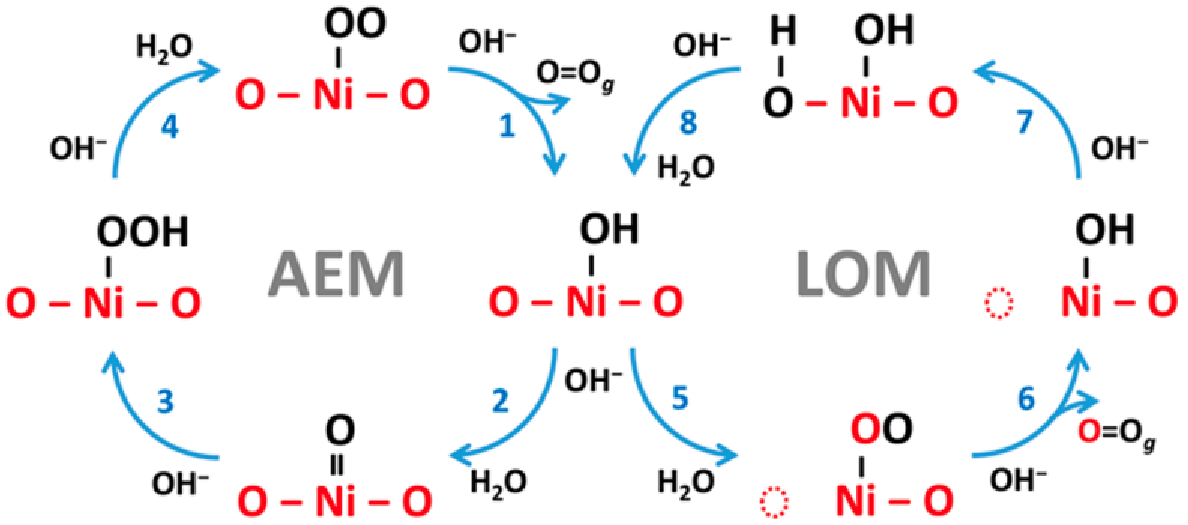

Figure 1.6 In Ni-based perovskite, schematic illustration of the competition between the Adsorbate Evolution Mechanism (AEM) and Lattice-Oxygen Participation Mechanism (LOM).[14] Copyright © 2018 American Chemical Society.

1.3 Carbon Control via Metal Surface

Various attempts have been made to control through the metal surface for the synthesis of carbon materials.[5,6,7] Nowadays, understanding the interaction between metal surfaces and carbon through theoretical research is a very important task.

1.3.1 Carbon Diffusion

An example of the simplest computational approach is the study of the kinetics of carbon diffusion in bulk metal such as Ni, Fe[15-18] and grain boundary.[19] The carbon diffusion activation barrier shown by DFT simulations in FCC bulk metals appeared when the carbon moved from octahedral site (Figure 1.7a) to tetrahedral site (Figure 1.7b). Carbon diffusion through metal can be another graphene synthesis method without exfoliation technique, where amorphous carbon diffuses inside the 3d transition metal to form multilayer graphene on the opposite side which is called layer-exchange growth of multilayer graphene (Figure 1.8).[20] There is a possibility that it can be used for synthesis technique via carbon diffusion in 3d transition metals.

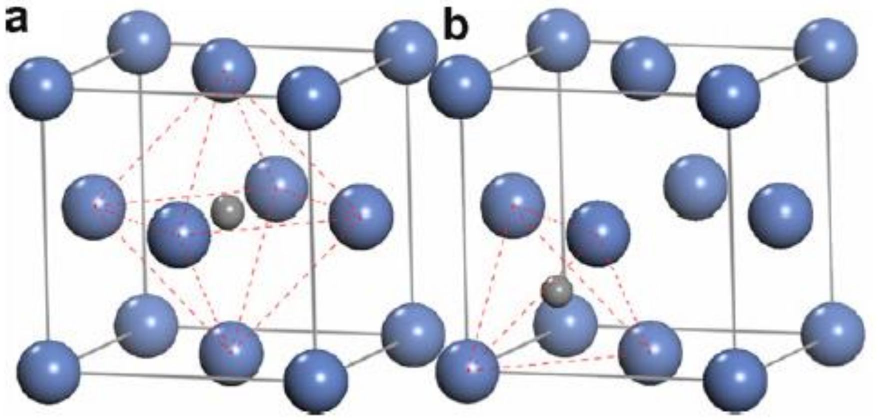

Figure 1.7 Illustration of C dissolution at the interstitial (a) O-site and (b) T-site in bulk Ni. Large balls denote Ni atoms and small balls denote C atoms.[15] Copyright © 2006 Elsevier Ltd.

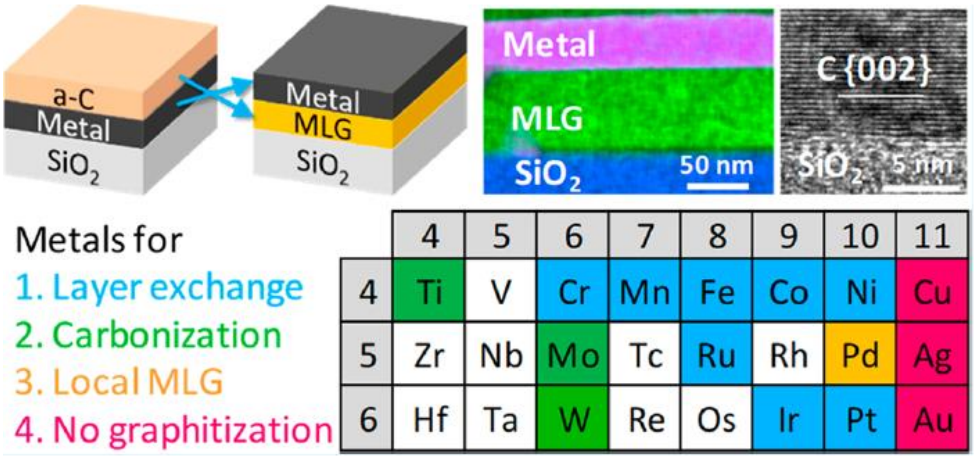
a-C
Metal
SiO2
Metal
MLG
SiO2
Metal
MLG
SiO2
50 nm
C {002}
SiO2
5 nm
Metals for
1. Layer exchange
2. Carbonization
3. Local MLG
4. No graphitization
4 5 6 7 8 9 10 11
4 Ti V Cr Mn Fe Co Ni Cu
5 Zr Nb Mo Tc Ru Rh Pd Ag
6 Hf Ta W Re Os Ir Pt Au

Figure 1.8 Some 3d transition metals can induce layer exchange to turn amorphous carbon into graphene.[20] Copyright © 2018 American Chemical Society.

1.3.2 Growth of Carbon

A carbon material synthesis method via carbon growth with metal surface as a starting site has been studied as discussed in Section 1.1.2. Carbon materials are made by initiating and growing on the terrace or step edge of the metal surface. Recently, the cause of CNTs growth has been discovered[5], and silmilarly, we revealed the reason why the formation of graphene nanowalls(Figure 1.9, 1.10) occur along the Cu(111) edge directions.[7] Being able to initiate carbon growth along the metal edge direction can suggest a new direction for material synthesis.

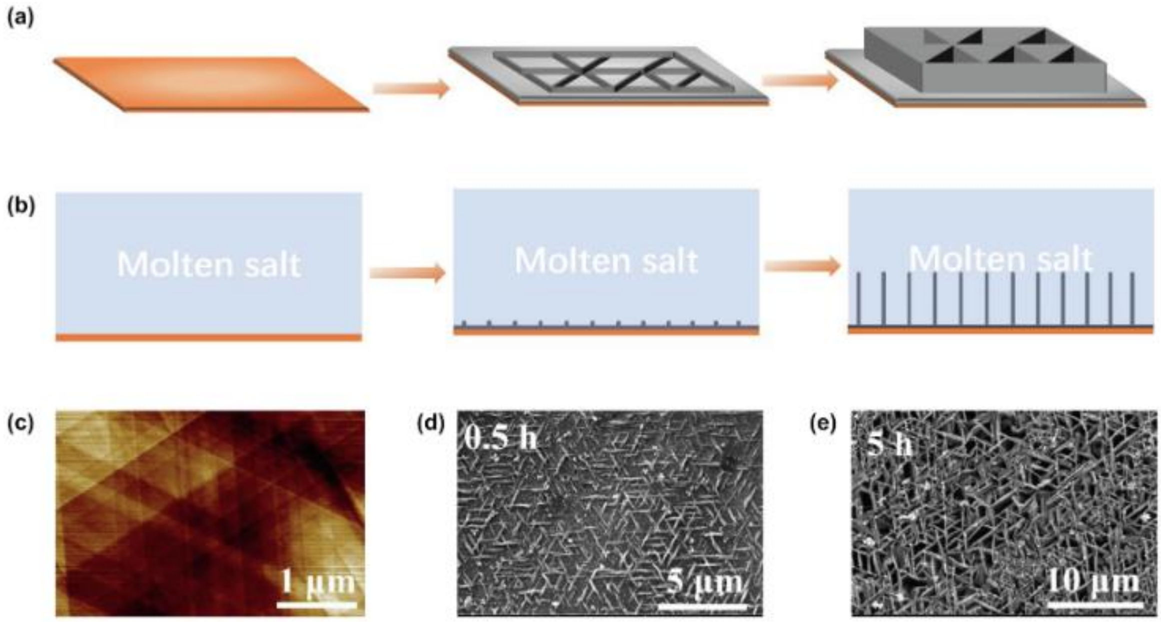

Figure 1.9 (a,b) Schematic representations of growth of CNWs. (c) AFM image of bare Cu (111) surface. (d, e) SEM images of CNWs deposited at -1.25 V for (d) 0.5 h and (e) 5h.[7] Copyright © 2022 Elsevier Ltd.

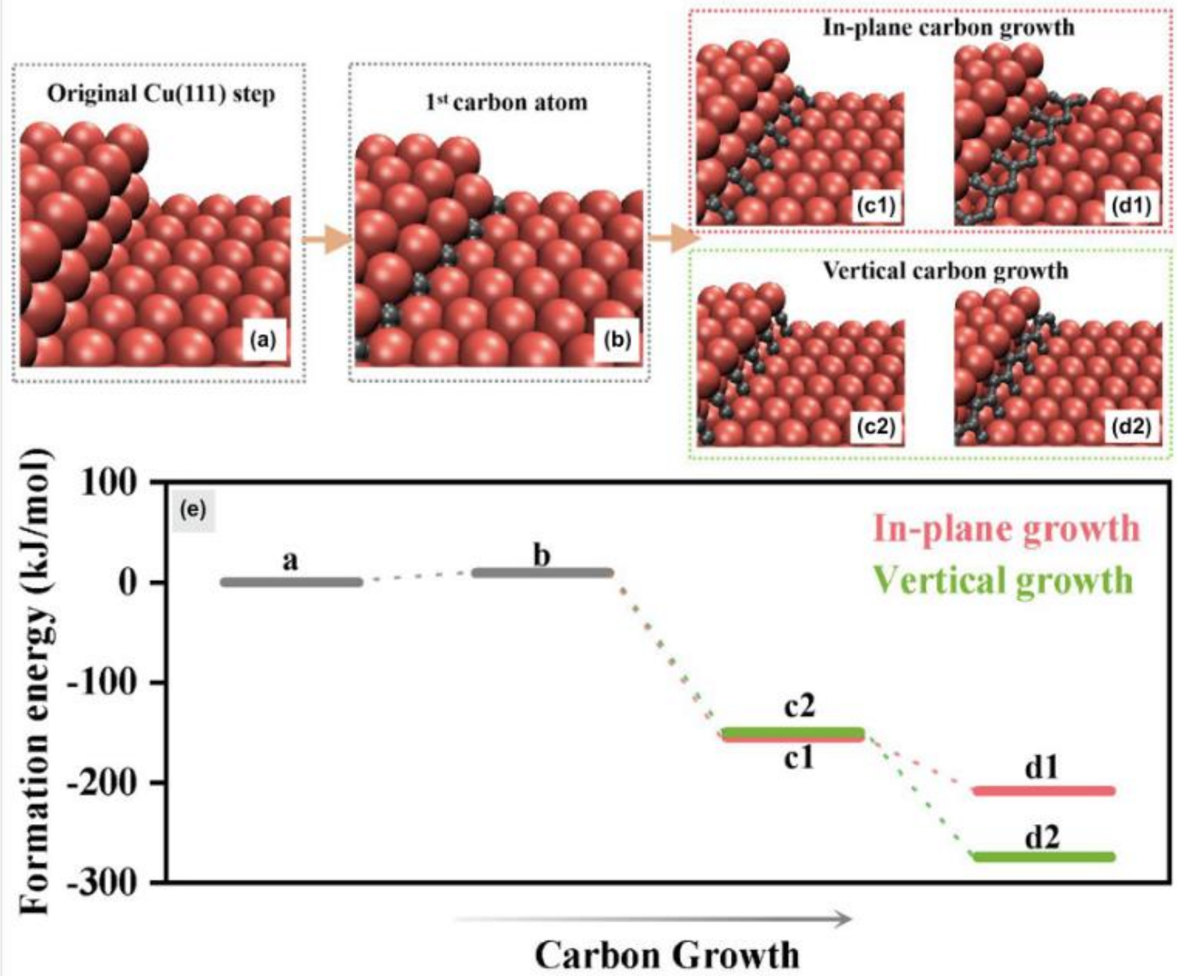

Figure 1.10 (a) The optimized structure of the Cu(111) with a two-atom step running along the <110> slip direction; (b) The optimized structure of the first carbon atom adsorbed at an edge of the step and the lower terrace; The optimized structures following (c1 and d1) in-plane carbon growth or (c2 and d2) vertical carbon growth; (e) Calculated formation energy per carbon atom according to equations (1) and (2). (Each step shown corresponds to these structures: a, b, c1, d1, c2, d2).[7] Copyright © 2022 Elsevier Ltd.

1.4 Outline of Dissertation

In this dissertation, the reason why metal oxides or surfaces of metals used as catalysts form bonds and induce chemical deformation is explored through computational research.

In Chapter 2, through DFT calculations, we reveal the physical origins that determine the catalystic activity in the $La_xSr_{1-x}Co_yFe_{1-y}O_3$ (LSCF) double perovskite oxide (*AA*’*BB*’O_6) structure used as an OER electrocatalyst, and suggest a way to design a highly efficient catalyst based on theoretical analysis. Furthermore, by closely analyzing the mixing effect of *A*-site and *B*-site, we propose a new descriptor that expresses the electrocatalyst activity well and present the possibility of material design that goes beyond Fe-Co mixing.

In chapter 3, the mechanism of carbon dissolution and diffusion at the junction of diamond and metal was revealed, and the thermodynamically expressed enthalpy was identified through computational research. In addition, the surface exchange mechanism by which the surface carbon of diamond can dissolve into the FCC Ni and Co surface was revealed.

1.5 References

(1) Mortensen, P. M.; Grunwaldt, J. D.; Jensenm P. A.; Knudsen, K. G.; Jensen, A. D. A review of catalytic upgrading of bio-oil to engine fuels. *Applied Catalysis A: General* **2011**, 407, 1–19.

(2) Cortright, R. D.; Davda, R. R.; Dumesic, J. A. Hydrogen from catalytic reforming of biomass-derived hydrocarbons in liquid water. *Nature*, **2002**, 418, 964–967.

(3) McCrory, C. C. L.; Jung, S.; Peters, J. C.; Jaramillo, T. F. Benchmarking Heterogeneous Electrocatalysts for the Oxygen Evolution Reaction *J. Am. Chem. Soc*. **2013**, 135, 45, 16977–16987.

(4) Yue, M.; Lambert, H.; Pahon, E.; Roche, R.; Jemei, S.; Hissel, D. Hydrogen energy systems: A critical review of technologies, applications, trends and challenges, *Renewable and Sustainable Energy Reviews*, **2021**,146, 111180.

(5) Ding, L. P.; McLean, B.; Xu, Z.; Kong, X.; Hedman, D.; Qiu, L.; Page, A. J.; Ding, F. Why Carbon Nanotubes Grow. *J. Am. Chem. Soc*. **2022**, 144, 5606−5613.

(6) Yuan, Q.; Yakobson, B. I.; Ding, F. Edge-Catalyst Wetting and Orientation Control of Graphene Growth by Chemical Vapor Deposition Growth. *J. Phys. Chem. Lett*. **2014**, 5, 3093−3099.

(7) Wang, M.; Kim, Y.; Zhang, L.; Seong, W. K.; Kim, M.; Chatterjee, S.; Wang, M.; Li, Y.; Bakharev, P. V.; Lee, G. S.; Lee, S. H.; Ruoff, R. S. Controllable electrodeposition of ordered carbon nanowalls on Cu(111) substrates. *Materials Today* **2022**, 57, 75-83.

(8) Hammer, B.; Nørskov, J. K. Theoretical surface science and catalysis – Calculations and concepts, *Advances in Catalysis*, **2000**, 45, 71-129.

(9) Bligaard, T.; Nørskov, J. K. Heterogeneous Catalysis. *Chemical Bonding at Surfaces and Interfaces*; Nilsson, A.; Pettersson, L. G. M.; Nørskov, J. K., Eds.; Elsevier: Amsterdam, 2008; p 255-321.

(10) Nørskov, J. K.; Rossmeisl, J.; Logadottir, A.; Lindqvist, L.; Kitchin, J. R.; Bligaard, T.; Jónsson, H. Origin of the Overpotential for Oxygen Reduction at a Fuel-Cell Cathode. *J. Phys. Chem. B* **2004**, 108, 46, 17886–17892.

(11) Li, X. P.; Huang, C.; Han, W. K.; Ouyang, T.; Liu, Z. Q. Transition metal-based electrocatalysts for overall water splitting. *Chinese Chemical Letters*, **2021**, 32, 2597–2616.

(12) Man, I. C.; Su, H. Y.; Calle-Vallejo, F.; Hansen, H. A.; Martínez, J. I.; Inoglu, N. G.; Kitchin, J.; Jaramillo, T. F.; Nørskov, J. K.; Rossmeisl, J. Universality in Oxygen Evolution Electrocatalysis on Oxide Surfaces. *ChemCatChem* **2011**, *3* (7), 1159–1165.

(13) Grimaud, A.; Diaz-Morales, O.; Han, B.; Hong, W. T.; Lee, Y. L.; Giordano, L.; Stoerzinger, K. A.; Koper, M. T. M.; Shao-Horn, Y. Activating Lattice Oxygen Redox Reactions in Metal Oxides to Catalyse Oxygen Evolution. *Nat. Chem.* **2017**, *9* (5), 457–465.

(14) Yoo, J. S.; Rong, X.; Liu, Y.; Kolpak, A. M. Role of Lattice Oxygen Participation in Understanding Trends in the Oxygen Evolution Reaction on Perovskites. *ACS Catal*. **2018**, 8, 5, 4628–4636.

(15) Zhu, Y.; Dai, Y.; Chen, D.; Yuan, W. First-principles study of carbon diffusion in bulk nickel during the growth of fishbone-type carbon nanofibers, *Carbon*, **2007**, 45, 1, 21-27.

(16) Jiang, D. E.; Carter, E. A. Carbon dissolution and diffusion in ferrite and austenite from first principles. *Phys. Rev. B* **2003**, 67, 214103.

(17) Massaro, T. A.; Petersen, E. E. Bulk Diffusion of Carbon-14 through Polycrystalline Nickel Foil between 350 and 700°C. *Journal of Applied Physics* **1971**, 42, 5534.

(18) Wiltner, A.; Linsmeier, Ch.; Jacob, T. Carbon reaction and diffusion on Ni(111), Ni(100), and Fe(110): Kinetic parameters from x-ray photoelectron spectroscopy and density functional theory analysis. *THE JOURNAL OF CHEMICAL PHYSICS* **2008**, 129, 084704.

(19) Siegel, D. J.; Hamilton, J.C. Computational study of carbon segregation and diffusion within a nickel grain boundary. *Acta Materialia* **2005**, 53, 87–96.

(20) Nakajima, Y.; Murata, H.; Saitoh, N.; Yoshizawa, N.; Suemasu, T.; Toko, K. Metal Catalysts for Layer-Exchange Growth of Multilayer Graphene. *ACS Appl. Mater. Interfaces* **2018**, 10, 41664−41669.

II. Theoretical Investigation for Rational Design of the Perovskite Oxide OER Elecatalysts

This chapter includes the materials of:

Unveiling surface electronic descriptor for Fe-Co mixing enhanced stability and efficiency of perovskite oxygen evolution electrocatalysts.

Yongchul Kim, Miran Ha, Anand Rohit, Mohammad Zafari, Jeong Min Baik, Hyesung Park, Geunsik Lee*, Submitted.

2.1 Introduction

In order to produce hydrogen without emitting greenhouse gases, electrochemical splitting of water is a desirable way for sustainable energy storage. However, it is required improving in efficiency and stability of eletrocatalysts composed of earth abundant elements for large-scale hydrogen production. The state-of-the-art electrocatalysts have been consisted of noble-metal, such as Pt, IrO_2, or RuO_2 for the hydrogen evolution reaction (HER), and oxygen evolution reaction (OER). Various studies have attempted to replace noble-metal-based catalysts. Among those electrocatalysts candidate, perovskite oxides (ABO_3) have attracted a lot of attention as it can be easily synthesized with various compositions and crystal structures[1-3], and has good OER performance. As OER electrocatalysts, $Ba_{0.5}Sr_{0.5}Co_{0.8}Fe_{0.2}O_{3-\delta}$ (BSCF) and $La_{0.6}Sr_{0.4}Co_{0.8}Fe_{0.2}O_{3-\delta}$ (LSCF) double perovskite oxides have attracted attention as they outperformed the OER activity of IrO_2[4,5]. In addition, Fe-doping in $La_xSr_{1-x}CoO_3$ (LSC) and $Ba_xSr_{1-x}CoO_3$ (BSC) improved the structural stability and electro-catalytic activity[6-8]. *A*-site mixing as well as *B*-site mixing causes various changes of perovskite oxide properties. For instance, by mixing Sr with $LaCoO_3$, the space group variation is observed from rhombohedral (R-3c) to cubic (Pm-3m)[9,10], spin state change can be accompanied[8,10-12], and the OER performance can be enhanced[9,11].

To make efficient and robust electrocatalyst, what influences the intrinsic catalytic activity and stability of perovskite oxides during electrolysis is need to be clearly understood. Attempts have been made to create descriptors that explain phenomena well through understanding of physical properties. There has been a pioneering report that the number of e_g electrons in the t_{2g}/e_g crystal field derived from the O_h symmetry of *B* metal has a correlation with the OER activity[1,2,13]. As the stability of lattice oxygen is considered to be related to OER performance, the O 2p center level has been proposed as a OER descriptor[11,14-16]. Also, the O 2p level implies the degree of hybridization between *B* atom 3d orbitals and lattice oxygen 2p orbitals which is related to OER intermediate species binding strength on the active site. There have also been attempts to theoretically describe OER performance through an approach to calculating Gibbs free energy[17] and crystal structural information[5,18]. However, there are problems with each descriptor, e_g electron number is difficult to obtain through DFT simulations[12,19], Gibbs free energy is difficult to study in experiments and operando environment, and crystal structure is also affected by various factors, so it has a disadvantage to use as a descriptor.

In this study, based on the surface electronic structure, a good descriptor was devised and the possibility of electrocatalyst rational design was tested.

2.2 Methods

2.2.1 Calculation Information

Density functional theory (DFT) calculations using the VASP package were performed with the RPBE exchange correlation[20,21]. The plane wave energy cutoff was 520 eV. Our structural models are based on the reported cubic perovskite crystals of $SrCoO_3$, $LaCoO_3$, $SrFeO_3$, and $LaFeO_3$ with experimental lattice constants of 3.8289, 3.8200, 3.8531, and 3.926 Å, respectively[22-25]. For mixed double perovskite, the cubic lattice is used with the supercell lattice constant determined based on the weighted average of each pure perovskite component. For instance, the lattice constant of $La_xSr_{1-x}BO_3$ with *A*-site mixing is given by $a_{\mathrm{La}BO3}x + a_{\mathrm{Sr}BO3}(1-x)$. Herein, $La_xSr_{1-x}Fe_yCo_{1-y}O_3$ with x = 0.0, 0.5, and 1.0 and y = 0.0 is denoted as SC, LSC, and LC, respectively, and y = 1.0 is denoted as SF, LSF, and LF, respectively. The model structure shown in Figure 2.1 corresponds to x = y = 0.5, i.e., LSFC or LSCF depending on the Co or Fe active site, respectively, which is indicated by the last abbreviation alphabet. For the spatial arrangement of the mixed *A*- or *B*-site atoms, the rock-salt type presented in Figure 2.1 is adopted as an example of a highly disordered structure associated with high-temperature synthesis condition.

The OER Gibbs energies are calculated based on the following concerted reactions under standard condition (U = 0 V, pH = 0, p = 1 bar, and T = 298.15 K)[17,26]:

$$* + \mathrm{H_2O} \rightleftarrows \mathrm{HO}* + \mathrm{H^+} + \mathrm{e^-} \quad (2.1)$$

$$\mathrm{HO}* \rightleftarrows \mathrm{O}* + \mathrm{H^+} + \mathrm{e^-} \quad (2.2)$$

$$\mathrm{O}* + \mathrm{H_2O} \rightleftarrows \mathrm{HOO}* + \mathrm{H^+} + \mathrm{e^-} \quad (2.3)$$

The DFT binding energies of the three intermediates (HO, O, and HOO) are calculated using the symmetric slab model (Figure 2.1) with a sufficient vacuum size (>15 Å). With the 2 × 2 lateral supercell size, we verified that the adsorption energies change by less than 0.01 eV when the slab thickness is increased by more than three periodic units, as shown in Figure 2.1. Additionally, the ferromagnetic alignment of the spins is initially assumed for all cases. Although the presence of different magnetic ground states has not been studied, the change of the Gibbs energy difference will be sufficiently small. For structural optimization, only the upper two atomic layers of the slab are relaxed with the force criteria of 0.01 eV/A. The k-mesh is 2 × 2 × 1 for the geometric optimization and 12 × 12 × 1 for the density of states. The theoretical free energies and overpotentials are calculated by applying the computational standard hydrogen electrode model[17,26], and their definitions and details are discussed in Section 1.2. As is well-known, the LOM advantageously detours the reaction path to avoid the HOO* intermediate stage, overcoming the scaling-relations-induced limitations[17]. Although LOM is highly advantageous, due to the participation of lattice oxygen, it suffers from surface amorphization, leading to the partial deactivation of the electrocatalyst[4,11,16,27]. Therefore, it is worthwhile to search based on AEM to obtain a robust electrocatalyst. In this study, we focus AEM since AEM exhibits simplicity and high structural stability during electrolysis. Focusing on the AEM could be meaningful, because according to the report of Kim et al., catalysts that are known to follow LOM follow AEM (pH independence) near neutral pH (~7)[28].

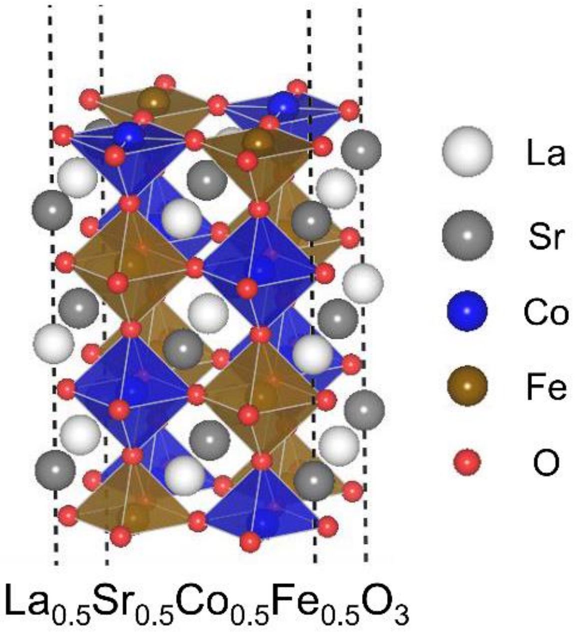

Figure 2.1 Rock-salt ordered slab model of $La_{0.5}Sr_{0.5}Co_{0.5}Fe_{0.5}O_3$. *A*- and *B*-site are described as highly isotropic chemical environment. Copyright © 2022 American Chemical Society.

2.2.2 Explicit Solvent and Minima Hopping Methods

Various studies have referred that the solvation effect plays an important role in the OER intermediate species stability[29-36]. Although implicit solvation calculations have the obvious advantage of low computational cost, they are not accurate enough as local effects are neglected, such as hydrogen bonding between water molecules and OER intermediates[29]. To depict the accurate solvent effect, a suitable explicit solvent model is required. We performed a global minimization process called minima hopping[37] through the Atomic Simulation Environment (ASE)[38] commencing from the initial ice-like most stable water layer to determine the water placement (Figure 2.2)[30]. Among the various ABO_3 compositions, we tested the explicit solvent effect on $SrCoO_3$, $SrFeO_3$, $LaFeO_3$, and $LaCoO_3$. The solvent effect had a difference energy of 0.1 eV according to A mixing in the HOO* intermediate and was almost independent of the *B* metal species. In $La_xSr_{1-x}BO_3$, the solvation energy was reflected as $x * \Delta G^{\text{solv}}_{\text{La}BO3} + (1-x) * \Delta G^{\text{solv}}_{\text{Sr}BO3}$ according to the *A* ratio. Since the solvent effect was mainly reflected by the hydrogen bonding to the intermediates, the binding strength was not notably affected by the *AB*O_3 surface composition. Based on the surface composition insensitivity of solvation energy, the average solvation energies of the HO*, O*, and HOO* intermediates were −0.394, +0.008, and −0.643 eV for SrBO3 and −0.401, +0.009, and −0.544 for LaBO3, respectively (Table 2.1). In order to describe a realistic water environment, I utilized explicit water model. To get the explicit solvent initial positions, structure optimization by minima hopping[37] was done, and the most stable structure in each OER intermediate was taken as the initial position. After we get the initial solvent position, additional optimization was taken into account to calculate solvation free energy:

$$\Delta G^{\text{solv}} = E_{DFT}^{\text{opt}} - E_{DFT}^{\text{solvent}} - E_{DFT}^{\text{slab}} \qquad (2.4)$$

The solvation free energy is represented in Table 2.1. To deal with a mixed perovskite oxide ($La_xSr_{1-x}BO_3$), we considered solvation energy as followed equation:

$$\Delta G^{\text{solv}} = x \cdot \frac{\left(\Delta G_{\text{LaCoO3}}^{\text{solv}} + \Delta G_{\text{LaFeO3}}^{\text{solv}}\right)}{2} + (1-x) \cdot \frac{\left(\Delta G_{\text{SrCoO3}}^{\text{solv}} + \Delta G_{\text{SrFeO3}}^{\text{solv}}\right)}{2} \qquad (2.5)$$

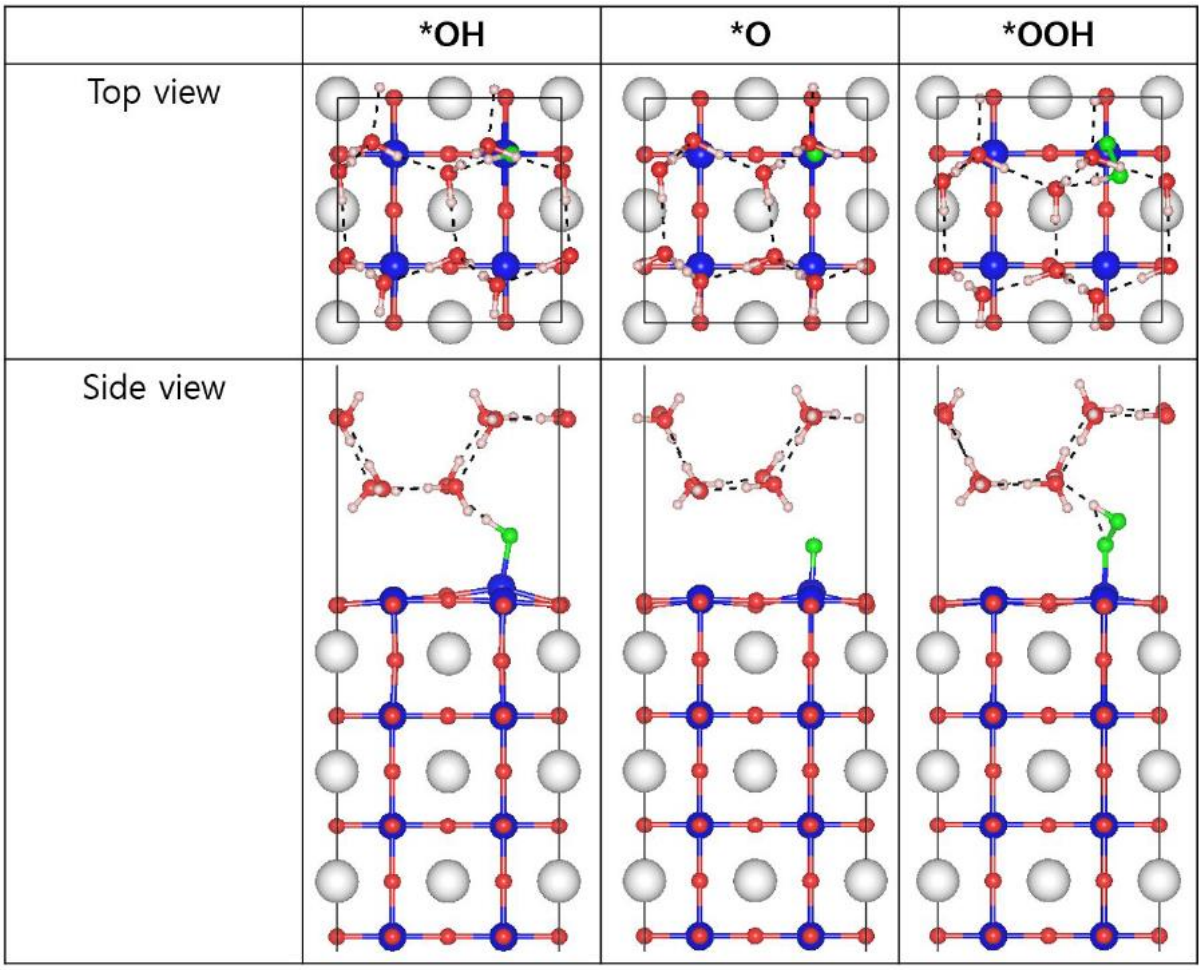

Figure 2.2 Optimized $LaCoO_3$ structure with the explicit solvent. The explicit water molecule initial positions were given by atomic simulation environment (ASE) package global optimization. *OH and *OOH intermediate form hydrogen bond with water molecule. The different colors indicate each atom (La = white, Co = blue, O = red, intermediate O = green, H = pink). Copyright © 2022 American Chemical Society.

Table 2.1 The solvation free energy among the SC, SF, LC and LF. In our results, we applied the solvation energy of $La_xSr_{1-x}BO_3$ as function of x which is denoted in eq (2.5). (Unit: eV) Copyright © 2022 American Chemical Society.

	ΔG^{*OH}_{solv}	ΔG^{*O}_{solv}	ΔG^{*OOH}_{solv}
$SrCoO_3$	-0.3912	0.0327	-0.6783
$SrFeO_3$	-0.3972	-0.0167	-0.6070
$LaCoO_3$	-0.3883	0.0098	-0.5419
$LaFeO_3$	-0.4138	0.0115	-0.5454

2.3 Results and Discussion

2.3.1 OER Mechanism and Intermediates Binding Strength

Based on the AEM described schematic in Figure 1.?, the binding energies of OER intermediate were investigated. In reports, the binding energy of OER intermediate species (E_b) are described well with O p-band center relative to the Fermi level (E_{2p})[7,14,15]. As shown in Figure 2.3, the bulk oxygen p-band center showed good correlation with OER current density, *O binding energy, ORR surface exchange coefficient and XES p-band center[15]. In addition, R. Jacob reported that the PBE functional predicts the oxygen p-band center best than other functional[15]. Following the literature, it is worthy that calculate the OER intermediate binding energies as a function of oxygen p-band center. I simulated the double perovskite $La_xSr_{1-x}Co_yFe_{1-y}O_3$ (LSCF) system to test the correlation.

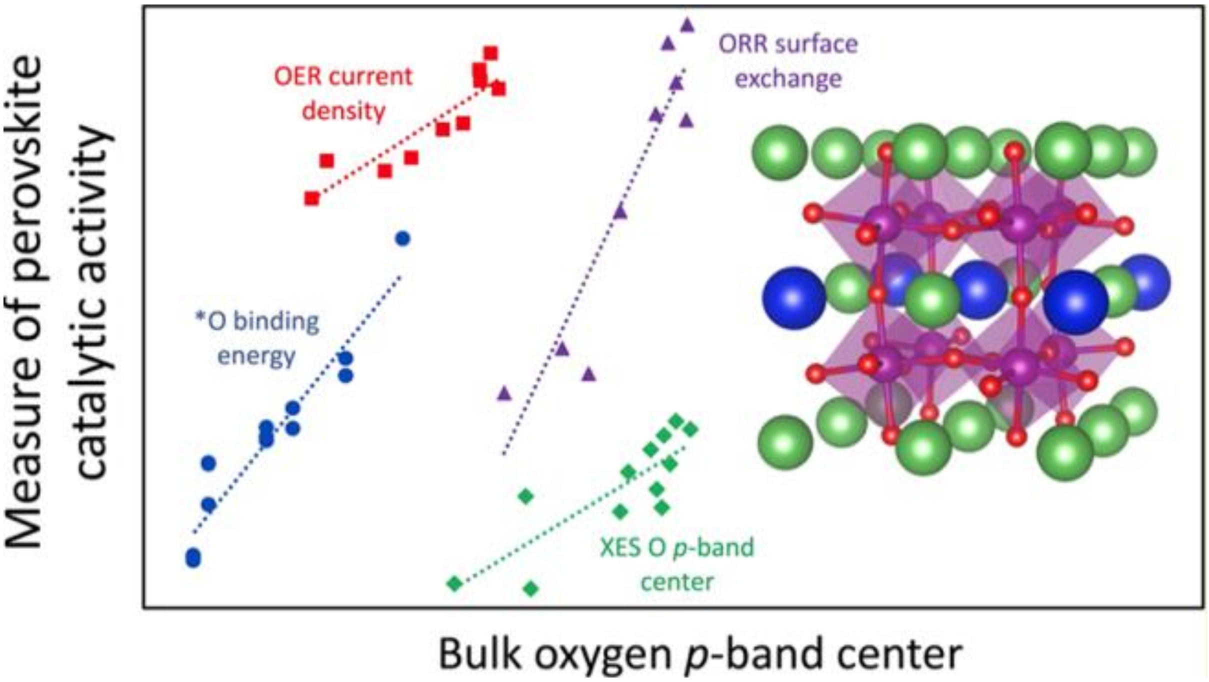

Figure 2.3 According to the R. Jacob. report, catalytic activity of perovskite correlates with bulk oxygen p-band center. Reprinted from ref. 15. Copyright © 2019, American Chemical Society.

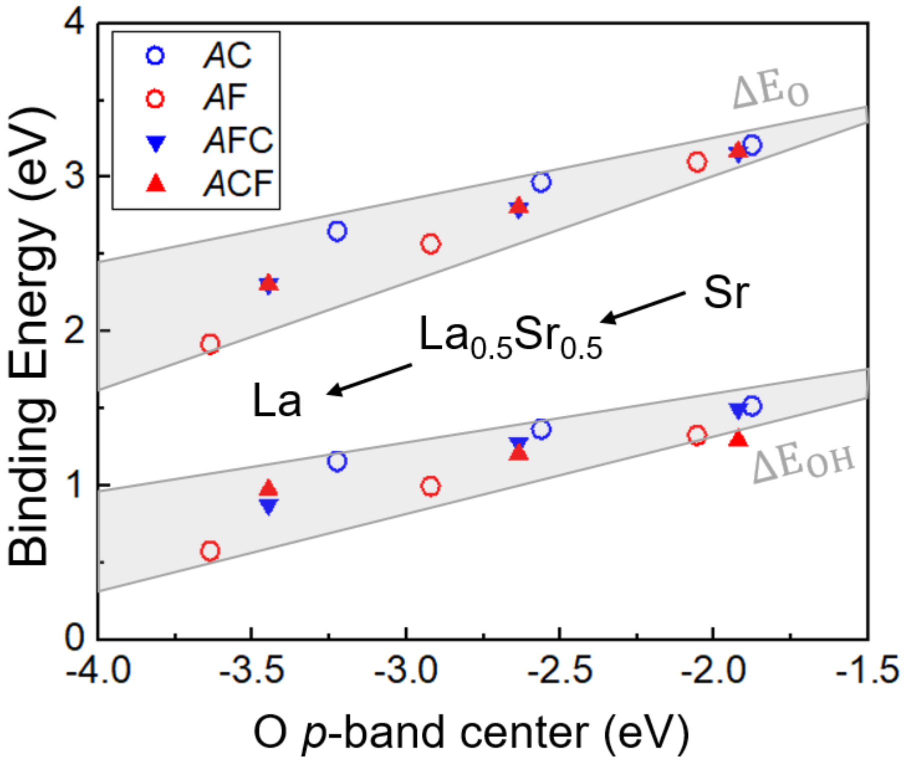

Figure 2.4 Calculated binding energies of HO* (ΔE_{OH}) and O* (ΔE_{O}) on the (001) surface as a function of O p-band center for $La_xSr_{1-x}Co_yFe_{1-y}O_3$ with x, y = 0.0, 0.5, or 1.0. The color of the symbols indicates the species of the active metal site (red = Fe and blue = Co). The binding energies of AFeO$_3$ (*AF*) and ACoO$_3$ (*AC*) are represented with open circles, where the mixed case (y = 0.5) are denoted by upward- and downward-facing triangles. Both of notation *ACF* and *AFC* represent $ACo_{0.5}Fe_{0.5}O_3$ composition, the last abbreviation alphabet (C or F) indicates the active *B*-site element. Copyright © 2022 American Chemical Society.

Figure 2.4 shows the calculated binding energies as a function of E_{2p} for the nine compounds of ABO_3, where *A* and *B* denote La_xSr_{1-x} and Co_yFe_{1-y}, respectively, with x or y = 0.0, 0.5, and 1.0. For a given y value, the E_{2p} value decreases with increasing x value or La doping, e.g., SF to LF or SC to LC. This is mainly because additional electrons introduced by La doping are almost free and fill more empty states; thus, the oxygen states shift downward in the energy relative to the Fermi level. The positive correlation between E_b and E_{2p} shows that the binding of the intermediate species becomes accordingly stronger. In contrast, the increase of y for a given x value causes the increase of the E_{2p} value, e.g., LF to LC, although Co has one more d electron than Fe. The main reason is ascribed to the higher electron withdrawing capability of Co compared to Fe with respect to O, in accordance with the ligand hole behavior reported for $SrCoO_3$[39-41]. The additional electron of Co plays a minor role in increasing the Fermi level due to the localized character of d electrons. Consequently, the intermediate species binding becomes less stable with Co doping. Figure 2.4 shows that the reported 2p band center descriptor (E_{2p}) cannot well describe the complete behavior of the intermediate species binding energies. Under the same amount of downshift in E_{2p} by La or electron doping, *A*FeO$_3$ exhibits larger binding energy stabilization than *A*CoO$_3$, as indicated by the gray zone in the figure. The reason for the larger binding energy variation for Fe is attributed to the extra d electron of Co. In order to explain this different variation, surface electronic structure was investigated in followed section. The whole intermediate species (HO*, O*, and HOO*) binding energies are summarized in Table 2.2 include other composition (x or y = 0.25, or 0.75).

Table 2.2 Intermediate binding energy table. For convenience, like $La_{0.25}Sr_{0.75}Co_{0.75}Fe_{0.25}O_3$, 1:3 ratio mixing of A-/B-site is expressed as L1S3C3F1 and the last abbreviation indicates the active B-site metal. (Unit: eV) Copyright © 2022 American Chemical Society.

		ΔE_{OH}	ΔE_{O}	ΔE_{OOH}
1	SC	1.516	3.211	4.544
2	SF1C3	1.521	3.110	4.577
3	SFC	1.496	3.162	4.492
4	SF3C1	1.441	3.043	4.471
5	SF	1.331	3.097	4.617
6	SC1F3	1.284	2.997	4.508
7	SCF	1.305	3.169	4.622
8	SC3F1	1.208	3.154	4.564
9	L1S3C	1.483	3.121	4.518
10	L1S3F1C3	1.350	2.979	4.462
11	L1S3FC	1.326	2.950	4.407
12	L1S3F3C1	1.353	2.906	4.390
13	L1S3F	1.148	2.734	4.384
14	L1S3C1F3	1.209	2.842	4.435
15	L1S3CF	1.172	2.945	4.411
16	L1S3C3F1	1.146	2.960	4.371
17	LSC	1.373	2.970	4.433
18	LSF1C3	1.298	2.880	4.338
19	LSFC	1.278	2.796	4.321
20	LSF3C1	1.172	2.699	4.228
21	LSF	0.996	2.571	4.245
22	LSC1F3	1.191	2.703	4.458
23	LSCF	1.209	2.809	4.434
24	LSC3F1	1.162	2.845	4.387
25	L3S1C	1.287	2.858	4.333
26	L3S1F1C3	1.238	2.749	4.314
27	L3S1FC	1.125	2.596	4.235
28	L3S1F3C1	0.902	2.344	4.108
29	L3S1F	0.799	2.283	4.045
30	L3S1C1F3	0.909	2.417	4.181
31	L3S1CF	1.130	2.599	4.408
32	L3S1C3F1	1.155	2.687	4.429
33	LC	1.158	2.651	4.282
34	LF1C3	1.079	2.546	4.136
35	LFC	0.881	2.310	3.949
36	LF3C1	0.787	2.150	3.877
37	LF	0.585	1.922	3.893
38	LC1F3	0.701	2.130	4.048
39	LCF	0.981	2.310	4.244
40	LC3F1	1.070	2.472	4.355

2.3.2 Correlation of Surface Electronic Structure and Surface Stability

To figure out the detailed electronic structure of the active *B* metal site for La*B*O_3, projected density of states (PDOS) before and after O adsorption was analyzed. In Figure 2.5, for clarity, only the minority spin $d_{yz/xz}$ or d_{xy} are plotted, because they mainly contribute to the states near the Fermi level. For clean La*B*O_3, indicated by the dashed curves in Figure 2.5, more $d_{yz/xz}$ states are occupied for Co than Fe. With an O atom adsorbed (O*), the $d_{yz/xz}$ PDOS, indicated by the blue filled curves, exhibits a clear splitting into bonding and antibonding states due to the π interaction with O* $p_{x/y}$, where the Fermi level is close to the bottom of the π^* band for $LaCoO_3$ and is close to the top of the π band for $LaFeO_3$. Thus, the effective π bond order between *B* and adsorbate O is almost equal for *B* = Co and Fe in La*B*O_3, with essentially the same number of minority spin $d_{xz/yz}$ electrons involved in the π bond. Furthermore, the d_{xy} PDOS for O*, the red filled curves in Figure 2.5, does not exhibit an energy gap opening like $d_{yz/xz}$ with O adsorption. Instead, it remains almost intact like for the clean case, mainly because of the significantly stronger π interaction of the metal d_{xy} with surface O $p_{x/y}$ than that with O*. The associated states mainly appear inside the gap region between π and π^* bands formed by metal $d_{yz/xz}$ and O* $p_{x/y}$, whose metallic behavior facilitates electron gaining or losing. Moreover, the additional $d_{yz/xz}$ electron of $LaCoO_3$ relative to $LaFeO_3$ transfers to the metallic d_{xy} states rather than filling energetically unfavorable π^* states of $d_{yz/xz}$, which is why the Fermi level of $LaCoO_3$ is higher close to the π^* band bottom. Note that the bonding type character of metal d_{xy} with surface O $p_{x/y}$ almost diminishes and changes to antibonding type at an energy level close to the top of $d_{yz/xz}$ π band (Figure 2.6). Hence, to properly describe the binding energies, the probable electron transfer behavior from $d_{yz/xz}$ to d_{xy} of the active metal site need to be considered.

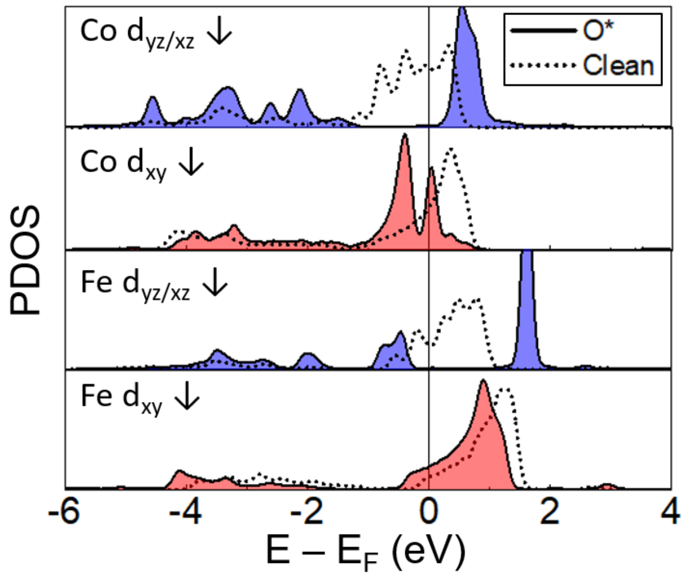

Figure 2.5 The PDOS of the minority spin d_{yz} and d_{xy} orbitals of the active metal site for La*B*O_3 before (Clean) and after adsorption of O (O*), which are represented by the dashed and solid lines, respectively. Copyright © 2022 American Chemical Society.

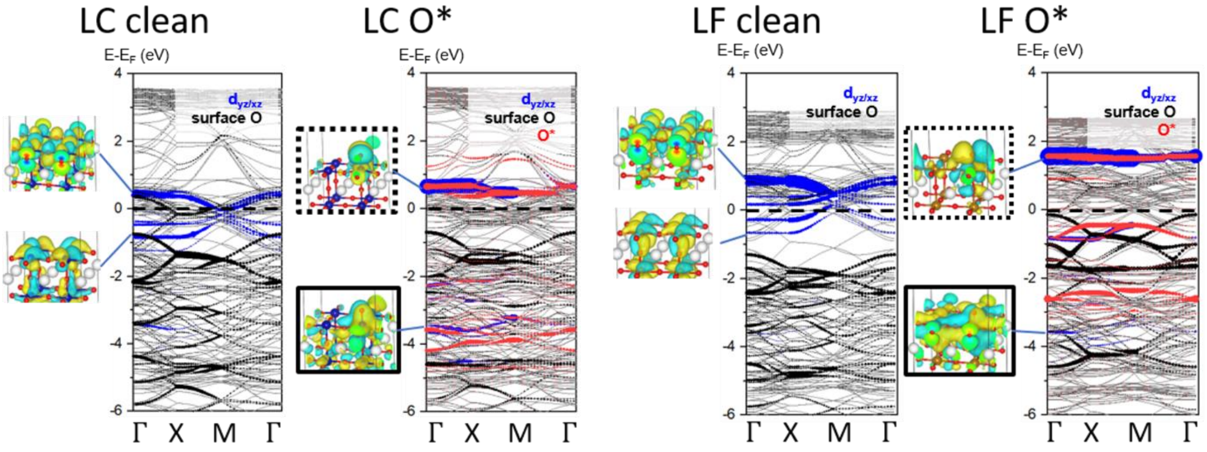

Figure 2.6 The $d_{yz/xz}$ minority spin projected band of $LaCoO_3$ and $LaFeO_3$ for clean surface and O*. In order to show some band characters, the wavefunctions of several representative bands related to d_{yz} at the Γ point are also shown in left of each band. The abbreviation capital alphabet represents L = La, C = Co, F = Fe, respectively. The band of the entire slab is shown in gray, active site $d_{yz/xz}$ and the surface oxygen band are shown in blue and black, respectively. After O was adsorbed to the surface, the band of intermediate O was shown in red. The wavefunction of each band shows that $d_{yz/xz}$ mainly forms a surface state before intermediate adsorption and mainly forms π bond with O after the adsorption. In O*, $d_{yz/xz}$ formed wavefunctions that mainly overlaps with O intermediate states, and it can be seen that it makes π-, π^*-bond. Bonding wavefunction is indicated by a solid box, and antibonding is indicated by a dashed box. Copyright © 2022 American Chemical Society.

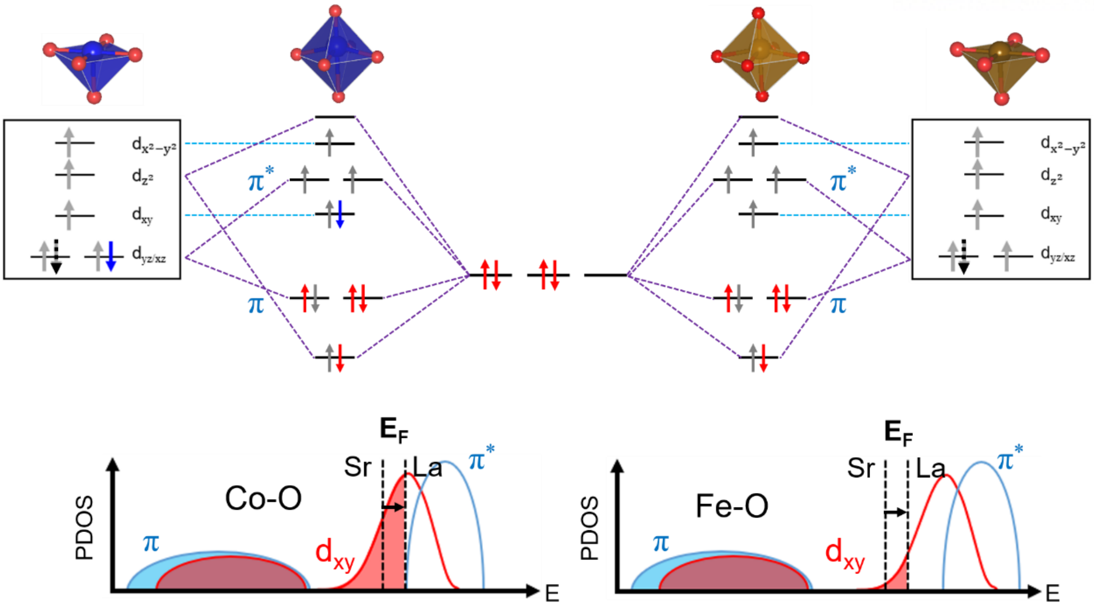

Figure 2.7 (Top) Orbital configurations of *A*CoO_3 and *A*FeO_3 for clean and O*. Before O intermediate adsorbed, the clean surface has C_{4v} symmetry. The blue arrow indicates the additional electron in Co active site compared with Fe active site. The gray arrows represent the other electron from *B* metal and red arrows indicate the electrons from intermediate O. The black dashed arrow shows the variation of electron number from Sr to La *A*-site substitution. (Bottom) The PDOSs after O adsorption are presented only for the minority spin $d_{yz/xz}$ (light blue sold line) or d_{xy} (red solid line) orbitals in π hybridization with $p_{x/y}$ of the adsorbate or surface-layer O, respectively, where the vertical dashed line denotes the Fermi level (E_F) shifting rightward upon changing Sr to La, with the occupied states denoted by filled color for La*B*O_3.

Figure 2.7 displays the schematic of the d orbital configuration of *A*FeO_3 and *A*CoO_3 in C_{4v} symmetry for the clean surface and in O_h symmetry for the O*. *A*CoO_3 has one more $d_{yz/xz}$ down (or minority) spin electron than *A*FeO_3, and in both cases, the $d_{yz/xz}$ down electron increases with La doping, as denoted with a black dashed arrow in Figure 2.7. After the oxygen atom is adsorbed on the active site, the $d_{yz/xz}$ and $p_{x/y}$ of the intermediate O form the π and π^* orbitals as guided with purple dashed lines in orbital configuration diagram (Figure 2.7). To describe the d orbital configuration change, the minority spin $d_{yz/xz}$ and d_{xy} schematic PDOS of O* are shown in bottom of Figure 2.7. In the PDOS of O*, the light blue lines represent the π and π^* orbitals. As shown by the red filled curve around E_F (bottom of Figure 2.7), the extra minority spin electrons of $d_{yz/xz}$ transfer to d_{xy} rather than the newly formed π^* as shown in the orbital configurations. Moreover, the binding energy difference between Co and Fe active sites, which cannot be explained only by the O 2p center (Figure 2.4), is related to the d_{xy} minority electron. In our wavefunction analysis (Figure 2.8), note that d_{xy} does not form any orbital overlap with the O intermediate. Interestingly, the d_{xy} electrons near E_F mainly constitute antibonding orbitals with the surface lattice oxygen (Figure 2.8). With presence of the OER intermediate, d_{xy} slightly weakens the binding energy indirectly by destabilizing the surface. The intermediate binding energy is mostly affected by the O 2p center and is slightly weaker when the clean active site has more $d_{yz/xz}$ electrons. Furthermore, when the intermediate is adsorbed, more electrons fill the surface antibonding orbital through La doping in the active site; thus, the difference in binding energy between Co and Fe in $LaBO_3$ increases. This is the reason why the O* or HO* adsorption energy is comparable for Fe and Co in the case of $SrBO_3$, and the binding strength is relatively weaker for Co for the same number electrons doped by La. Additionally, the ΔE_{O^*} of $ACo_{0.5}Fe_{0.5}O_3$ is almost the median of the results of $ACoO_3$ and $AFeO_3$. To show the role of the d_{xy} orbital, schematic illustration was prepared in Figure 2.9. The d_{xy} orbital near the Fermi level is related to surface stability due to the its antibonding character with surface lattice oxygen. Compared with Fe active site, the additional electron on the Co active site transfers to the d_{xy} orbital after the O intermediate adsorbed. It is a reason why the $ACoO_3$ shows slightly weaker binding strength compared to $AFeO_3$ as explained in Figure 2.9.

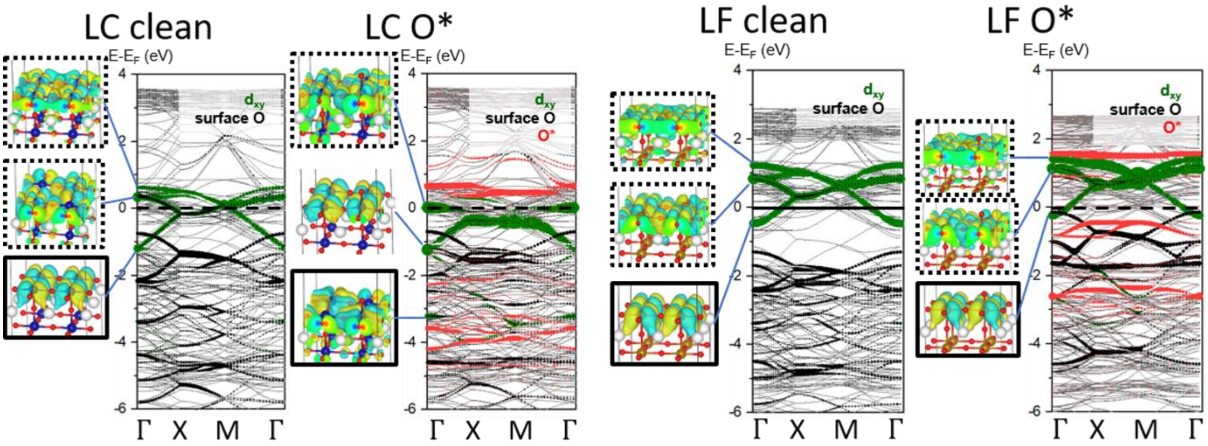

Figure 2.8 The d_{xy} minority spin projected band of $LaCoO_3$ and $LaFeO_3$ for clean surface and O*. Except that d_{xy} is expressed in green, the other notation and color is the same as in Figure 2.6. Through the wavefunction images, dxy electrons form a bond with surface oxygen, and it can be seen that there is almost no overlap with O intermediate states (red projected band). Copyright © 2022 American Chemical Society.

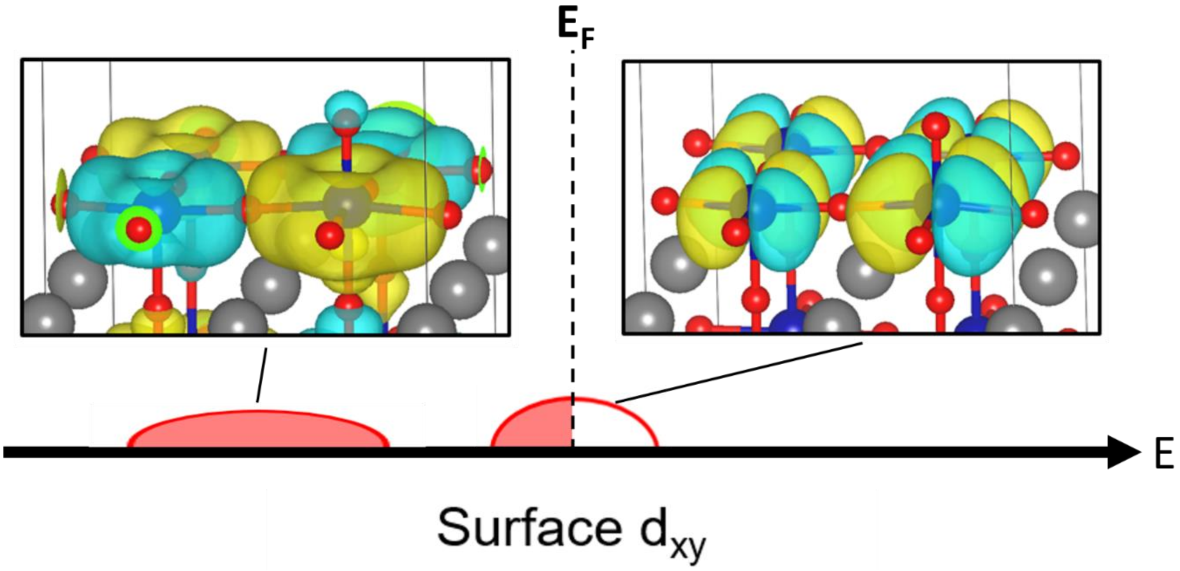

Figure 2.9 Schematic illustration of surface d_{xy} projected DOS of $LaCoO_3$ with its wavefunction image. The wavefunction image near the Fermi level shows that d_{xy} and intermediate O of the active site metal have no overlap (which means non-bonding), and that d_{xy} mainly has antibonding character with surface lattice oxygen. Since the d_{xy} has the antibonding character with surface lattice oxygen, additional electron in Co active site can affect to the surface stability and the intermediate binding strength even though the d_{xy} doesn't form bonding nor antibonding with intermediate species.

2.3.3 Descriptor (E_{2p} – 0.4 E_{dxy})

As shown in Figure 2.9, how many electrons will be occupied in the d_{xy} determines the surface stability and intermediate species binding strength. As well as oxygen 2p band center is important to describe the OER intermediate binding energy or OER performance[7,14,15], our finding suggests that the d_{xy} down spin center level also needs to be considered in OER activity. The bulk descriptor E_{2p} can describe the overall trend, but the descriptor based on ideal or distorted octahedron (O_h) environment lacks details of the electronic structure affected by surface environment. Thus, the E_{2p} descriptor is refined by adding the d_{xy} minority spin band center (E_{dxy}) of active site with respect to the Fermi level. For each $ACo_yFe_{1-y}O_3$, we evaluate E_{2p}, as described before, and add the additional quantity $E_{dxy} = y\,E_{dxy}^{Co} + (1-y)\,E_{dxy}^{Fe}$, where $E_{dxy}^{Co/Fe}$ is obtained from PDOS for y =1 or 0 for Co or Fe, respectively. The new descriptor is defined as E_{2p} – t E_{dxy}, where t is the fitting parameter. Figure 2.10 shows the O and HO binding energies as a function of our new descriptor, where the best fit to our DFT results is obtained for t = 0.4. Since the new descriptor (E_{2p} – 0.4 E_{dxy}) contains information about the perovskite surface stability, it is related to the physical properties related to the surface state. To verify this, the quantitative evaluation of the LOM which is mentioned in Section 1.2.3 was used based on new descriptor (Figure 2.11).

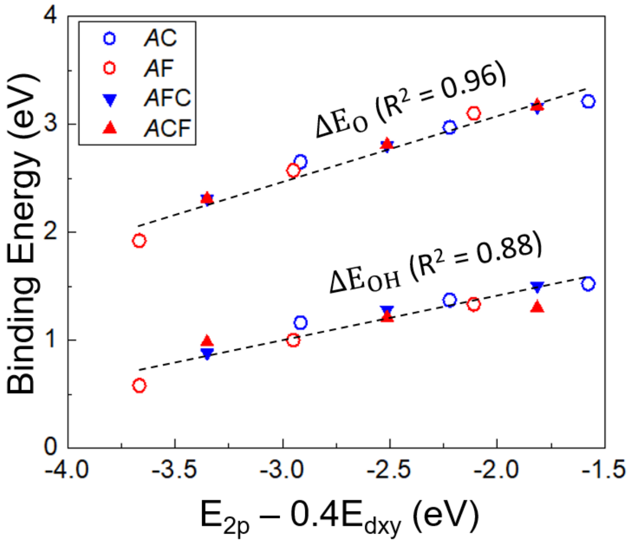

Figure 2.10 The binding energies of HO* and O* as in Figure 2.4 plotted against a new descriptor ($E_{2p} - 0.4\ E_{dxy}$). The color of the symbols indicates the species of the active metal site (red = Fe and blue = Co). The binding energies of *A*FeO$_3$ (*A*F) and *A*CoO$_3$ (*A*C) are represented with open circles, where the mixed case (y = 0.5) are denoted by upward- and downward-facing triangles. Both of notation *A*CF and *A*FC represent *A*Co$_{0.5}$Fe$_{0.5}$O$_3$ composition, the last abbreviation alphabet (C or F) indicates the active *B*-site element. Copyright © 2022 American Chemical Society.

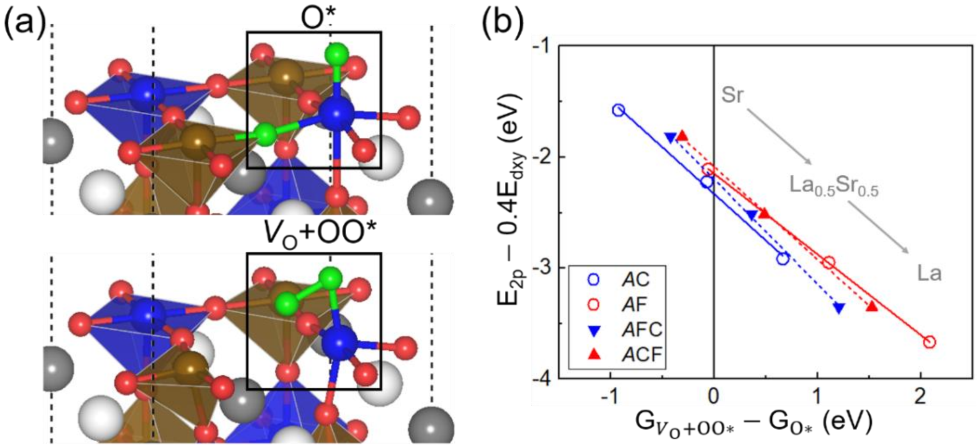

Figure 2.11 (a) Surface structure of the second reaction step (O*) in AEM (upper image) and O vacancy involved surface structure with adsorbate O (V_O+OO*) in LOM (lower image). The green balls represent the adsorbate O and associated lattice O. (b) Correlation between the newly suggested descriptor ($E_{2p} - 0.4\ E_{dxy}$) and the Gibbs free energy difference $\Delta G = G_{V_O+OO*} - G_{O*}$ of V_O+OO* and O* for *AB*O$_3$ without (open circle) or with (upper and lower triangle) Fe–Co mixing for the *B*-site. The blue and red colors denote Co and Fe for the active site metal, respectively. The variation of ΔG with the *A*-site composition, such as x = 0.0, 0.5, and 1.0 for La$_x$Sr$_{1-x}$, follows the lines with the associated color for the active site type. AEM is favored for a more positive value of ΔG ($G_{V_O+OO*} - G_{O*}$). Copyright © 2022 American Chemical Society.

We examined the effect of Fe–Co mixing on the tendency of $LaCoO_3$ to favor AEM over LOM. The criteria for choosing either AEM or LOM is the relative stability of O* with respect to O–O* involving one surface O vacancy, i.e., O* against V_O+OO*, as shown in Figure 2.11a. In Figure 2.11b, the difference between the Gibbs free energies calculated for the two configurations ($\Delta \mathrm{G} = \mathrm{G}_{V_\mathrm{O}+\mathrm{OO}*} - \mathrm{G}_{\mathrm{O}*}$) is plotted on the horizontal axis, while the newly suggested descriptor (E_{2p} – 0.4 E_{dxy}) is plotted on the vertical axis. The new descriptor shows good correlation with the stability of the surface lattice oxygen. Compared to $A\mathrm{CoO}_3$, $A\mathrm{FeO}_3$ exhibits a shift along the right-hand side by ~1.0 eV, signifying a more stable O* state. In the Fe–Co mixed case, the Fe active site (*A*CF) tends more toward AEM than the Co site (*A*FC). The Fe–Co mixed system also shows an intermediate value both in E_{2p} – 0.4 E_{dxy} and ΔG. This result shows that Fe–Co mixing in $AB\mathrm{O}_3$ is helpful for enhancing AEM to obtain stable OER electrocatalysts.

The descriptor of the surface d_{xy} minority spin center and the O 2p band center enables an accurate estimation of the stability of the intermediate species, especially in the presence of Fe–Co mixing. However, it cannot be considered as an effective descriptor since it requires a slab structure calculation to obtain the d_{xy} level (E_{dxy}). Ghiringhelli et al. suggested the following four conditions of a good descriptor[42]: (i) the descriptor uniquely characterizes material properties, (ii) the difference in the value of the descriptor must be commensurate with the difference in properties, (iii) the determination of the descriptor must not involve theoretical (or experimental) processes as intensive as those needed for evaluating the property to be predicted, and (iv) the dimension of the descriptor should be as low as possible.

Due to the inadequacy to condition (iii), we devised a way to obtain a similar quantity through concise bulk system calculations. All *B* atoms of $AB\mathrm{O}_3$ cubic perovskite oxides have O_h symmetry, and the d_{xy} energy level is degenerate with d_{yz}/d_{xz}, named as t_{2g}. According to the bulk $AB\mathrm{O}_3$ calculations, the binding energies of O* and HO* are well described with the O 2p band center and t_{2g} minority spin band center of *B*-metal (Figure 2.12a). As shown in Figure 2.12a, although the calculated system is not the slab structure, using t_{2g} level the prediction quality as good as that in Figure 2.10 can be maintained. Additionally, the new bulk descriptor ($E_{2p} - 0.4\ E_{t2g}$) provide guidance to the OER overpotential, as shown in Figure 2.12b. As indicated by the solid or dashed lines in Figure 2.12b, the overpotential is positively correlated with the bulk descriptor value. However, the line slope slightly varies depending on the composition of the *B*-site and the type of active site. To understand this variance, note that the overpotential is mainly determined by the binding energy difference between O* and HO* (Figure 2.13). In most $AB\mathrm{O}_3$ compositions, forming O* from HO* is a potential determining step (PDS); therefore, stable O* and unstable HO* are desirable for a low overpotential. Figure 2.12a shows that the amount of ΔE_{OH} variation with the *A*-site composition is lower for *A*CF (red upper triangle) than that for *A*F (red open circle). In *A*CF, the surface Co linked to the Fe active site via O slightly destabilizes the HO* binding, thereby reducing the difference in the binding energies of O* and HO* ($\Delta E_O - \Delta E_{OH}$). Notably, the binding energy of O* (ΔE_O) is insensitive to the *B*-site mixing. For the Co active site, *AFC* (blue lower triangle in Figure 2.12a) exhibits greater ΔE_{OH} variation with the *A*-site mixing than *AC* (blue open circle), which leads to the suppressed reduction of the overpotential through the *B*-site mixing. Figure 2.12b shows that the overall amount of overpotential decrease with the *B*-site mixing is greater for Fe than Co active site.

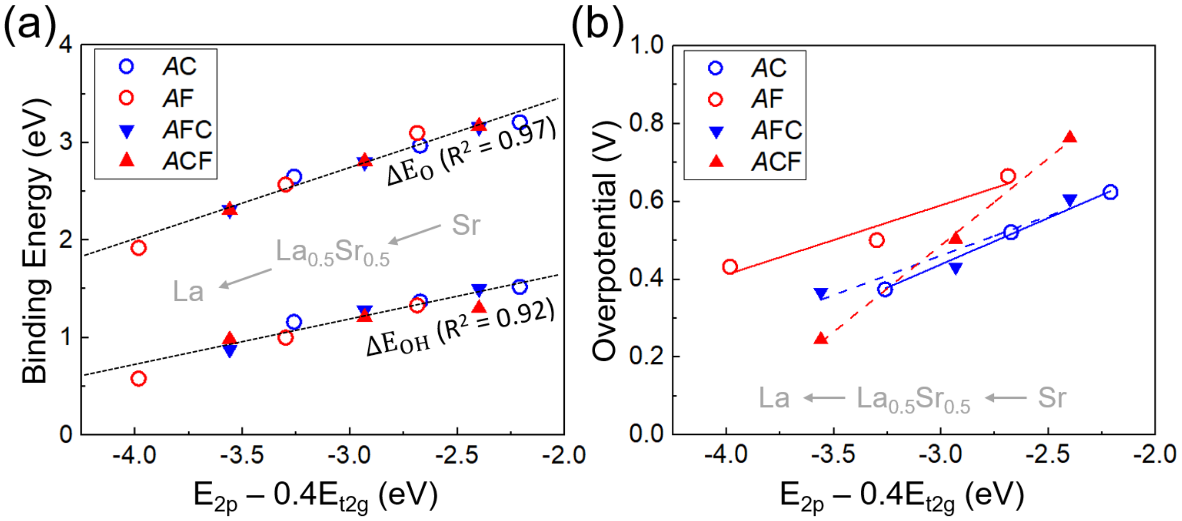

Figure 2.12 (a) Binding energies of HO* and O* versus the new bulk descriptor $E_{2p} - 0.4\ E_{t2g}$, where E_{2p} and E_{t2g} are the O 2p band energy level and t_{2g} minority spin band center relative to E_F, respectively, from the 2 × 2 × 2 cubic supercell calculations. (b) The AEM overpotentials of *AC*, *AF*, *AFC*, and *ACF* (*A* = Sr, $La_{0.5}Sr_{0.5}$, and La) plotted against the descriptor ($E_{2p} - 0.4\ E_{t2g}$). Lines in (a) and (b) are added for guidance. Copyright © 2022 American Chemical Society.

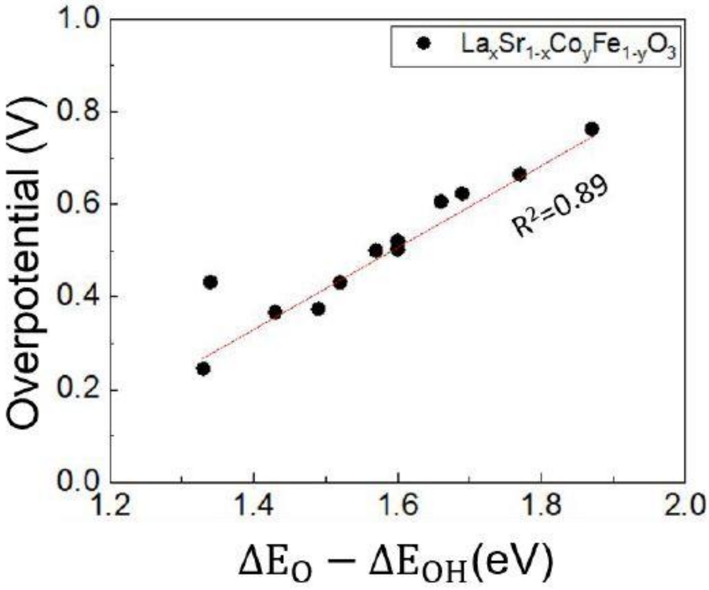

Figure 2.13 In $La_xSr_{1-x}Co_yFe_{1-y}O_3$ (x=0.0, 0.5, 1.0, y=0.0, 0.5), the OER overpotential is plotted by binding energy difference between O* and HO* (**ΔE_O — ΔE_{OH}**). The OER overpotential is based on AEM 4 step reaction (Section 1.2.3). Copyright © 2022 American Chemical Society.

2.3.4 OER activity and Electrocatalyst Design

For the electrocatalyst activity evaluation, Gibbs free energy of each OER step was calculated based on the AEM as described in eq 2.1-2.3. Given the four reaction steps involved in AEM, Nørskov et al. reported the minimum OER overpotential (~0.3 V) achievable for metal oxides owing to the linear scaling relation between HO* and HOO*[17]. In our simulations, the scaling relation is given by $\Delta G_{OOH} = 0.82\ \Delta G_{OH} + 3.40$ (Figure 2.14a), which is consistent with Ref. 17. However, by including the explicit water solvent, the difference between ΔG_{OH} and ΔG_{OOH} can be reduced because the solvation Gibbs free energy (ΔG_{solv}) of HOO* (−0.6 eV) is larger than that of HO* (−0.4 eV) (Table 2.1). This mainly stems from the hydrogen bonds of the OER intermediates with the water molecules, because O* does not exhibit such stabilization. Figure 2.14b shows the scaling relation between HO* and HOO* under the explicit solvent condition. After including the solvent effect, the slope of $\Delta G_{OOH}/\Delta G_{OH}$ is 0.79, which is slightly less than 1, and the intercept becomes 3.17, which is about 0.2 smaller than that without the solvent.

Based on the relation between ΔG_{OOH} and ΔG_{OH} ($\Delta G_{OOH} = 0.79\ \Delta G_{OH} + 3.17$), we plot the overpotential contour map in Figure 2.15a; the optimal point is indicated by the filled star. The *A*CF and *A*F values, corresponding to the Fe active site, are represented with open and filled circles, respectively, to show the drastic effect of Co mixing, where the results of minor variation for the Co active are shown in Figure 2.15b. The figure shows that $A\mathrm{Co_{0.5}Fe_{0.5}O_3}$ (black open circles and line) is closer to the optimal point than $A\mathrm{FeO_3}$ (gray filled circles and line). As shown in Figure 2.12b and Figure 2.13, the destabilization of HO* by Co nearby Fe active site explains the closer proximity of *A*CF than *A*F to the optimal point. Among the various compositions calculated for ABO_3, the lowest overpotential of 0.245 V was obtained for $LaCo_{0.5}Fe_{0.5}O_3$.

Figure 2.16 displays the Gibbs energies (ΔG_1, ΔG_2, and ΔG_3) of the three reaction steps for $La_xSr_{1-x}Co_yFe_{1-y}O_3$ (x, y = 0.0, 0.25, 0.5, 0.75 or 1.0) as a function of x. The PDS is ΔG_2 for most catalysts due to the less stable O*, except $LaFeO_3$ and $LaCo_{0.5}Fe_{0.5}O_3$ whose PDS is ΔG_3. For all cases, the overpotential corresponding to Max(ΔG_1, ΔG_2, ΔG_3) relative to the horizontal dashed line at 1.23 decreases with La doping. For the Co active site, ΔG_2 remains the highest for whole range of x. This suggests that enhanced binding of the intermediate species is desirable for a lower overpotential. This can be achieved by additional Fe doping than LFC. For example, $La_{0.75}Sr_{0.25}Fe_{0.75}Co_{0.25}O_3$ has the lowest overpotential (η_{OER} = 0.289 V) among the Co active materials (Figure 2.16). For the Fe active site, the intermediate binding is relatively strong; thus, *A*F has a higher overpotential than *A*CF, as shown in Figure 2.15. Hence, under the same *A* composition, the overpotential decreases with Fe–Co mixing. An overpotential of less than 0.3 V is predicted for $LaCo_{0.5}Fe_{0.5}O_3$ (LCF) and $La_{0.75}Sr_{0.25}Fe_{0.75}Co_{0.25}O_3$, and 19 other compositions yield η_{OER} less than 0.5 V (Table 2.3).

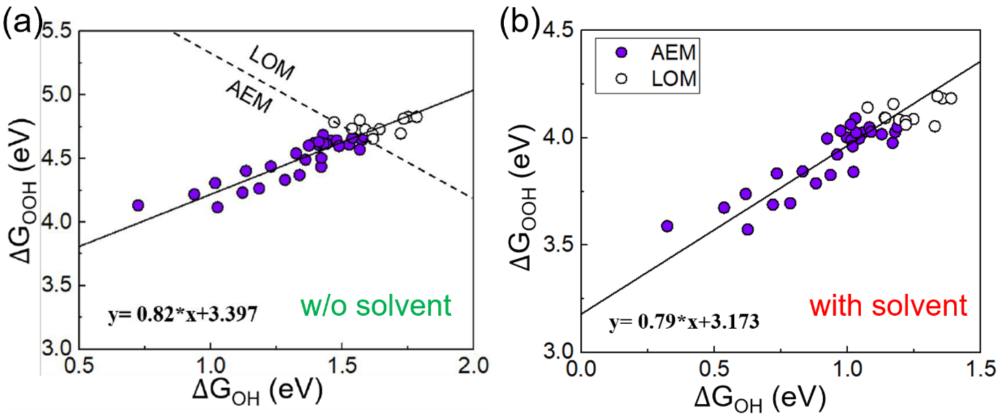

Figure 2.14 Gibbs free energy of HOO* plotted against the Gibbs free energy of HO* calculated for $La_xSr_{1-x}Co_yFe_{1-y}O_3$ (x, y = 0.0, 0.25, 0.5, 0.75, or 1.0) (a) without explicit solvent condition and (b) with explicit solvent. The solid lines indicate the lines fitting by (a) $\Delta G_{OOH} = 0.82\Delta G_{OH} + 3.397$ and (b) $\Delta G_{OOH} = 0.79\Delta G_{OH} + 3.173$. To differentiate the OER reaction path favored for each material, the AEM and LOM types are denoted by filled and open circles, respectively. Copyright © 2022 American Chemical Society.

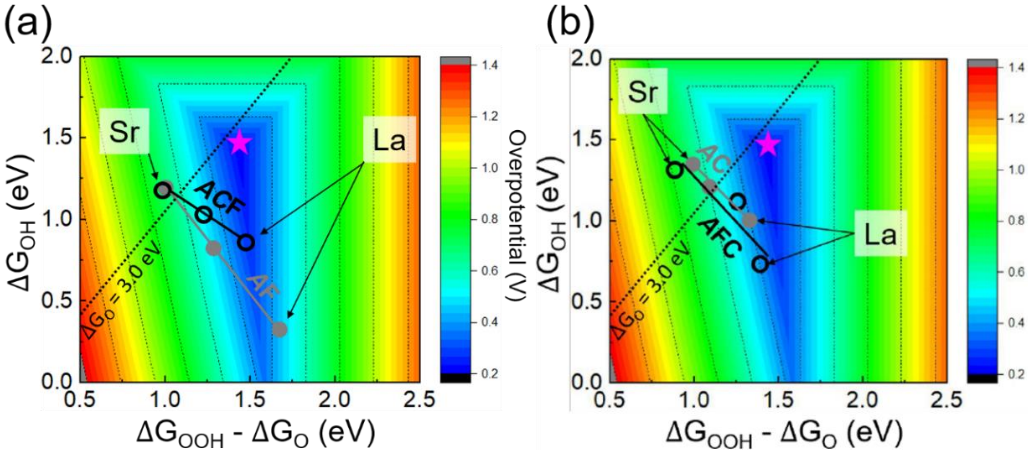

Figure 2.15 (a) Overpotential contour map based on the scaling relation ($\Delta G_{OOH} = 0.79\Delta G_{OH} + 3.173$). The gray filled circles and line correspond to $La_xSr_{1-x}FeO_3$ calculated for x = 0.0, 0.5, or 1.0 and the guidance to eye, respectively. Similarly, the black open circles and line denote the case for $La_xSr_{1-x}Co_{0.5}Fe_{0.5}O_3$. The former and latter are denoted as *A*F and *A*CF, respectively, with the left- and right-end corresponding to Sr and La, respectively, for the *A*-site. The pink star indicates the most optimal point with an overpotential of 0.21 V. The black dashed line represents the $\Delta G_O = 3.0$ eV corresponding to the boundary of the two regions favoring AEM (lower-right) and LOM (upperleft). (b) Overpotential contour map based on the scaling relation as same with (a). The gray filled circle and line show the points of $La_xSr_{1-x}CoO_3$ (x=0.0, 0.5, 1.0) and its trend line. Fe-Co half mixed cases are represented as the black open circle and the trend of the $AFe_{0.5}Co_{0.5}O_3$ is denoted by the black solid line as denoted by *A*C and *A*FC. Among the 6 points, LSFC (η_{LSFC} = 0.43 V) is closest to the optimal point (pink star, $\boldsymbol{\eta}$ = 0.21 V). Copyright © 2022 American Chemical Society.

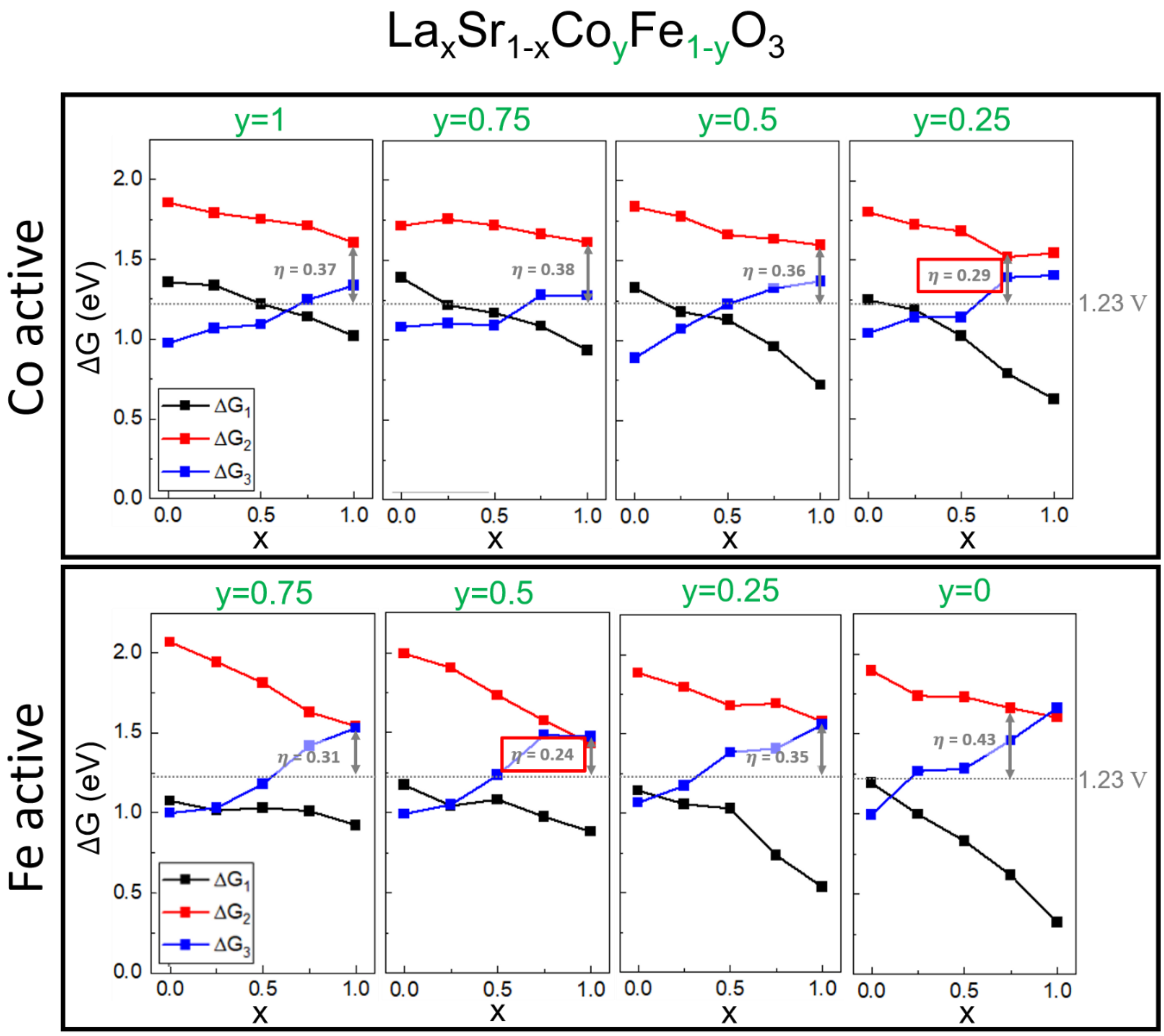

Figure 2.16 Gibbs free energy difference (ΔG) as function of x and y in $La_xSr_{1-x}Co_yFe_{1-y}O_3$. Top boxes present the results for the Co active site, while the remaining bottom boxes present the results for the Fe active site. The highest ΔG is a PDS and the discrepancy between the highest free energy step and 1.23 V (gray dashed line) determines the theoretical overpotential. The lowest overpotential according to *A* variation is indicated by a gray double arrow in each *B* composition with its value. For all the plotted free energies, the water solvent is explicitly included. In each active site, the lowest overpotential is denoted by red rectangle. Copyright © 2022 American Chemical Society.

Table 2.3 Gibbs free energy table with explicit solvent. The abbreviation capital alphabet represents L = La, S = Sr, C = Co, F = Fe. For convenience, like $La_{0.25}Sr_{0.75}Co_{0.75}Fe_{0.25}O_3$, 1:3 ratio mixing of *A*-/*B*-site is expressed as L1S3C3F1 and the last abbreviation indicates the active *B*-site metal. (Unit: eV)

		ΔG_{OH}	ΔG_{O}	ΔG_{OOH}	**Overpotential (V)**
1	SC	1.3562	3.210039	4.183705	0.62384
2	SF1C3	1.3892	3.103359	4.184365	0.48416
3	SFC	1.32826	3.164279	4.053725	0.60602
4	SF3C1	1.24787	3.047829	4.087485	0.56996
5	SF	1.19381	3.088829	4.084585	0.66502
6	SC1F3	1.14259	3.026819	4.093025	0.65423
7	SCF	1.17217	3.165499	4.157895	0.76333
8	SC3F1	1.07552	3.142669	4.141835	0.83715
9	L1S3C	1.337204	3.12691	4.194077	0.559707
10	L1S3F1C3	1.217894	2.97316	4.078327	0.525267
11	L1S3FC	1.179234	2.9549	4.027237	0.545667
12	L1S3F3C1	1.187814	2.90946	4.050197	0.491647
13	L1S3F	0.997704	2.73439	4.001807	0.506687
14	L1S3C1F3	1.058274	2.85249	4.025127	0.564217
15	L1S3CF	1.043654	2.94778	3.997507	0.674127
16	L1S3C3F1	1.014634	2.95864	3.990117	0.714007
17	LSC	1.219578	2.970372	4.061119	0.520794
18	LSF1C3	1.169508	2.886712	3.976399	0.487204
19	LSFC	1.128718	2.790452	4.016679	0.431734
20	LSF3C1	1.022628	2.702492	3.841509	0.449864
21	LSF	0.831388	2.561862	3.843739	0.500474
22	LSC1F3	1.029408	2.707312	4.091289	0.447904
23	LSCF	1.082268	2.815522	4.049139	0.503254
24	LSC3F1	1.031638	2.843952	4.024169	0.582314
25	L3S1C	1.139692	2.848633	4.094081	0.478941
26	L3S1F1C3	1.088372	2.748653	4.028511	0.430281
27	L3S1FC	0.961352	2.596513	3.922611	0.405161
28	L3S1F3C1	0.785132	2.304113	3.695311	0.288981
29	L3S1F	0.617762	2.278453	3.738611	0.430691
30	L3S1C1F3	0.734932	2.426133	3.833871	0.461201
31	L3S1CF	0.973712	2.548133	4.032861	0.344421
32	L3S1C3F1	1.011802	2.642013	4.061321	0.400211
33	LC	1.019586	2.623854	3.960233	0.374268
34	LF1C3	0.936476	2.548694	3.826633	0.382218
35	LFC	0.719876	2.316994	3.688513	0.367118
36	LF3C1	0.625356	2.169164	3.572113	0.313808
37	LF	0.323249	1.925844	3.588013	0.432169
38	LC1F3	0.536591	2.114944	3.674093	0.348353
39	LCF	0.881456	2.312664	3.788053	0.245389
40	LC3F1	0.923756	2.466094	3.996913	0.312338

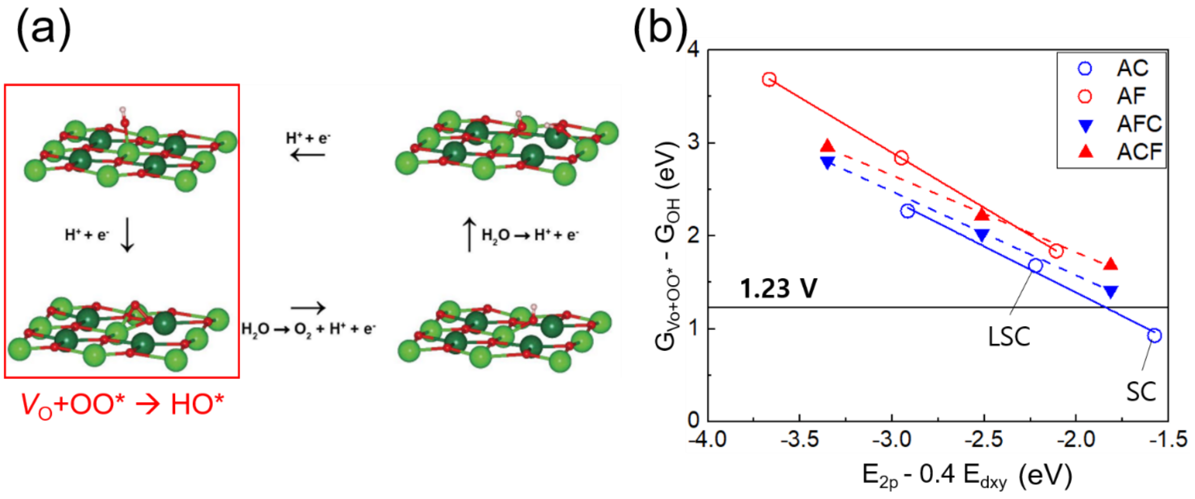

Figure 2.17 (a) Oxygen evolution reaction via the lattice-oxygen participation mechanism on the LSC surface. Red, pink, bright green, and dark green spheres represent oxygen, hydrogen, lanthanum, and strontium atoms, respectively. The top-left, bottom-left, bottom-right, and top-right structures indicate OH*, (V_O+OO)*, (V_O+OH)*, and (H_O+OH)* adsorbed on the LSC (001) surface, respectively. Nature Communications, Copyright © 2021, Nam Khen Oh et al. (b) Gibbs free energy difference ($G_{V_{O+OO*}} - G_{OH}$) as function of suggested new descriptor (E_{2p} – 0.4 E_{dxy}). The Gibbs free energy difference is mainly related to potential determining step (PDS) of the lattice oxygen participated mechanism (LOM). Black solid line indicates potential of 1.23 V which could be the reference for optimal LOM materials in order to satisfy the Sabatier principle.

Since the newly proposed descriptor is related to the surface oxygen stability (Figure 2.11b), it can verify the possibility of LOM. To approximately estimate the OER activity in LOM based on the newly suggested descriptor (E_{2p} – 0.4 E_{dxy}), we briefly plotted the Gibbs free energy difference between the V_O+OO* structure and the HO* structure, which is usually the PDS in LOM (Figure 2.17). To satisfy the Sabatier principle, the Gibbs free energy difference ($G_{V_{O+OO*}} - G_{OH}$) needs to be an appropriate value that is neither too small nor too large. For an ideal catalyst design, the free energy difference should be close to 1.23 V. As shown in Figure 2.17, since the new descriptor exhibits a linear correlation with the free energy difference, the electrocatalyst can be designed with the new descriptor even in LOM.

Figure 2.18 shows the O binding energies of different 3d transition metals (*B* = Cr, Mn, Fe, Co, Ni and Cu) in $LaBO_3$ to confirm the extensibility of the descriptor applied in $La_xSr_{1-x}Co_yFe_{1-y}O_3$. As a result, our descriptor could predict the binding energies of O* for $LaMnO_3$, $LaNiO_3$, and $LaNi_{0.5}Fe_{0.5}O_3$ well while the O p-band center failed to predict them as can be seen in Figure 2.18a, b. However, we found that the binding energies of O* for $LaCrO_3$ and $LaCuO_3$ are not lying on the trend line. This is mainly due to because the number of insufficient (e.g. $LaCrO_3$) or too many (e.g. $LaCuO_3$)

number of 3d electrons of each cation does not cause transfer of minority spin electrons to the d_{xy} orbital upon chemisorption of O or OH. For example, as shown in Figure 2.18c, d, the d_{xy} orbital remains completely empty or occupied for $LaCrO_3$ or $LaCuO_3$, respectively, whereas the others exhibit variation in the occupation. If the 3d electrons are insufficient as $LaCrO_3$, the d_{xy} orbital cannot be filled with electrons during the reaction. On the other hand, if the 3d electrons are enough like $LaCuO_3$, the d_{xy} orbital is fully occupied already and is not involved to the adsorption of intermediates (Figure 2.18 c, d). Still, it could be different if other cations like Mn, Ni, Fe, or Co is mixed in these materials.

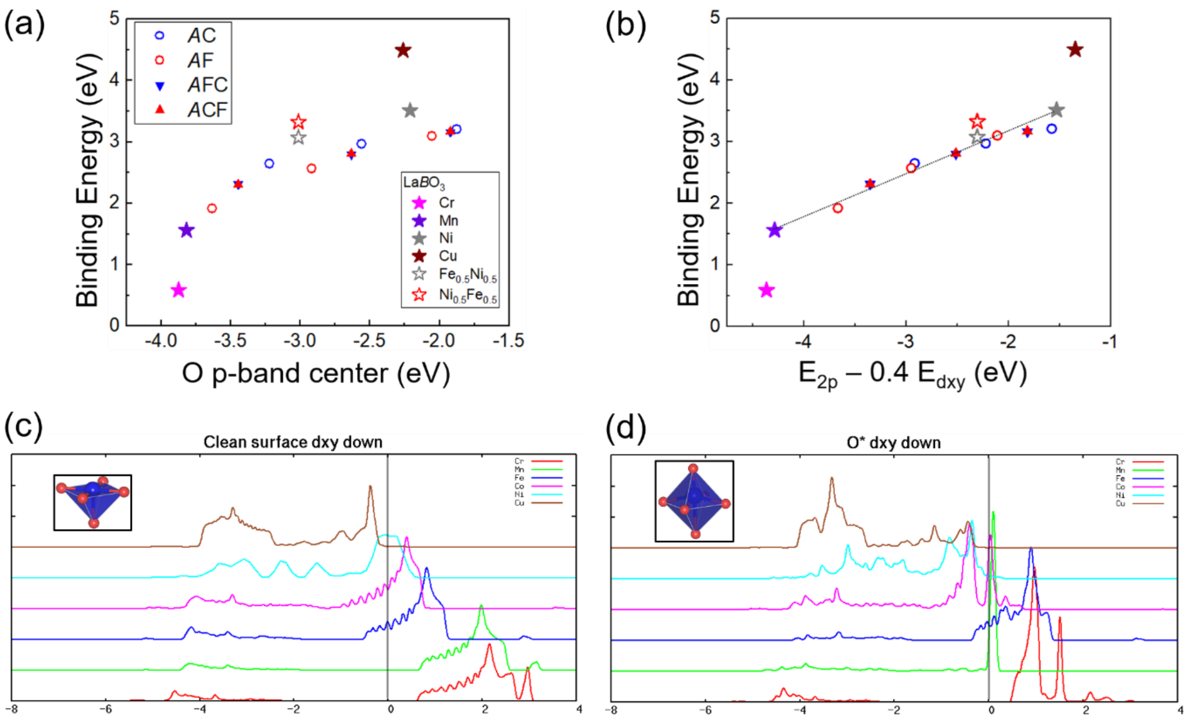

Figure 2.18 Calculated binding energies of O* as a function of (a) O p-band center and (b) new descriptor E_{2p} - 0.4 E_{dxy}. The binding energy for AFeO$_3$/ACoO$_3$ and ACo$_y$Fe$_{1-y}$O$_3$ (A=La$_x$Sr$_{1-x}$; x, y = 0.0, 0.5, 1.0) are shown in open circles and triangles, respectively. The color of open circles and triangles indicates the species of active metal site (red = Fe, blue = Co). The additional calculated binding energies of O* for $LaCrO_3$ (pink star), $LaMnO_3$ (purple star), $LaNiO_3$ (gray star), $LaCuO_3$ (brown star) and $LaNi_{0.5}Fe_{0.5}O_3$ (gray and red open star) are shown together. In LaBO$_3$ (B = Cr, Mn, Fe, Co, Ni, and Cu), surface B-atom d_{xy} down spin orbital projected DOS for (c) clean surface and (d) O*. As O intermediate is adsorbed, d_{xy} down orbital starts to be filled in Mn and completely filled in Ni. However, in Cr, d_{xy} down orbital is not filled in both the clean surface and O*. Conversely, in Cu, even from the clean surface, d_{xy} orbital is fully filled. This means that the Cr and Cu OER intermediate binding strengths are independent of d_{xy}. This is the reason why $LaCrO_3$ and $LaCuO_3$ cannot be described by our new descriptor.

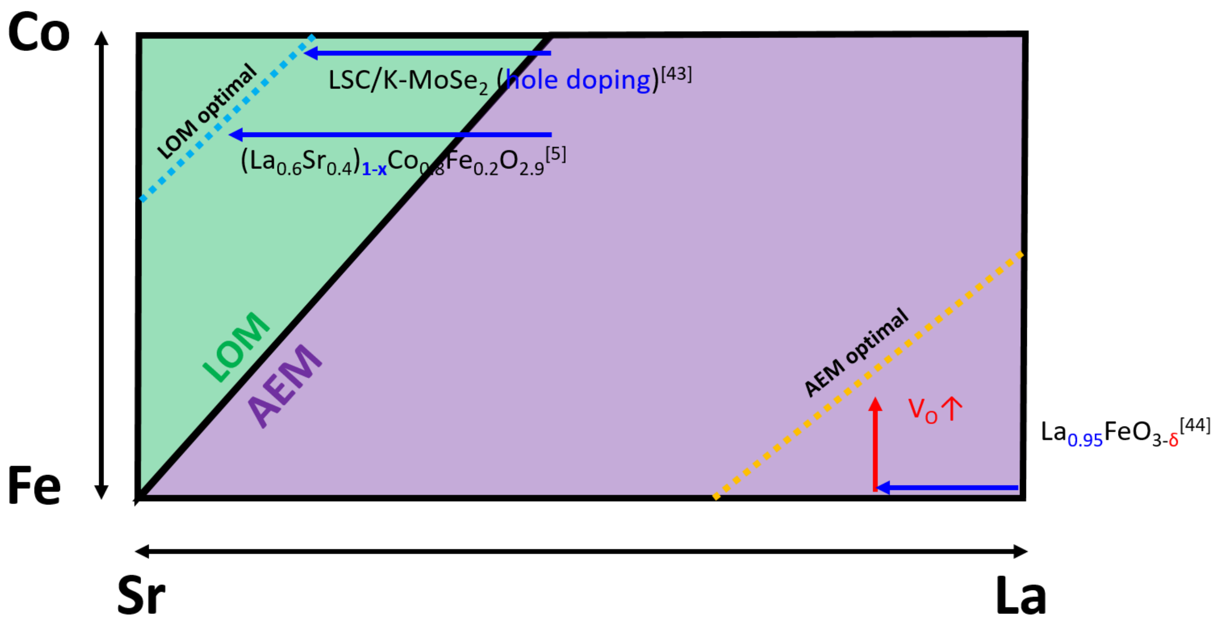
Co
Fe
Sr
La
LOM optimal
LSC/K-$MoSe_2$ (hole doping)[43]
$(La_{0.6}Sr_{0.4})_{1-x}Co_{0.8}Fe_{0.2}O_{2.9}$[5]
LOM
AEM
AEM optimal
V_O↑
$La_{0.95}FeO_{3-\delta}$[44]

Figure 2.19 Based on our calculation results, the AEM and LOM boundary line according to *A*-/*B*-mixing is presented. The upper left green area composition is expected to follow LOM and the lower right purple area is expected to follow AEM. The dashed line in each area represents the line where optimal overpotential could appear. The *A*-mixing can correspond to the effect of hole (or electron) doping through the hetero stack, where the amount of non-local or free carriers determines the doping concentration. Whereas, the *B*-mixing can explain the local effect of oxygen vacancy as it affects the amount of local 3d electrons. The AEM optimal line is estimated from Figure 2.12b and the LOM optimal line is deducted by the Figure 2.17b results. (Reference information, [5], [43], [44])

To evaluate whether our calculations are able to depict heterostructure or oxygen vacancy effect, we qualitatively compared our calculation expectations with relevant experimental reports that enhanced OER performance through the introduction of heterostructure or O vacancy in Figure 2.19. In Ref 43, LOM boosting through the hole doping in $La_{0.5}Sr_{0.5}CoO_{3-\delta}$ can be explained by controlling free electrons as represented in the Figure 2.19 upper blue arrow line. The OER performance improvement through *A*-site defect in $La_{0.6}Sr_{0.4}Co_{0.8}Fe_{0.2}O_{2.9}$[5] can be understood qualitatively as the amount of free electron decreases (Figure 2.19). In addition, the OER activity enhancement of $La_{0.95}FeO_{3-\delta}$[44] can be understood as approaching the AEM optimal line through the introduction of O vacancy and *A*-site defect (Figure 2.19). Based on the mapping in Figure 2.19, OER electrocatalyst can be designed and guided toward desired direction which is close to the optimal point.

2.4 Conclusion

Our study investigated the effects of Fe–Co mixing on the OER performance in a double perovskite electrocatalyst. The lattice oxygen 2p band center and surface d_{xy} minority spin band center determines the binding energies of intermediate species in double perovskite catalysts. In ABO_3 cubic perovskite, the clean surface d_{xy} minority spin band near the Fermi level has an antibonding characteristic that is related to surface stability. We suggested the combination of lattice oxygen 2p band center and surface *B* metal d_{xy} minority electron center as a binding energy descriptor, which contains both bulk property (E_{2p}) and surface property (E_{dxy}). The proposed descriptor can be obtained via simple cubic bulk structure calculation ($E_{2p} - 0.4\ E_{t2g}$), and it satisfies the conditions for a good descriptor by exhibiting very low computational cost and prominent predictability. Moreover, we found that a robust perovskite oxide OER electrocatalyst with low overpotential (< 0.3 V) can be produced based on AEM by Fe–Co mixing. Based on our finding, we suggest $La_xSr_{1-x}Co_yFe_{1-y}O_3$ double perovskites, which yield comparably low overpotentials based on AEM. $LaCo_{0.5}Fe_{0.5}O_3$ and $La_{0.75}Sr_{0.25}Fe_{0.75}Co_{0.25}O_3$ have low overpotentials of 0.245 and 0.289 V, respectively.

2.5 References

(1) Suntivich, J.; May, K. J.; Gasteiger, H. A.; Goodenough, J. B.; Shao-horn, Y.; Calle-vallejo, F.; Oscar, A. D.; Kolb, M. J.; Koper, M. T. M.; Suntivich, J.; May, K. J.; Gasteiger, H. A.; Goodenough, J. B.; Shao-horn, Y. A Perovskite Oxide Optimized for Molecular Orbital Principles. *Science* **2011**, *334* (6061), 1383–1385.

(2) Hwang, J.; Rao, R. R.; Giordano, L.; Katayama, Y.; Yu, Y.; Shao-Horn, Y. Perovskites in Catalysis and Electrocatalysis. *Science* **2017**, *358* (6364), 751–756.

(3) Shi, Z.; Wang, X.; Ge, J.; Liu, C.; Xing, W. Fundamental Understanding of the Acidic Oxygen Evolution Reaction: Mechanism Study and State-of-the-Art Catalysts. *Nanoscale* **2020**, *12* (25), 13249–13275.

(4) Grimaud, A.; Diaz-Morales, O.; Han, B.; Hong, W. T.; Lee, Y. L.; Giordano, L.; Stoerzinger, K. A.; Koper, M. T. M.; Shao-Horn, Y. Activating Lattice Oxygen Redox Reactions in Metal Oxides to Catalyse Oxygen Evolution. *Nat. Chem.* **2017**, *9* (5), 457–465.

(5) Li, N.; Guo, J.; Ding, Y.; Hu, Y.; Zhao, C.; Zhao, C. Direct Regulation of Double Cation Defects at the A1A2 Site for a High-Performance Oxygen Evolution Reaction Perovskite Catalyst. *ACS Appl. Mater. Interfaces* **2021**, *13* (1), 332–340.

(6) Kim, B. J.; Fabbri, E.; Abbott, D. F.; Cheng, X.; Clark, A. H.; Nachtegaal, M.; Borlaf, M.; Castelli, I. E.; Graule, T.; Schmidt, T. J. Functional Role of Fe-Doping in Co-Based Perovskite Oxide Catalysts for Oxygen Evolution Reaction. *J. Am. Chem. Soc.* **2019**, *141* (13), 5231–5240.

(7) Rong, X.; Parolin, J.; Kolpak, A. M. A Fundamental Relationship between Reaction Mechanism and Stability in Metal Oxide Catalysts for Oxygen Evolution. *ACS Catal.* **2016**, *6* (2), 1153–1158.

(8) Duan, Y.; Sun, S.; Xi, S.; Ren, X.; Zhou, Y.; Zhang, G.; Yang, H.; Du, Y.; Xu, Z. J. Tailoring the Co 3d-O 2p Covalency in $LaCoO_3$ by Fe Substitution to Promote Oxygen Evolution Reaction. *Chem. Mater.* **2017**, *29* (24), 10534–10541.

(9) Cheng, X.; Fabbri, E.; Nachtegaal, M.; Castelli, I. E.; El Kazzi, M.; Haumont, R.; Marzari, N.; Schmidt, T. J. Oxygen Evolution Reaction on $La_{1-x}Sr_xCoO_3$ Perovskites: A Combined Experimental and Theoretical Study of Their Structural, Electronic, and Electrochemical Properties. *Chem. Mater.* **2015**, *27* (22), 7662–7672.

(10) Petrov, A. N.; Kononchuk, O. F.; Andreev, A. V.; Cherepanov, V. A.; Kofstad, P. Crystal Structure, Electrical and Magnetic Properties of $La_{1-x}Sr_xCoO_{3-y}$. *Solid State Ionics* **1995**, *80* (3–4), 189–199.

(11) Shen, Z.; Qu, M.; Shi, J.; Oropeza, F. E.; de la Peña O’Shea, V. A.; Gorni, G.; Tian, C. M.; Hofmann, J. P.; Cheng, J.; Li, J.; Zhang, K. H. L. Correlating the Electronic Structure of Perovskite $La_{1-x}Sr_xCoO_3$ with Activity for the Oxygen Evolution Reaction: The Critical Role of Co 3d Hole State. *J. Energy Chem.* **2022**, *65*, 637–645.

(12) Chakrabarti, B.; Birol, T.; Haule, K. Role of Entropy and Structural Parameters in the Spin-State Transition of $LaCoO_3$. *Phys. Rev. Mater.* **2017**, *1* (6), 1–8.

(13) Wang, X.; Gao, X. J.; Qin, L.; Wang, C.; Song, L.; Zhou, Y. N.; Zhu, G.; Cao, W.; Lin, S.; Zhou, L.; Wang, K.; Zhang, H.; Jin, Z.; Wang, P.; Gao, X.; Wei, H. E_g Occupancy As an Effective Descriptor for the Catalytic Activity of Perovskite Oxide-Based Peroxidase Mimics. *Nat. Commun.* **2019**, *10* (1), 1–8.

(14) Dickens, C. F.; Montoya, J. H.; Kulkarni, A. R.; Bajdich, M.; Nørskov, J. K. An Electronic Structure Descriptor for Oxygen Reactivity at Metal and Metal-Oxide Surfaces. *Surf. Sci.* **2019**, *681*, 122–129.

(15) Jacobs, R.; Hwang, J.; Shao-Horn, Y.; Morgan, D. Assessing Correlations of Perovskite Catalytic Performance with Electronic Structure Descriptors. *Chem. Mater.* **2019**, *31* (3), 785–797.

(16) Grimaud, A.; May, K. J.; Carlton, C. E.; Lee, Y. L.; Risch, M.; Hong, W. T.; Zhou, J.; Shao-Horn, Y. Double Perovskites as a Family of Highly Active Catalysts for Oxygen Evolution in Alkaline Solution. *Nat. Commun.* **2013**, *4* (May), 1–7.

(17) Man, I. C.; Su, H. Y.; Calle-Vallejo, F.; Hansen, H. A.; Martínez, J. I.; Inoglu, N. G.; Kitchin, J.; Jaramillo, T. F.; Nørskov, J. K.; Rossmeisl, J. Universality in Oxygen Evolution Electrocatalysis on Oxide Surfaces. *ChemCatChem* **2011**, *3* (7), 1159–1165.

(18) Weng, B.; Song, Z.; Zhu, R.; Yan, Q.; Sun, Q.; Grice, C. G.; Yan, Y.; Yin, W. J. Simple Descriptor Derived from Symbolic Regression Accelerating the Discovery of New Perovskite Catalysts. *Nat. Commun.* **2020**, *11* (1), 1–8.

(19) Haverkort, M. W.; Hu, Z.; Cezar, J. C.; Burnus, T.; Hartmann, H.; Reuther, M.; Zobel, C.; Lorenz, T.; Tanaka, A.; Brookes, N. B.; Hsieh, H. H.; Lin, H. J.; Chen, C. T.; Tjeng, L. H. Spin State Transition in $LaCoO_3$ Studied Using Soft X-Ray Absorption Spectroscopy and Magnetic Circular Dichroism. *Phys. Rev. Lett.* **2006**, *97* (17), 38–41.

(20) Kresse, G.; Furthmüller, J. Efficient Iterative Schemes for Ab Initio Total-Energy Calculations Using a Plane-Wave Basis Set. *Phys. Rev. B - Condens. Matter Mater. Phys.* **1996**, *54* (16), 11169–11186.

(21) Hammer, B.; Hansen, L. B.; Nørskov, J. K. Improved Adsorption Energetics within Density-Functional Theory Using Revised Perdew-Burke-Ernzerhof Functionals. *Phys. Rev. B - Condens. Matter Mater. Phys.* **1999**, *59* (11), 7413–7421.

(22) Long, Y.; Kaneko, Y.; Ishiwata, S.; Taguchi, Y.; Tokura, Y. Synthesis of Cubic SrCoO3 Single Crystal and Its Anisotropic Magnetic and Transport Properties. *J. Phys. Condens. Matter* **2011**, *23* (24), 0–6.

(23) Blasco, J.; Stankiewicz, J.; García, J. Phase Segregation in the $Gd_{1-x}Sr_xFeO_{3-\delta}$ Series. *J. Solid State Chem.* **2006**, *179* (3), 898–908.

(24) Sommer, L. H.; Tyler, L. J. Steric Effects of the T-Butyl Group in Organosilicon Compounds. *J. Am. Chem. Soc.* **1954**, *76* (4), 1030–1033.

(25) Koehler, W. C.; Wollan, E. O. Neutron-Diffraction Study of the Magnetic Properties of Perovskite-like Compounds $LaBO_3$. *J. Phys. Chem. Solids* **1957**, *2* (2), 100–106.

(26) Rossmeisl, J.; Qu, Z. W.; Zhu, H.; Kroes, G. J.; Nørskov, J. K. Electrolysis of Water on Oxide Surfaces. *J. Electroanal. Chem.* **2007**, *607* (1–2), 83–89.

(27) Pan, Y.; Xu, X.; Zhong, Y.; Ge, L.; Chen, Y.; Veder, J. P. M.; Guan, D.; O'Hayre, R.; Li, M.; Wang, G.; Wang, H.; Zhou, W.; Shao, Z. Direct Evidence of Boosted Oxygen Evolution over Perovskite by Enhanced Lattice Oxygen Participation. *Nat. Commun.* **2020**, *11* (1), 1–10.

(28) Kim, B. J.; Fabbri, E.; Borlaf, M.; Abbott, D. F.; Castelli, I. E.; Nachtegaal, M.; Graule, T.; Schmidt, T. J. Oxygen Evolution Reaction Activity and Underlying Mechanism of Perovskite Electrocatalysts at Different PH. *Mater. Adv.* **2021**, *2* (1), 345–355.

(29) Gauthier, J. A.; Dickens, C. F.; Chen, L. D.; Doyle, A. D.; Nørskov, J. K. Solvation Effects for Oxygen Evolution Reaction Catalysis on IrO_2(110). *J. Phys. Chem. C* **2017**, *121* (21), 11455–11463.

(30) Siahrostami, S.; Vojvodic, A. Influence of Adsorbed Water on the Oxygen Evolution Reaction on Oxides. *J. Phys. Chem. C* **2015**, *119* (2), 1032–1037.

(31) Nørskov, J. K.; Rossmeisl, J.; Logadottir, A.; Lindqvist, L.; Kitchin, J. R.; Bligaard, T.; Jónsson, H. Origin of the Overpotential for Oxygen Reduction at a Fuel-Cell Cathode. *J. Phys. Chem. B* **2004**, *108* (46), 17886–17892.

(32) Tripković, V.; Skúlason, E.; Siahrostami, S.; Nørskov, J. K.; Rossmeisl, J. The Oxygen Reduction Reaction Mechanism on Pt(1 1 1) from Density Functional Theory Calculations. *Electrochim. Acta* **2010**, *55* (27), 7975–7981.

(33) Karlberg, G. S. Adsorption Trends for Water, Hydroxyl, Oxygen, and Hydrogen on Transition-Metal and Platinum-Skin Surfaces. *Phys. Rev. B - Condens. Matter Mater. Phys.* **2006**, *74* (15), 3–6.

(34) Calle-Vallejo, F.; Martínez, J. I.; Rossmeisl, J. Density Functional Studies of Functionalized Graphitic Materials with Late Transition Metals for Oxygen Reduction Reactions. *Phys. Chem. Chem. Phys.* **2011**, *13* (34), 15639–15643.

(35) Liu, S.; White, M. G.; Liu, P. Mechanism of Oxygen Reduction Reaction on Pt(111) in Alkaline Solution: Importance of Chemisorbed Water on Surface. *J. Phys. Chem. C* **2016**, *120* (28), 15288–15298.

(36) Briquet, L. G. V.; Sarwar, M.; Mugo, J.; Jones, G.; Calle-Vallejo, F. A New Type of Scaling Relations to Assess the Accuracy of Computational Predictions of Catalytic Activities Applied to the Oxygen Evolution Reaction. *ChemCatChem* **2017**, *9* (7), 1261–1268.

(37) Goedecker, S. Minima Hopping: An Efficient Search Method for the Global Minimum of the Potential Energy Surface of Complex Molecular Systems. *J. Chem. Phys.* **2004**, *120* (21), 9911–9917.

(38) Goedecker, S. Minima Hopping: An Efficient Search Method for the Global Minimum of the Potential Energy Surface of Complex Molecular Systems. *J. Chem. Phys.* **2004**, *120* (21), 9911–9917.

(39) Mefford, J. T.; Rong, X.; Abakumov, A. M.; Hardin, W. G.; Dai, S.; Kolpak, A. M.; Johnston, K. P.; Stevenson, K. J. Water Electrolysis on $La_{1-x}Sr_xCoO_{3-\delta}$ Perovskite Electrocatalysts. *Nat. Commun.* **2016**, *7*, 11053.

(40) Suntivich, J.; Hong, W. T.; Lee, Y. L.; Rondinelli, J. M.; Yang, W.; Goodenough, J. B.; Dabrowski, B.; Freeland, J. W.; Shao-Horn, Y. Estimating Hybridization of Transition Metal and Oxygen States in Perovskites from o k -Edge X-Ray Absorption Spectroscopy. *J. Phys. Chem. C* **2014**, *118* (4), 1856–1863.

(41) Potze, R. H.; Sawatzky, G. A.; Abbate, M. Possibility for an Intermediate-Spin Ground State in the Charge-Transfer Material $SrCoO_3$. *Phys. Rev. B* **1995**, *51* (17), 11501–11506.

(42) Ghiringhelli, L. M.; Vybiral, J.; Levchenko, S. V.; Draxl, C.; Scheffler, M. Big Data of Materials Science: Critical Role of the Descriptor. *Phys. Rev. Lett.* **2015**, *114* (10), 1–5.

(43) Oh, N. K.; Seo, J.; Lee, S.; Kim, H. J.; Kim, U.; Lee, J.; Han, Y. K.; Park, H. Highly Efficient and Robust Noble-Metal Free Bifunctional Water Electrolysis Catalyst Achieved via Complementary Charge Transfer. *Nat. Commun.* **2021**, *12* (1), 1–12.

(44) Zhu, Y.; Zhou, W.; Yu, J.; Chen, Y.; Liu, M.; Shao, Z. Enhancing Electrocatalytic Activity of Perovskite Oxides by Tuning Cation Deficiency for Oxygen Reduction and Evolution Reactions. *Chem. Mater.* **2016**, *28* (6), 1691–1697.

III. DFT Simulation for the Interface Carbon Diffusion.

This chapter includes the materials of:

Dissolving Diamond: Kinetics of the Dissolution of (100) and (110) Single Crystals in Nickel and Cobalt Films

Yunqing Li, **Yongchul Kim**, Pavel V. Bakharev, Won Kyung Seong, Chohee Hyun, Dulce C. Camacho-Mojica, Liyuan Zhang, Benjamin V. Cunning, Tae Joo Shin, Geunsik Lee*, and Rodney S. Ruoff*
Chem. Mater. 2022, **34**, 2599 – 2611. Copyright © 2022, American Chemical Society.

3.1 Introduction

Diamond has the highest atomic concentration and thermal conductivity, the highest shear modulus and shear strength, the highest tensile strength, and the highest hardness of all known materials.[1−5] These remarkable properties open up a wide range of potential applications for bulk diamond and diamond thin films.[2,6−8] However, to fully exploit the potential of diamond-based structures, it is essential to develop efficient methods for diamond patterning and surface morphology modification. Conventional patterning methods such as hard mask-[9] or lithography-based[10] reactive ion etching (RIE), molding[11] and laser patterning[12] are time consuming and can cause significant damage to diamonds.[13-17] Alternatively, it has recently been demonstrated that water vapor can continuously dissolve carbon into thin nickel films in single-crystal diamond with surface orientations of (100) and (110).[18,19] However, to date, there has not been any comprehensive study on the interaction between diamond and metal at the metal−diamond interface, the dissolution of C, and its diffusion in the metal film, as well as the water-induced reaction at the open metal surface.

The current work is a comprehensive experimental and theoretical study on the kinetics of the dissolution of a singlecrystal diamond with the (100) and (110) surface planes into Ni and Co films. We conducted DFT modeling for the reactions at the metal open surface and at the metal/diamond interface to thoroughly describe the diamond dissolution process.

3.2 Methods

DFT calculations were done with the Vienna ab initio simulation package (VASP).[20] The PBE type exchange–correlation functional[21] was used as it predicts FCC Ni and Co lattice constants (Ni 3.513 Å and Co 3.514 Å) within ～0.2% error when compared with experiment,[22,23] and the bulk modulus values (Ni 188 GPa, Co 213 GPa) were also in good agreement with the experimental values (Ni 186 GPa, Co 196 GPa).[23,24] Spinpolarization was considered in whole simulations with a 400 eV cutoff energy. In all slab structures, the vacuum size was greater than 15 Å. The structure optimizations were done until all the residual atomic forces became less than 0.01 eV/Å. To calculate the activation energies and to probe the mechanism of carbon diffusion and role of H2O and thus the elimination of C at the free metal surface, the climbing image nudged elastic band (CI-NEB)[25] method was used. The temperature effect in the CI-NEB calculations was considered by choosing the reported high temperature lattice constants, corresponding to 3.58 Å for Ni (T = 1256 K) or 3.63 Å for Co (T = 1394 K) and 3.57 Å for diamond (T = 1273 K).[22,26,27] The unit cell size for the metal–diamond interfaces was adjusted to the lattice parameters of Ni or Co with a lattice mismatch smaller than 1.5%. In Table 3.1, the supercell size, surface Miller indices, slab thickness, interlayer distance, and K-point sampling of the simulated structures are given. The pressure effect or PV contribution in enthalpy is negligible for the interface or estimated as small as RT ～ 10.6 kJ/mol using T = 1273 K for gas production reactions at the surface.

Table 3.1 The detailed parameters of the simulation model. Copyright © 2022, American Chemical Society.

Reaction	**Supercell size**	**Slab layer number**	**Interlayer distance (Å)**	**K-point sampling**
Ni(001) – H_2O	Ni: 2 x 2	Ni: 4		3 x 3 x 1
Ni(001) – D(001)	Ni: 2 x 2 D: 2 x 2	Ni: 4 D: 4	1.489	3 x 3 x 1
Bulk FCC Ni C diffusion (O-T site)	2 x 2 x 2			8 x 8 x 8
Co(001) – H_2O	Co: 2 x 2	Co: 4		3 x 3 x 1
Co(001) – D(001)	Co: 2 x 2 D: 2 x 2	Co: 4 D: 4	1.480	3 x 3 x 1
Bulk FCC Co C diffusion (O-T site)	2 x 2 x 2			8 x 8 x 8
Ni(110) – H_2O	Ni: 3 x 3	Ni: 4		2 x 2 x 1
Ni(110) – D(110)	Ni: 3 x 3 D: 3 x 3	Ni: 4 D: 4	1.379	2 x 2 x 1
Co(110) – H_2O	Co: 3 x 3	Co: 4		2 x 2 x 1
Co(110) – D(110)	Co: 3 x 3 D: 3 x 3	Co: 4 D: 4	1.428	2 x 2 x 1

3.3 Results and Discussion

3.3.1 Experimental Findings

(Note: In order to avoid misunderstanding of experimental results, the description followed the original text as much as possible.)

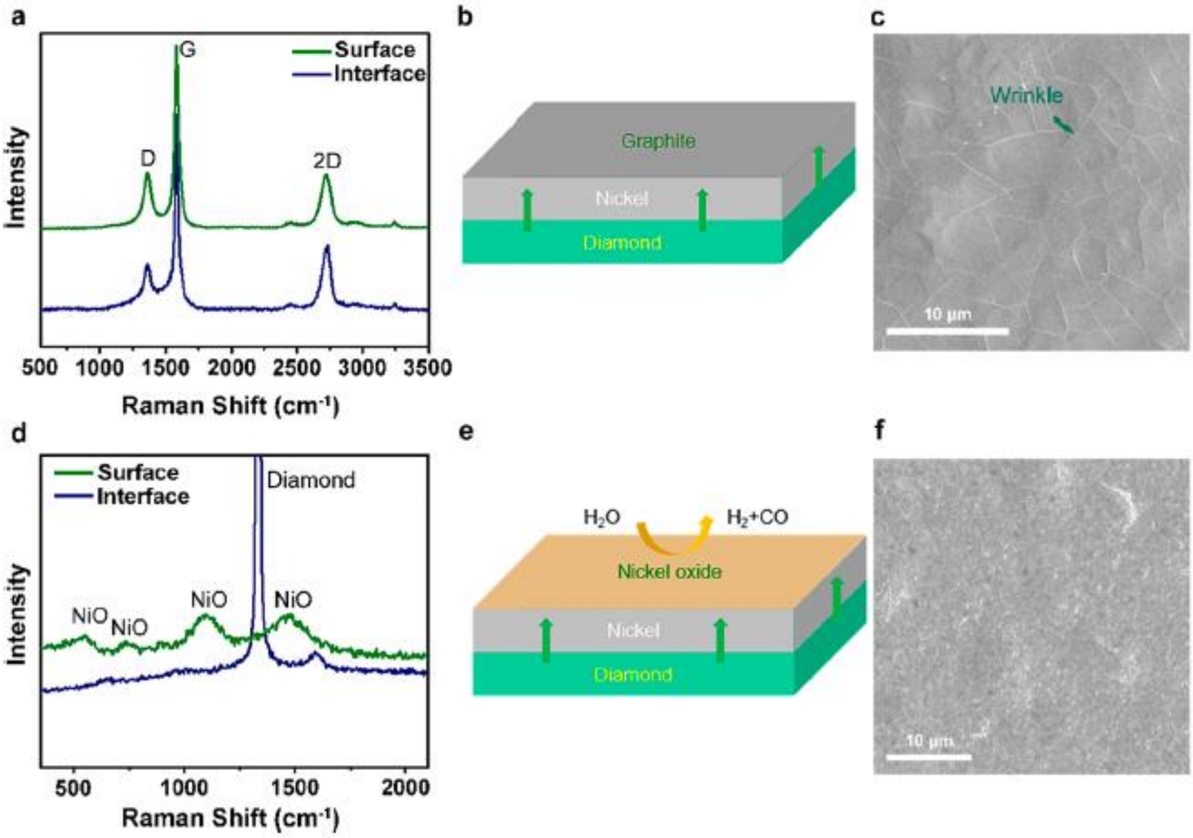

Figure 3.1 (a) Raman spectra after experiment without water vapor that were measured at the open metal surface (upper spectrum) and at the diamond surface after removal of the Ni film (lower spectrum). (b) Schematic of the Ni−diamond system; the green arrows show the diffusion direction of the C atoms. (c) SEM image of the graphite film formed on the open Ni surface. (d) Raman spectra obtained after the experiment with water vapor present in the quartz chamber, which were measured at the open metal surface (upper spectrum) and at the diamond surface after the removal of the Ni_xO_y/Ni film (lower spectrum). (e) Schematic of C diffusion through a Ni film and oxidation of C atoms at the open Ni surface. (f) SEM image of the nickel (oxide) surface. Copyright © 2022, American Chemical Society.

Experimental group sputter-deposited 500 nm-thick Ni and Co films onto the single-crystal diamond plates of (100) and (110) surface orientation. The Raman spectra of these graphite films (D ∼ 1350 cm−1, G ∼ 2580 cm−1, and 2D ∼ 2700 cm−1 band)[28] are shown in Figure 3.1a. Raman characterization suggests that some of the C atoms at the Ni/D(100) interface “dissolved” and diffused into and through the Ni film at 1009 ± 1 °C. The configuration of the Ni−diamond sample and the direction of C diffusion are schematically shown in Figure 3.1b. The scanning electron microscopy

(SEM) image (Figure 3.1c) shows wrinkles[29] in the graphite film formed on the metal surface. After the Ni film was removed, wrinkles were also observed in the graphite film on the diamond surface, which had been formed at the Ni/D(100) interface.

In contrast, with water vapor present (see details in the Methods section of the original paper) in the quartz tube reaction chamber during the heat treatment at 1009 ± 1 °C for 30 min under a 1000 sccm flow of Ar(g) at 760 ± 1 Torr total pressure, an oxide layer was formed at the open metal surface and the continuous dissolution of diamond at the metal/diamond interface was observed, as shown in Figure 3.1d. Evidently, H_2O reacts with the Ni film, and the dissolved C is essentially removed "by" the water vapor, as reported by Nagai et al.[18] The concentration gradient of C in the Ni or Co film established by the continuous removal of C at the surface drives the continuous dissolution of the diamond at the M/D(100) interface, as shown schematically in Figure 3.1e. Raman (Figure 3.1d) and SEM (Figure 3.1f) analyses show that no graphite film was formed on the open metal surface, and this is because the C could be continuously removed by the water vapor. After the Ni film was removed, no graphite film was observed at the Ni/D(100) interface. Owing to the driving force of the C concentration gradient which is formed and maintained by continuous reaction between water vapor and C at the open metal surface, C atoms continuously diffuse from the interface to the open metal surface; this continuous "outflow" of C prevents the formation of graphene/graphite at the metal/diamond interface. The Ni/D(110) results are similar to the results on Ni/D(100) described above.

Figure 3.2a-d shows Arrhenius plots for the rates of dissolution of D(100) and D(110) in 500 nm-thick Ni and Co films, measured for different water vapor partial pressures (i.e., at different temperatures of the water bubbler unit) at the sample temperature range of 875 to 1009 ± 1 °C. Based on the fact that for each D/Metal system two different slopes (activation enthalpies) were obtained for the Arrhenius plots at different water bubbler temperatures, we may suggest two regimes (referred to as regime I and regime II for relatively low (≤25 °C) and high (≥43 °C) water bubbler temperatures, respectively) to describe the water induced diamond dissolution process. The Arrhenius plots in Figure 3.2a,b have essentially identical slopes for bath temperatures of 0 and 25 °C even though the concentration of water vapor is about 4× higher at 25 °C than at 0 °C (mole fraction in argon gas: 0.0064 for 0 °C and 0.0029 for 25 °C). For water bubbler temperatures of 43 and 63 °C, we discovered for the 500 nm-thick Ni film on the D(100) plate that the dissolution rates and the slopes of the Arrhenius plots are essentially identical. The values of the activation enthalpy $\Delta H^{\ddagger}$, and the prefactor, A, measured for the diamond dissolution rates, k ($\ln k = -\Delta H^{\ddagger}/\mathrm{RT} + \ln A$), in regimes I and II are given in Table 3.2 for D(100) and D(110). We note that the experimental activation energies of C diffusion in Ni and Co reported in the literature are 137 kJ/mol (for the temperature range 873−1673 K) and 154 kJ/mol (for the temperature range 976−1673 K), respectively.[30,31] These reported values are substantially lower than the $\Delta H^{\ddagger}$ values obtained for both regimes. This suggests that diffusion of C through the Ni or Co films is not the rate-limiting step in either regime.

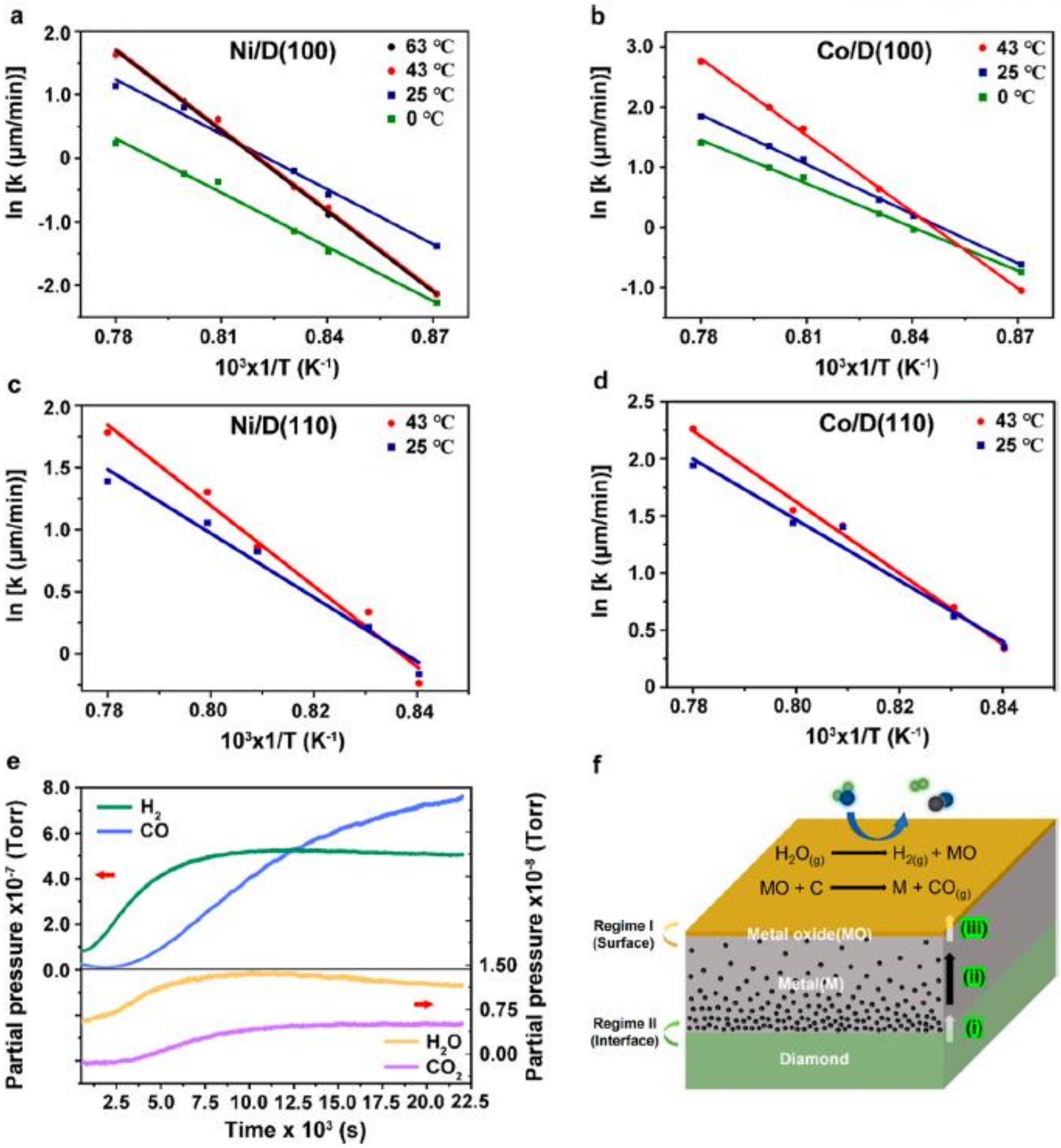

Figure 3.2 (a, b) Arrhenius plots of the dissolution rates of single-crystal diamonds with (100) surfaces coated with a (a) 500 nm-thick Ni film and (b) 500 nm-thick Co film, at different water bubbler temperatures. (c, d) Arrhenius plots of the dissolution rates of single-crystal diamond with (110) surfaces coated with a (c) 500 nm-thick Ni film and (d) 500 nm-thick Co film, at different water bubbler temperatures. (e) Real-time residual gas analyzer (RGA) analysis of water vapor−Ni−diamond reaction products. (f) Schematic of diamond dissolution with water vapor present: the surface reaction [regime I when this is rate-limiting, step (iii)] and the metal diamond interface where diamond dissolves into the metal through breaking of C−C bonds at the M−D interface [regime II when this is rate-limiting, step (i)]. Step (ii) represents diffusion of C atoms through the Ni film-this is never rate-limiting for our study. Copyright © 2022, American Chemical Society.

Table 3.2 $\Delta H^{\ddagger}$ and Prefactor *A* Values, from a Study of the Dissolution of D(100) and D(110) Coated with a 500 nm-Thick Ni or Co Film. Copyright © 2022, American Chemical Society.

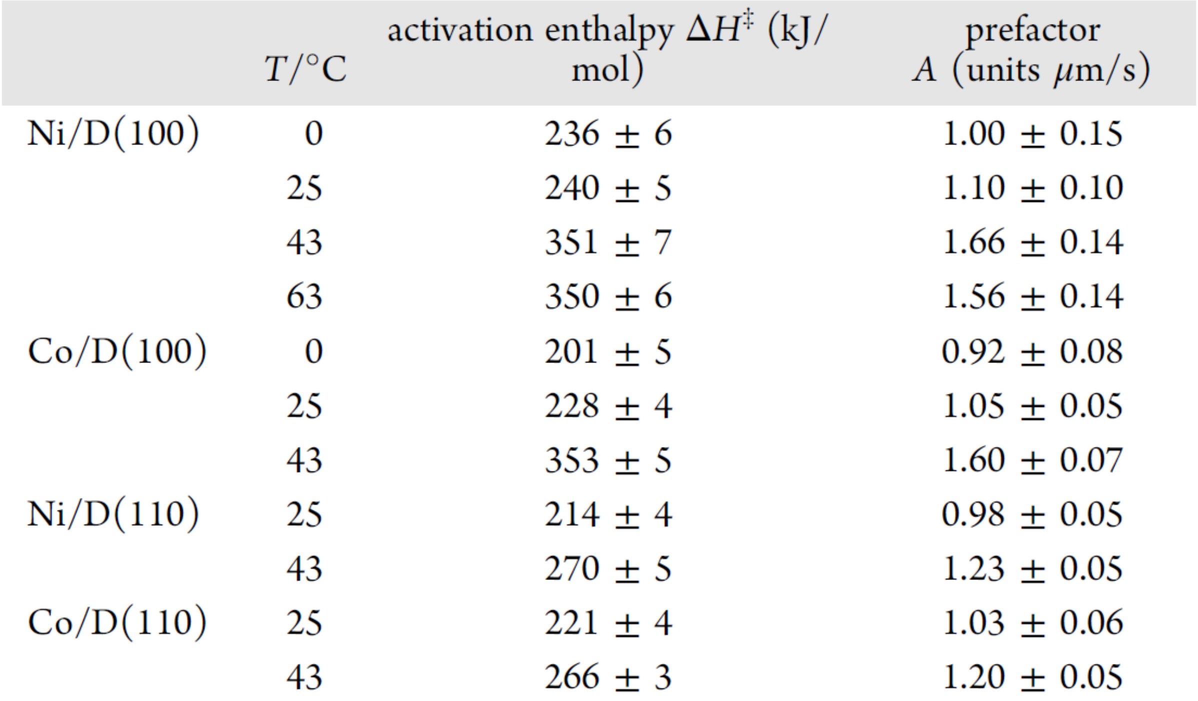

	T/°C	activation enthalpy $\Delta H^{\ddagger}$ (kJ/mol)	prefactor A (units μm/s)
Ni/D(100)	0	236 ± 6	1.00 ± 0.15
	25	240 ± 5	1.10 ± 0.10
	43	351 ± 7	1.66 ± 0.14
	63	350 ± 6	1.56 ± 0.14
Co/D(100)	0	201 ± 5	0.92 ± 0.08
	25	228 ± 4	1.05 ± 0.05
	43	353 ± 5	1.60 ± 0.07
Ni/D(110)	25	214 ± 4	0.98 ± 0.05
	43	270 ± 5	1.23 ± 0.05
Co/D(110)	25	221 ± 4	1.03 ± 0.06
	43	266 ± 3	1.20 ± 0.05

Figure 3.2e shows the realtime partial pressure response curves of H_2, CO, H_2O, and CO_2 gases/vapors that leaked through the metering valve from the CVD reaction chamber into the high vacuum gas analyzer system. The process of the dissolution of diamond in Ni or Co films in the presence of water vapor involves three primary steps: (i) C—C bond breaking followed by the diffusion of C atoms into Ni or Co films at the metal/diamond interface, (ii) C diffusion through the 500 nm-thick metal film, and (iii) reaction of C atoms with a thin layer of metal oxide on the metal surface to form CO(g), as schematically shown in Figure 3.2f.

3.3.2 Theoretical Modeling of Reaction Pathways and Potential Energy Barriers

We have done a variety Density functional theory (DFT) calculations related to these metal thin films deposited on diamond and heated in the presence or absence of water vapor. The potential energy barriers of (i) the oxidation reactions on open metal surfaces; (ii) carbon "dissolves" into the metal-diamond interfaces were calculated at ~1273K and is shown in the Figure3.3. We used $Fm\bar{3}m$ Ni(100) [Ni(110)] or Co(100) [Co(110)] configurations on the D(100)[D(110)] surfaces in our modeling because the experiments suggested that the films are either completely or mostly epitaxial to the single-crystal diamond substrates.

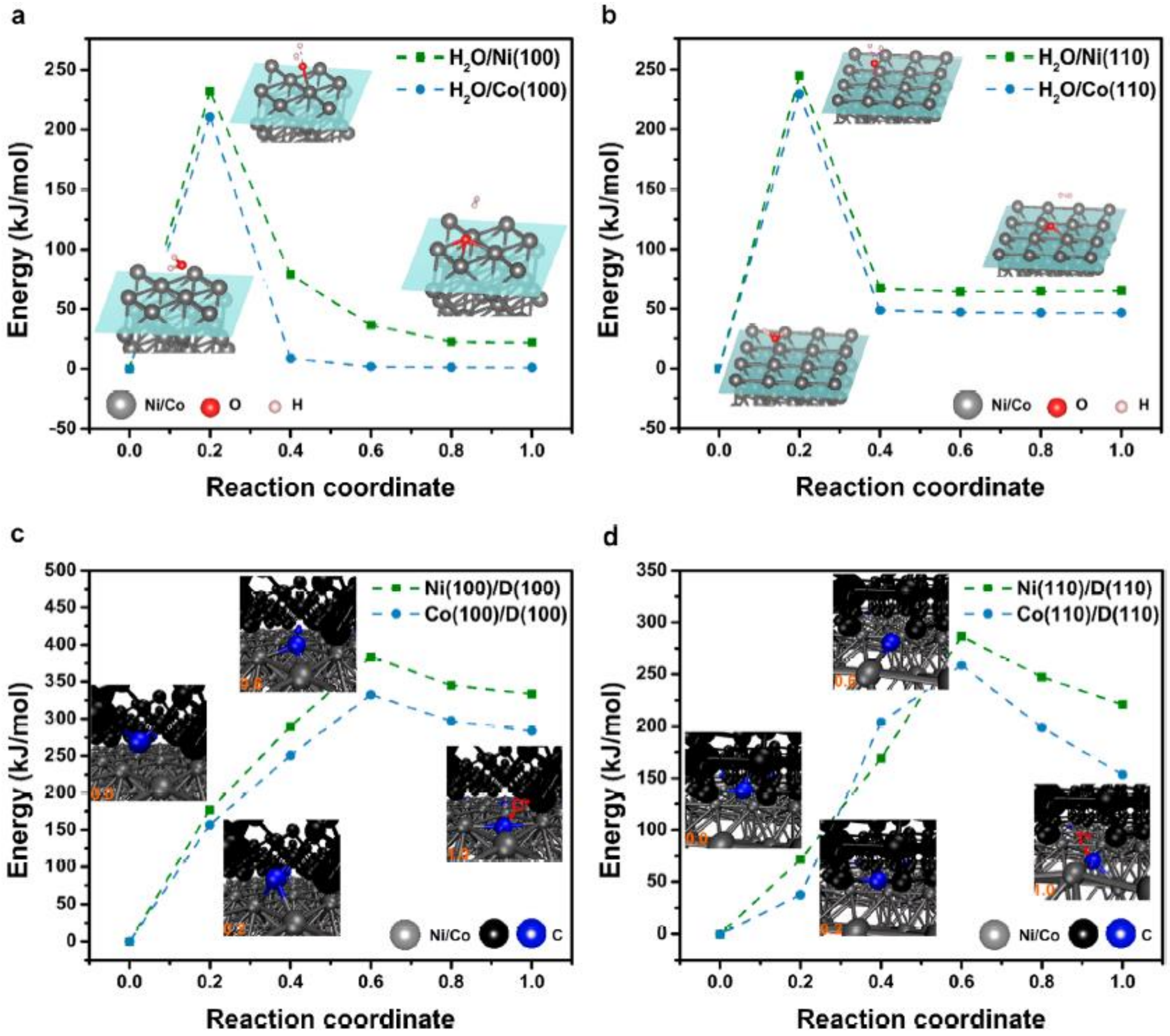

Figure 3.3 (a,b) Potential energy curves calculated for (a) H_2O molecule reacting with Ni(100) (green) or Co(100) (blue) and (b) for C−C bond breaking at the Ni(100)/D(100) (green) or Co(100)/D(100) (blue) interfaces. The corresponding atomic structures of the initial, intermediate, and final configurations are shown as insets. (c,d) Potential energy curves calculated for a C atom diffusing from (c) Ni(100)/D(100) interface (green) through the octahedral site (O*) or (d) Co(110)/D(110) interface (blue) through the tetrahedral site (T*). The corresponding atomic structures of the initial, intermediate, and final configurations are shown as insets. Copyright © 2022, American Chemical Society.

Figure 3.3a shows the calculated potential energy curves for surface reactions of H_2O molecules on Ni(100) and Co(100) surfaces (Figure 3.4). A H_2O molecule adsorbs with binding energies of -0.745 eV on Ni(100) and -0.270 eV on Co(100), and then dissociates into hydrogen molecule and a chemisorbed oxygen atom. The calculated $\Delta H^{\ddagger}$ for this dissociation is 232 kJ/mol on the Ni(100) surface and 211 kJ/mol on the Co(100) surface. For the comparison, the experimental values with water bubbler temperatures in parentheses on D(100) substrates are Ni: 236 ± 6 kJ/mol (0 °C), 240 ± 5 kJ/mol (25 °C) and Co: 201 ± 5 kJ/mol (0 °C), 228 ± 4 kJ/mol (25 °C), for regime I. The C atoms diffusing through the metal layer react with surface -Ni-O species to form -Ni-C-O and decompose to release CO into the gas phase. Potential-energy curves describing the formation of -Ni-C-O configurations on the Ni(100) surface and their decomposition to release CO into the gas phase are shown in Figure 3.5. The same simulation of the formation of -Co-C-O and its decomposition to release CO into the gas phase is shown in Figure 3.6. For both, the energy barrier is primarily lower than the formation barrier of -Ni-O (232 kJ/mol) and -Co-O species (211 kJ/mol) at each fcc-M(100) surface. The same simulation was conducted for the Ni(110) and Co(110) surfaces (see details of the DFT modeling in Figure 3.7), as shown in Figure 3.3b. A H_2O molecule absorbs with binding energies of -0.405 eV on the Ni(110) surface and -0.391 eV on the Co(110) surface. The calculated $\Delta H^{\ddagger}$for its dissociation is 245 kJ/mol on the Ni(110) surface and 230 kJ/mol on the Co(110) surface. Our experimental values (water bubbler temperatures in parentheses) on D(110) substrates are follows: Ni: 214 ± 4 kJ/mol (25 °C) and Co: 221 ± 4 kJ/mol (25 °C) for regime I. The energy barrier values describing the formation of -M-O species, the formation of -M-C-O states on the M(110) surface and the decomposition to release CO into the gas phase are provided in Figure. 3.8. According to our DFT simulations, the activation energy barriers for the formation of −Ni−O species on Ni(110) and −Co−O species on Co(110) in regime I are 245 and 230 kJ/mol, respectively. These theoretical values are comparable with the experimental values. The energy barriers are summarized in Table 3.3 at each step for the M(100) and M(110) cases.

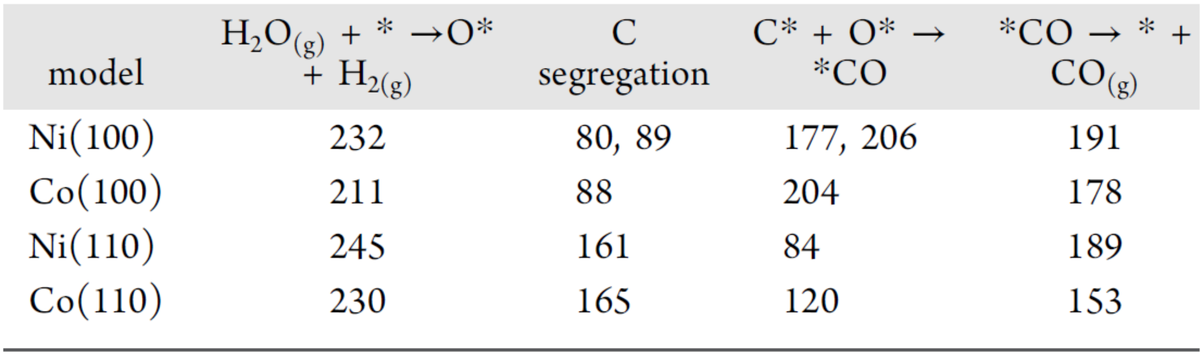

model	$H_2O_{(g)} + * \rightarrow O^* + H_{2(g)}$	C segregation	$C^* + O^* \rightarrow {}^*CO$	${}^*CO \rightarrow * + CO_{(g)}$
Ni(100)	232	80, 89	177, 206	191
Co(100)	211	88	204	178
Ni(110)	245	161	84	189
Co(110)	230	165	120	153

Table 3.3 Energy Barrier Values (kJ/mol) Describing the Formation of −Ni−C−O or −Co−C−O States on Ni/Co(100) and Ni/Co(110) Surfaces and the Decomposition to Release CO into the Gas Phase. Copyright © 2022, American Chemical Society.

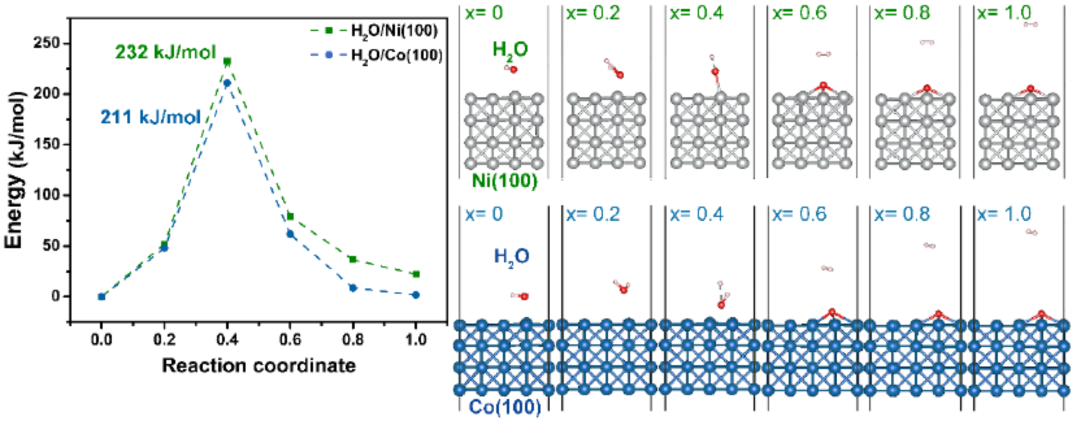

Figure 3.4 (left) Potential energy curves for an H_2O molecule reacting with the Ni(100) or Co(100) surfaces; (right) atomic structures of the initial physisorbed molecule (x= 0.0), the transition state (x= 0.4) and other intermediate configurations. Copyright © 2022, American Chemical Society.

Binding energies (-2.90 eV/C atoms for Ni(100)-D(100) and -3.27 eV/C atoms for Co(100)-D(100)) with respect to the M-D(100) interface metal surface stabilize the sp3-bonded C atoms on the D(100) surface located at bridge positions with respect to the atomic arrangement of Ni(100) or Co(100). The increases in energy up to the transition state are caused by sequential two steps: (i) a lateral movement that breaks one C—C bond, (ii) migration perpendicular to the surface with breaking of another C—C bond. These two C atoms then move to the octahedral interfacial sites in the fcc metal structure. As the carbon movement results, the potential energy curves of carbon atom diffusion at the Ni(100) or Co(100)/D(100) interface through the octahedral sites are shown in Figure 3.3c. In DFT simulations, the $\Delta H^{\ddagger}$ for this process was calculated to be 384 kJ/mol for the Ni(100)—D(100) interface and 332 kJ/mol for the Co(100)—D(100) interface. These theoretical activation barriers can be compared with the experimental values of 351 ± 7 kJ/mol (Ni/D(100)) and 353 ± 5 kJ/mol (Co/D(100)) (water bubbler temperature 43 °C (regime II)) discussed above.

In case of the M—D(110) interface diamond dissolution process, the permeation of C through the metal film starts with the dissociation of the C—C bonds at the metal—diamond interface. Interestingly, the C—C bonds at the M—D(110) interface preferentially release C atoms into the half-tetrahedral interfacial sites of the fcc metal structures instead of the octahedral sites (Figure 3.9). To show the activation barrier, the potential energy curves for carbon atom diffusion at the Ni(110) or Co(110)/D(110) interface are shown in Figure 3.3d. In the DFT calculations, the $\Delta H^{\ddagger}$ for this process was given by the 287 kJ/mol for the Ni(110)—D(110) interface and 259 kJ/ mol for the Co(110)—D(110) interface. These values can be compared with the respective experimental values of 270 ± 5 kJ/mol (Ni/D(110)) and 266 ± 3 kJ/mol (Co/D(110)) (water bubbler temperature 43 °C (regime II)) discussed above.

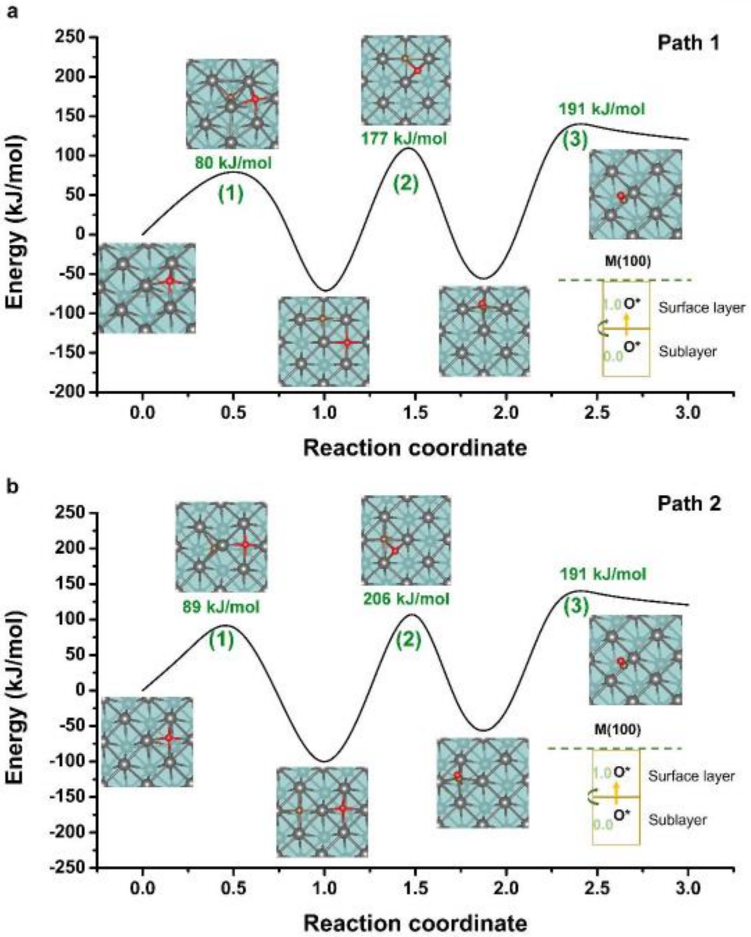

Figure 3.5 Potential energy curve for the surface reaction on Ni(100). **(a)** Potential energy curve for C atom migration from an octahedral (O*) site at the subsurface to an O* site at the surface, as shown in the inserted schematic image, which shows the reaction process from x= 0.0 to 1.0 (1). The O atom migrates from the original O* site to the O* site that the C atom had occupied yielding formation of -Ni-C-O (2), followed by release of one CO into the atmosphere (3). **(b)** Potential energy curve for C atom migration from an O* site at the subsurface to an O* site at the surface, as shown in the inserted schematic diagram, which shows the reaction process from x= 0.0 to 1.0 (1). The O atom migrates from the original O* site to an O* site that the C atom had occupied forming -Ni-C-O (2), followed by release of one CO into the atmosphere (3). Note that there are two possible paths for the migration of the O atom at the metal surface because there are two inequivalent half-octahedral sites that the C atom occupied relative to the position of the O atom at the surface. We calculated the two paths and provide the potential energy curve for both. The energy barriers at each step for these two paths are lower than the energy barrier of the surface reaction between a Ni atom and a H_2O molecule. Copyright © 2022, American Chemical Society.

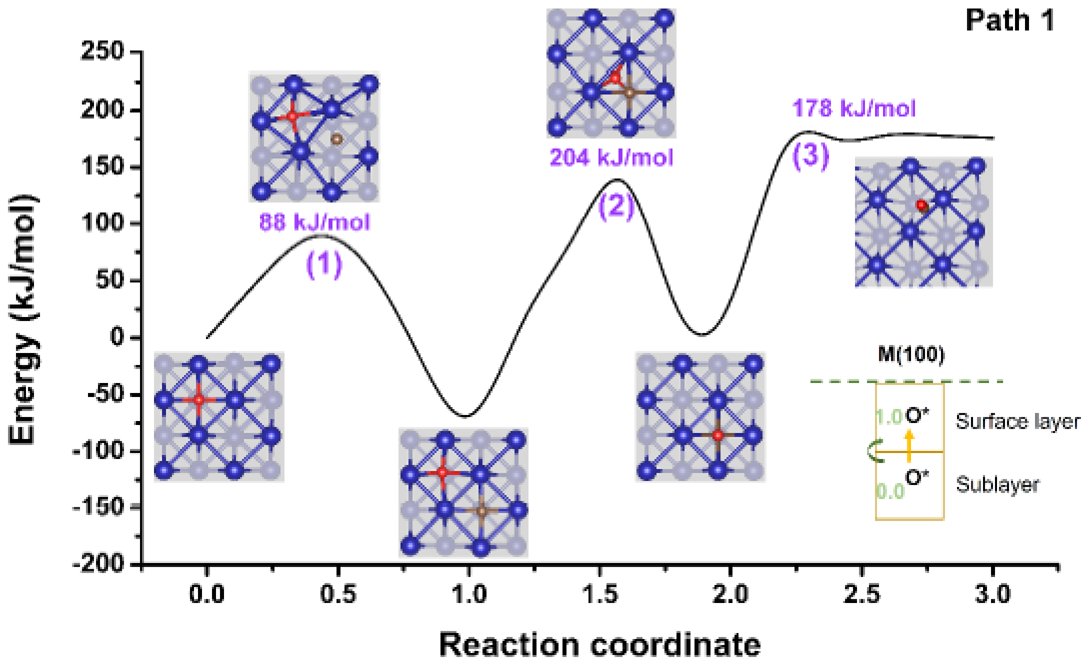

Figure 3.6 Potential energy curve for the surface reaction on Co(100). Potential energy curve for one C atom migration from an octahedral site (O*) at the subsurface to an O* site at the surface, as shown in the inserted schematic, which shows the reaction process from x= 0.0 to 1.0 (1). The oxygen atom migrates from the original O* site to the O* site that the C atom had occupied and forms the -Co-C-O state (2), and the -Co-C-O state decomposes and releases a CO(g) molecule into the atmosphere (3). The path calculated is the same as that calculated in **Figure 3.5a**, which has a lower energy barrier in steps (1) and (2) compared with the energy barrier for steps (1) and (2) in **Figure 3.5b**. The energy barriers at each step for this path are lower than the energy barrier of the surface reaction between a Co atom and a H_2O molecule. Copyright © 2022, American Chemical Society.

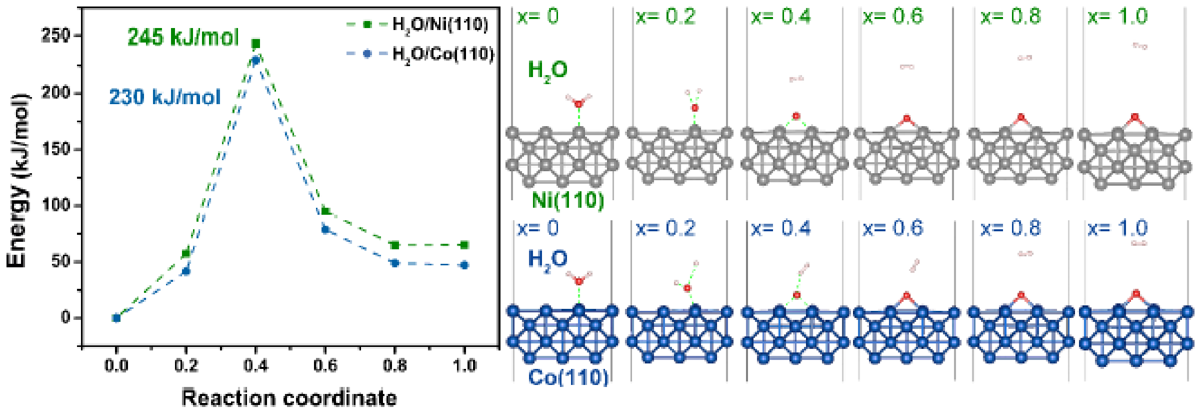

Figure 3.7 (left) Potential energy curves for a H_2O molecule reacting with the Ni(110) or Co(110) surface; (right) atomic structures of the initial physisorbed (x= 0.0) state, the transition state (x= 0.4) and other intermediate configurations. Copyright © 2022, American Chemical Society.

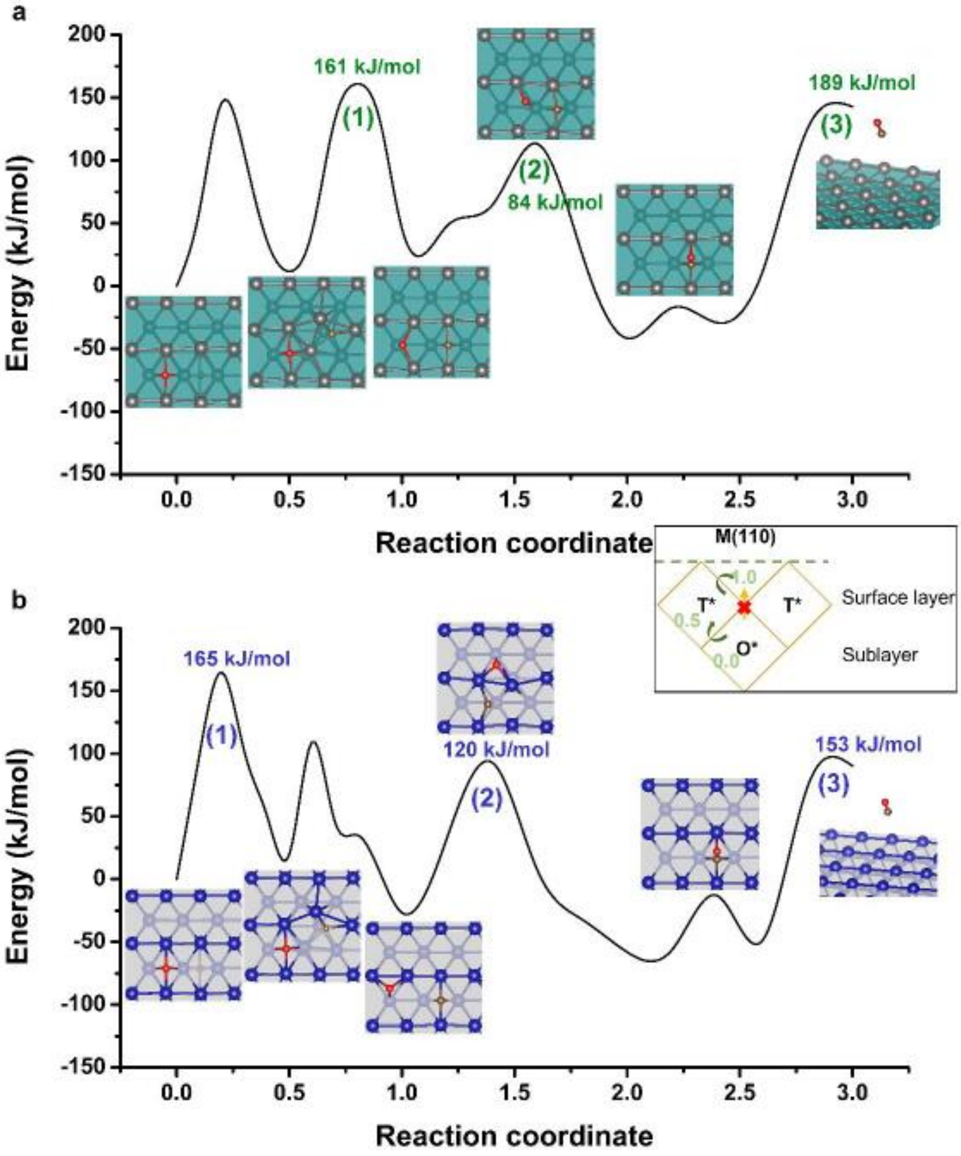

Figure 3.8 Potential energy curve for the surface reaction on (a) Ni(110) and (b) Co(110). One C atom jumps from an octahedral (O*) site at the subsurface to a tetrahedral (T*) site, then to the surface, as shown in the inserted schematic; from x= 0.0 to 1.0 (1), the O atom migrates from the original O* site to the T* site that the C atom occupied and forms -M-C-O (2), and the -M-C-O then releases a CO molecule into the atmosphere (3). Thus: From x= 0.0 to 1.0 the indicated C atom moves to the surface, from x= 1.0 to 2.0 a surface O atom and that same surface C atom migrate and react, and from x= 2.0 to 3.0 CO desorbs. The appearance of a C atom on the M(110) surface thus occurs in two steps, as shown in the inserted schematic: from x= 0.0 to 0.5, a C atom in the sublayer moves to a T* site just below the open surface, and from x= 0.5 to 1.0, this C atom moves from the T* site to the open surface. For Ni(110), this diffusion from subsurface to the surface has the highest energy barrier (161 kJ/mol) when the C atom migrates to the open surface. For Co(110) the highest energy barrier (165 kJ/mol) is for the C atom passing through the T* site. Copyright © 2022, American Chemical Society.

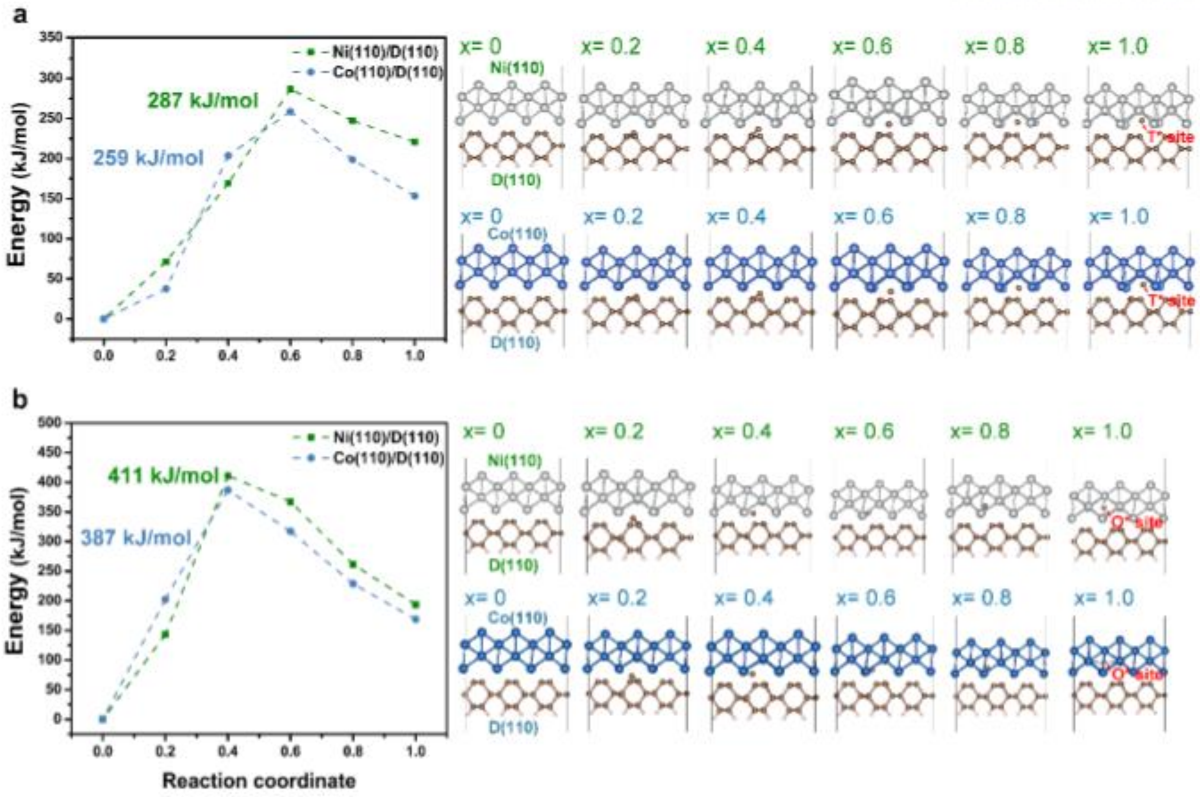

Figure 3.9 (left) Potential energy curves for C atom diffusion at the Ni(110)/D(110) (green curve) and Co(110)/D(110) (blue curve) interfaces through the (a) *tetrahedral* and (b) *octahedral* interfacial sites; (right) atomic structures of the initial (x= 0.0), intermediate (x= 0.2, 0.4, 0.6, and 0.8), and final (x= 1.0) configurations. Copyright © 2022 American Chemical Society.

3.3.3 Surface Exchange Mechanism

The calculated activation barriers for carbon diffusion in bulk Ni (153 kJ/mol) or Co (175 kJ/mol) (Figure 3.10) are much lower than the rate-limiting activation enthalpy of the surface (regime I) and the interface (regime II) processes; these calculated values are in good agreement with the reported experimental values of 137 kJ/mol (873−1673 K) for Ni and 154 kJ/mol (976−1673 K) for Co.[30,31] Since the metal bulk diffusion barrier is smaller than the enthalpy variation observed in the experiment, the carbon diffusion process inside the Ni or Co metal does not determine the reaction rate. Although the FCC bulk metal carbon diffusion barrier is small, there is one problem. As shown in Figure 3.11, the reverse reaction barrier of M(100)/D(100) interface carbon dissolution is less than 60 kJ/mol.

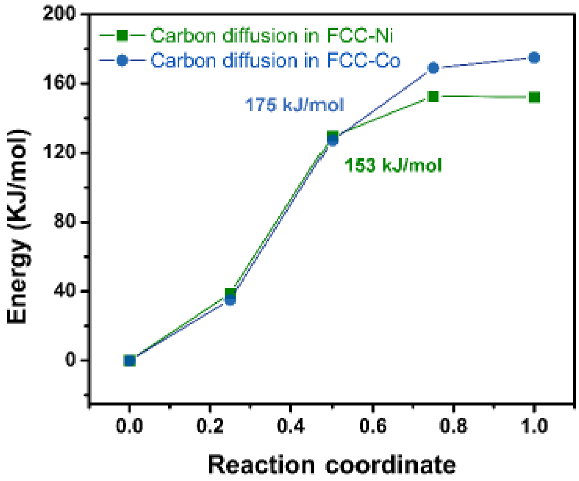

Figure 3.10 Potential energy curves of carbon diffusion barriers in fcc-Ni and fcc-Co. The C atom diffuses from an octahedral site to a tetrahedral site, then back to the octahedral site (O* → T* → O*). We show the C atom diffusion energy barrier from the O* site to T* site only, due to symmetry. Copyright © 2022 American Chemical Society.

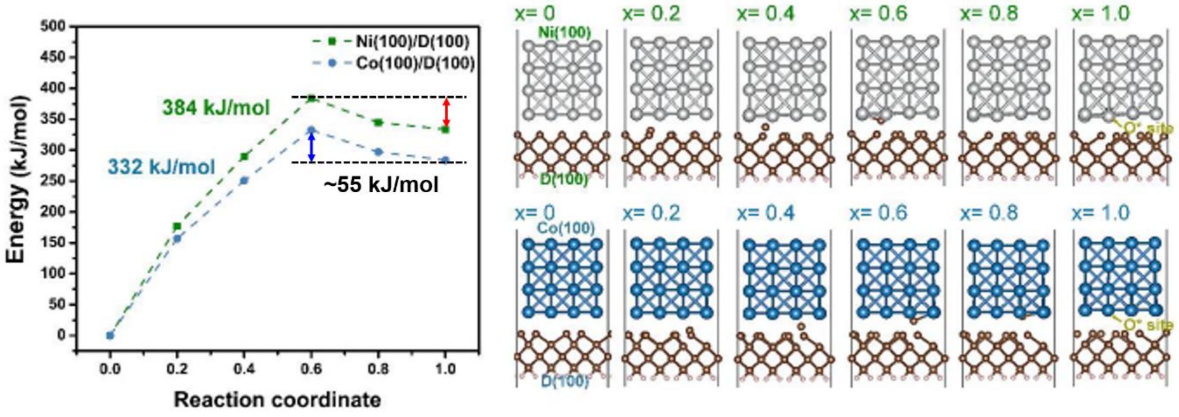

Figure 3.11 (left) Potential energy curves for C atom diffusion at the Ni(100)/D(100) (green curve) and Co(100)/D(100) (blue curve) interfaces; (right) atomic structures of the initial (x= 0.0), intermediate, and final (x= 1.0) configurations. Copyright © 2022 American Chemical Society.

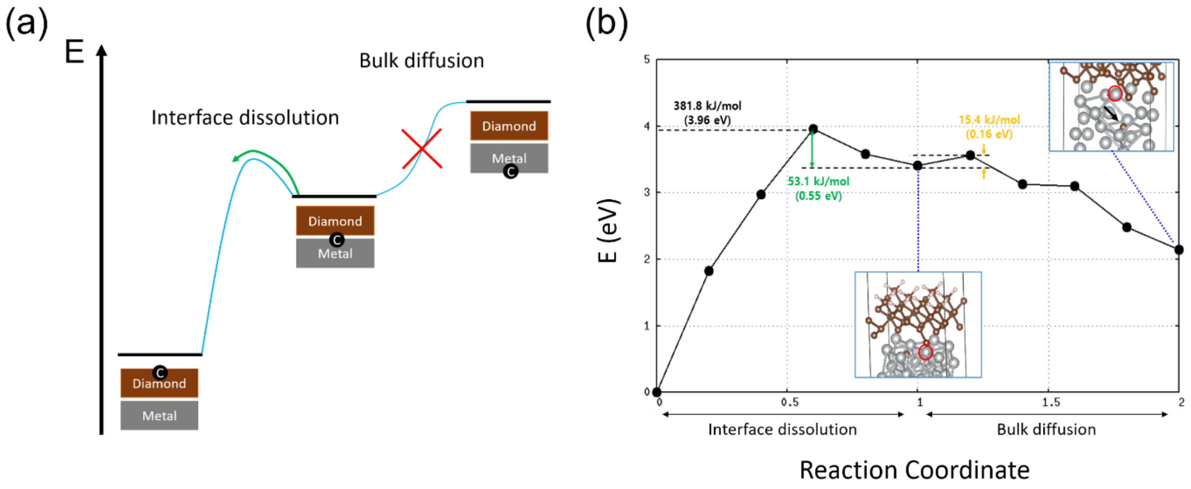

Figure 3.12 (a) Schematic comparison of interface dissolution and bulk FCC metal carbon diffusion. Due to the higher activation barrier of bulk diffusion, backward reaction may occur in this scheme. (b) Actual calculated activation barrier (T = 1386 K) of the process which is described in (a). Red circle indicates the surface Ni atom that move onto the carbon vacancy site in diamond. The first bulk carbon diffusion shows very low activation barrier (15.4 kJ/mol) compared to the reverse reaction barrier of interface carbon dissolution.

If the activation energy of the reverse interface dissolution reaction is smaller than that of bulk diffusion, it indicates that it is natural for carbon to return to the diamond surface as described in Figure 3.12a. However, carbon diffusion actually occurs as observed in experiment, implying that the activation barrier for the first carbon diffusion may not be very large. In actual DFT simulation, the activation barrier of the first carbon diffusion was small (E_a = 15.4 kJ/mol) in Ni(001)/D(001) interface system (Figure 3.12b). In Figure 3.10, the carbon diffusion barrier in Ni is 153 kJ/mol, but at the Ni(001)/D(001) interface, the barrier is significantly lowered with the assist of diamond vacancy site of diffused carbon. As the Ni atom, indicated by the red circle in Figure 3.12b, moves to the diamond vacancy site, it creates space and the carbon facilitates bulk diffusion. Figure 3.13 shows the location of the Ni atom after it migrates to the vacancy site. In summary, we found that the positions of diamond surface carbon and Ni are exchanged as a result, and surface exchange plays a key role in the carbon diffusion in metal-diamond interface system.

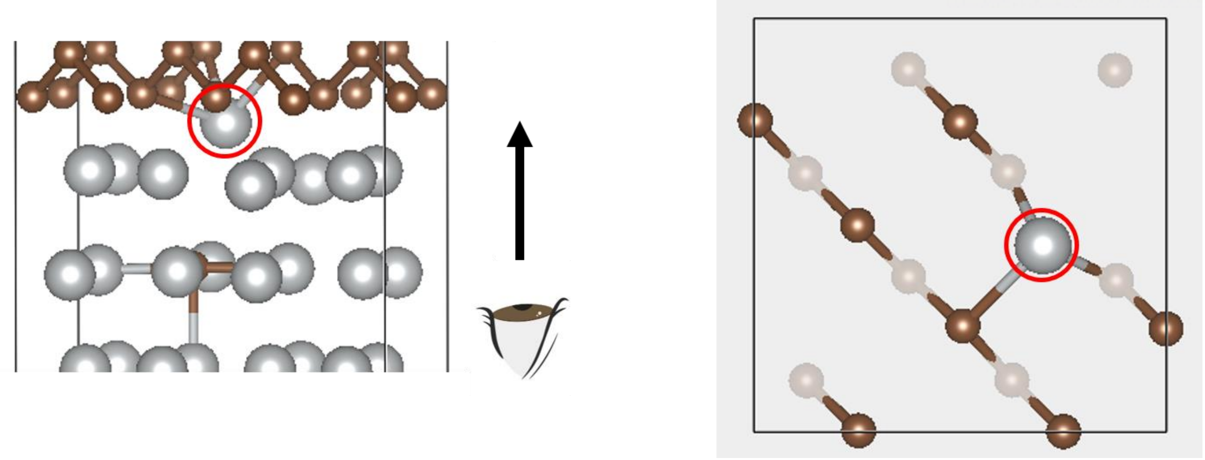

Figure 3.13 The location of transferred Ni at (left) the bird-eye view, and (right) bottom-up direction view.

3.4 Conclusion

This work is a comprehensive study of the kinetics of water vapor-induced dissolution of single crystal (100) and (110) diamond into nickel and cobalt films. The data and modeling inspire people in the industry to consider this method of removing diamonds as an alternative to polishing with mechanical abrasives. In addition, this study shed light on the veiled carbon diffusion process which is promoted through the interface exchange of carbon and metal atom at the metal-diamond interface. Knowing the kinetics and being able to model the rate of dissolution opens up new opportunities to "preshape" single crystal diamond in a way that can replace or enhance other methods such as RIE, molding and laser patterning to achieve microfabrication. It includes novel 3D structures such as quantum devices[32], MEMS[33], and power devices[34] and has low cost, high efficiency, and high controllability without “plasma damage” caused by the RIE method.[35] This research also covers free surface and metal/diamond Diamond dissolution through rational control of thermochemical parameters at the interface.

3.5 References

(1) Aharonovich, I.; Greentree, A. D.; Prawer, S. Diamond photonics. *Nat. Photonics* **2011**, 5, 397−405.

(2) Wort, C. J. H.; Balmer, R. S. Diamond as an electronic material. *Mater. Today* **2008**, 11, 22−28.

(3) Pleskov, Y. V. Electrochemistry of diamond: A review. *Russ. J. Electrochem.* **2002**, 38, 1275−1291.

(4) Werner, M.; Locher, R. Growth and application of undoped and doped diamond films. *Rep. Prog. Phys.* **1998**, 61, 1665−1710.

(5) Jelezko, F.; Wrachtrup, J. Single defect centres in diamond: A review. *Phys. Status Solidi A* **2006**, 203, 3207−3225.

(6) Nebel, C. E.; Rezek, B.; Shin, D.; Uetsuka, H.; Yang, N. Diamond for bio-sensor applications. *J. Phys. D Appl. Phys*. **2007**, 40, 6443−6466.

(7) Balmer, R. S.; Brandon, J. R.; Clewes, S. L.; Dhillon, H. K.; Dodson, J. M.; Friel, I.; Inglis, P. N.; Madgwick, T. D.; Markham, M. L.; Mollart, T. P.; Perkins, N.; Scarsbrook, G. A.; Twitchen, D. J.; Whitehead, A. J.; Wilman, J. J.; Woollard, S. M. Chemical vapour deposition synthetic diamond: materials, technology and applications. *J. Phys.: Condens. Matter* **2009**, 21, 364221.

(8) Kianinia, M.; Aharonovich, I. Diamond photonics is scaling up. *Nat. Photonics* **2020**, 14, 599−600.

(9) Hicks, M. L.; Pakpour-Tabrizi, A. C.; Jackman, R. B. Diamond Etching Beyond 10 mu m with Near-Zero Micromasking. *Sci. Rep.* **2019**, 9, 15619.

(10) Castelletto, S.; Rosa, L.; Blackledge, J.; Al Abri, M. Z.; Boretti, A. Advances in diamond nanofabrication for ultrasensitive devices. *Microsyst. Nanoeng*. **2017**, 3, 17061.

(11) Yan, J.; Imoto, Y. Nanoscale surface patterning of diamond utilizing carbon diffusion reaction with a microstructured titanium mold. *CIRP Ann.- Manuf. Technol.* **2018**, 67, 181−184.

(12) Kononenko, T. V.; Kononenko, V. V.; Konov, V. I.; Pimenov, S. M.; Garnov, S. V.; Tishchenko, A. V.; Prokhorov, A. M.; Khomich, A. V. Formation of antireflective surface structures on diamond films by laser patterning. *Appl. Phys. A: Mater. Sci. Process.* **1999**, 68, 99−102.

(13) Hwang, D. S.; Saito, T.; Fujimori, N. New etching process for device fabrication using diamond. *Diam. Relat. Mater.* **2004**, 13, 2207−2210.

(14) Ando, Y.; Nishibayashi, Y.; Kobashi, K.; Hirao, T.; Oura, K. Smooth and high-rate reactive ion etching of diamond. *Diam. Relat. Mater.* **2002**, 11, 824−827.

(15) Kawabata, Y.; Taniguchi, J.; Miyamoto, I. XPS studies on damage evaluation of single-crystal diamond chips processed with ion beam etching and reactive ion beam assisted chemical etching. *Diam. Relat. Mater.* **2004**, 13, 93−98.

(16) Kato, Y.; Kawashima, H.; Makino, T.; Ogura, M.; Traore, A.; Ozawa, N.; Yamasaki, S. Estimation of Inductively Coupled Plasma Etching Damage of Boron-Doped Diamond Using X-Ray Photoelectron Spectroscopy. *Phys. Status Solidi A* **2017**, 214, 1700233.

(17) Kunuku, S.; Sankaran, K. J.; Tsai, C.-Y.; Chang, W.-H.; Tai, N.-H.; Leou, K.-C.; Lin, I.-N. Investigations on Diamond Nanostructuring of Different Morphologies by the Reactive-Ion Etching Process and Their Potential Applications. *ACS Appl. Mater. Interfaces* **2013**, 5, 7439−7449.

(18) Nagai, M.; Nakanishi, K.; Takahashi, H.; Kato, H.; Makino, T.; Yamasaki, S.; Matsumoto, T.; Inokuma, T.; Tokuda, N. Anisotropic diamond etching through thermochemical reaction between Ni and diamond in high-temperature water vapour. *Sci. Rep.* **2018**, 8, 6687.

(19) Nagai, M.; Nakamura, Y.; Yamada, T.; Tabakoya, T.; Matsumoto, T.; Inokuma, T.; Nebel, C. E.; Makino, T.; Yamasaki, S.; Tokuda, N. Formation of U-shaped diamond trenches with vertical {111} sidewalls by anisotropic etching of diamond (110) surfaces. *Diam. Relat. Mater.* **2020**, 103, 107713.

(20) Kresse, G.; Furthmu¨ller, J. Efficient iterative schemes for ab initio total-energy calculations using a plane-wave basis set. *Phys. Rev. B: Condens. Matter Mater. Phys.* **1996**, 54, 11169−11186.

(21) Perdew, J. P.; Burke, K.; Ernzerhof, M. Generalized gradient approximation made simple. *Phys. Rev. Lett.* **1996**, 77, 3865−3868.

(22) Suh, I.-K.; Ohta, H.; Waseda, Y. High-temperature thermal expansion of six metallic elements measured by dilatation method and X-ray diffraction. *J. Mater. Sci.* **1988**, 23, 757−760.

(23) Armentrout, M. M.; Kavner, A. A new high pressure and temperature equation of state of fcc cobalt. *J. Appl. Phys.* **2015**, 118, 194904.

(24) Kittel, C. *Introduction to Solid State Physics*, 8th ed.; John Wiley& Sons, Inc.: New York, 2005; p 52.

(25) Henkelman, G.; Uberuaga, B. P.; Jónsson, H. A climbing image nudged elastic band method for finding saddle points and minimum energy paths. *J. Chem. Phys.* **2000**, 113, 9901−9904.

(26) Marick, L. Variation of Resistance and Structure of Cobalt with Temperature and a Discussion of Its Photoelectric Emission. *Phys. Rev.* **1936**, 49, 831.

(27) Straumanis, M. E.; Aka, E. Z. Precision Determination of Lattice Parameter, Coefficient of Thermal Expansion and Atomic Weight of Carbon in Diamond. *J. Am. Chem. Soc.* **1951**, 73, 5643−5646.

(28) Ferrari, A. C.; Meyer, J. C.; Scardaci, V.; Casiraghi, C.; Lazzeri, M.; Mauri, F.; Piscanec, S.; Jiang, D.; Novoselov, K. S.; Roth, S.; Geim, A. K. Raman spectrum of graphene and graphene layers. *Phys. Rev. Lett.* **2006**, 97, 187401.

(29) Chatterjee, S.; Kim, N. Y.; Pugno, N. M.; Biswal, M.; Cunning, B. V.; Goo, M.; Jin, S.; Lee, S. H.; Lee, Z.; Ruoff, R. S. Synthesis of Highly Oriented Graphite Films with a Low Wrinkle Density and Near-Millimeter-Scale Lateral Grains. *Chem. Mater.* **2020**, 32, 3134－3143.

(30) Brandes, E. A.; Brook, G. B. *Smithells Metals Reference Book*, 6th ed.; Butterworth-Heinemann, **1992**; Vol. 13, p 23.

(31) Iijima, Y.; Makuta, F.; Agarwala, R. P.; Hirano, K. Diffusion of Carbon in Cobalt. *Mater. Trans., JIM* **1989**, 30, 984－990.

(32) Ruf, M.; IJspeert, M.; van Dam, S.; de Jong, N.; van den Berg, H.; Evers, G.; Hanson, R. Optically Coherent Nitrogen-Vacancy Centers in Micrometer-Thin Etched Diamond Membranes. *Nano Lett.* **2019**, 19, 3987－3992.

(33) Kara, V.; Sohn, Y.-I.; Atikian, H.; Yakhot, V.; Loncˇar, M.; Ekinci, K. L. Nanofluidics of Single-Crystal Diamond Nanomechanical Resonators. *Nano Lett.* **2015**, 15, 8070－8076.

(34) Field, D. E.; Cuenca, J. A.; Smith, M.; Fairclough, S. M.; Massabuau, F. C.-P.; Pomeroy, J. W.; Williams, O.; Oliver, R. A.; Thayne, I.; Kuball, M. Crystalline Interlayers for Reducing the Effective Thermal Boundary Resistance in GaN-on-Diamond. *ACS Appl. Mater. Interfaces* **2020**, 12, 54138－54145.

(35) Cui, S.; Greenspon, A. S.; Ohno, K.; Myers, B. A.; Jayich, A. C. B.; Awschalom, D. D.; Hu, E. L. Reduced Plasma-Induced Damage to Near-Surface Nitrogen-Vacancy Centers in Diamond. *Nano Lett.* **2015**, 15, 2887－2891.

IV. Summary

The role of catalysts in modern industry is becoming more and more important day by day. Through the first-principles DFT calculations, understanding how catalysts work is also important for catalyst rational design. As stated in this dissertation, detailed descriptions of thermodynamic changes and surface dynamics can identify the reasons for unlikely reactions to occur. The advantage of DFT calculation in catalyst research is that it can reveal the physical origins that affect the catalytic activity and stability that determine catalyst performance.

In this study, it was revealed that the d_{xy} down spin orbital center level of the surface B-metal and the 2p band center of the lattice oxygen determine the performance of perovskite as an OER electrocatalyst using cheap 3d transition metal. Through our findings, a new surface electronic descriptor was proposed (E_{2p} – 0.4 E_{dxy}), and the possibility of utilizing it for catalyst design by extending the descriptor was suggested.

Based on Nudged Elastic Band (NEB) simulation, the activation energies of catalyst reactionss were performed to understand the catalyst's ability to contribute to the synthesis of materials. We were able to calculate the activation energies of chemical reactions occurring on the Ni and Co surface or interface and specify the reaction rate-determining step. We discovered a Ni-C surface exchange mechanism that allows diamond to dissolve into Nickel.

Acknowledgements

박사학위 과정동안 받은 많은 도움과 지지에 감사드립니다.

먼저, 많이 부족한 저를 박사과정기간동안 지도해주시고 올바른 연구의 방향으로 이끌어 주신 이근식 지도교수님께 감사의 말씀을 전하고 싶습니다. 지도교수님의 지도와 도움으로 연구하는 동안 중요한 것들을 알게 되었으며, 연구의 기쁨과 의미를 알도록 하셨습니다. 이근식 교수님의 적극적인 가르침과 열심 덕분에 지난한 연구의 과정을 무사히 마칠 수 있었습니다. 저도 은사님의 가르침을 바탕으로 이후의 삶의 과정 속에서도 발전하는 연구자가 되도록 노력하겠습니다.

아울러, 제 박사 학위 심사에 응해주시고 좋은 조언들을 해주신 김광수 교수님, Rodney S. Ruoff 교수님, 민승규 교수님, 김명종 교수님께도 감사의 말씀을 전합니다.

연구를 하면서 함께 동고동락한 박인기, 문진홍, 김은미에게도 감사를 전하며, 저의 연구에 도움을 주셨던 하미란 박사님, Mohammad Zafari, Rohit Anand, 김태인, 하종권, 이인성에게도 감사드립니다. Computational Lab for Innovative Materials 에서 함께 보냈던 시간들은 저의 삶에 있어서 값진 시간이었고, 잊지 못할 추억이 될 것입니다.

마지막으로, 제가 장성하여 학업을 이어 나가고 박사학위를 마치기까지 정말 많이 사랑하는 부모님, 김환수, 최미병 두 분이 보내주신 지지와 도움에 감사를 전할 수 있게 되어 너무 기쁩니다. 제가 박사학위를 마치기까지 아낌없는 격려와 지지를 보내준 사랑하는 우리 형과 우리 동생, 김용선, 김화원에게도 감사를 전하고 싶습니다.

그리고 제가 울산에 와서 어렵고 힘든 박사과정의 기간을 해볼 만한 것으로 즐거운 것으로 만들어준 사랑하는 최혜진에게도 감사의 말을 전하며, 제가 이 곳에 와서 무사히 학위를 마치고 새로운 사람들을 만나고 앞날을 꿈꾸도록 인생의 의미 있는 것들로 저의 시간들을 채우게 하신 하나님께 저의 감사가 전해지기를 소망하며 글을 줄입니다.

List of Publications

1. **Yongchul Kim**, Miran Ha, Rohit Anand, Mohammad Zafari, Jeong Min Baik, Hyesung Park, Geunsik Lee*, "Unveiling a Surface Electronic Descriptor for Fe-Co Mixing Enhanced the Stability and Efficiency of Perovskite Oxygen Evolution Electrocatalysts", *ACS Catal*. **2022**, 12, XXX, 14698–14707.
2. Hee Jun Kim, Sang Heon Kim, Sun-Woo Kim, Jin-Kyeom Kim, Chentian Cao, **Yongchul Kim**, Ungsoo Kim, Geunsik Lee, Jae-Young Choi, Hyung-Suk Oh, Hyun-Cheol Song, Won Jun Choi, Hyesung Park, Jeong Min Baik, "Low-temperature crystallization of LaFeO3 perovskite with inherent catalytically surface for the enhanced oxygen evolution reaction", *Nano Energy*. **2022**, 11, 108003.
3. Taehyung Kim, Sungho Choi, Jaegeon Ryu*, **Yongchul Kim**, Geunsik Lee, Byeong-Su Kim*, and Soojin Park*, "Surficial Amide-enabled Integrated Organic Anode–Binder Electrode for Electrochemical Reversibility and Fast Redox Kinetics in Lithium–Ion Batteries", *Applied Surface Science*. **2022**, 601, 154220.
4. Mengran Wang, **Yongchul Kim**, Liyuan Zhang, Won Kyung Seong, Minhyeok Kim, Shahana Chatterjee, Meihui Wang, Yunqing Li, Pavel V. Bakharev, Geunsik Lee*, Sun Hwa Lee*, Rodney S. Ruoff*, "Controllable electrodeposition of ordered carbon nanowalls on Cu(111) substrates", *Materials Today* **2022**, 57, 75-83.
5. Jihyung Seo, **Yongchul Kim**, Junghyun Lee, Eunbin Son, Min-Hyoung Jung, Young-Min Kim, Hu Young Jeong,* Geunsik Lee,* and Hyesung Park*, "A single-atom vanadium-doped 2D semiconductor platform for attomolar-level molecular sensing", *J. Mater. Chem. A*, **2022**,10, 13298-13304.
6. Yunqing Li, **Yongchul Kim**, Pavel V. Bakharev, Won Kyung Seong, Chohee Hyun, Dulce C. Camacho-Mojica, Liyuan Zhang, Benjamin V. Cunning, Tae Joo Shin, Geunsik Lee*, and Rodney S. Ruoff*, "Dissolving Diamond: Kinetics of the Dissolution of (100) and (110) Single Crystals in Nickel and Cobalt Films", *Chem. Mater*. **2022**, 34, 6, 2599–2611.
7. Taehyung Kim, Se Hun Joo, Jintaek Gong, Sungho Choi, Ju Hong Min, **Yongchul Kim**, Geunsik Lee, Eunji Lee, Soojin Park, Sang Kyu Kwak, Hee-Seung Lee, and Byeong-Su Kim*, "Geomimetic Hydrothermal Synthesis of Polyimide-Based Covalent Organic Frameworks", *Angew. Chem. Int. Ed.* **2022**, 61, e202113780.
8. Gyujeong Jeong, Jihyung Seo, **Yongchul Kim**, Dong-Hyun Seo, Jeong Min Baik*, Eun-chae Jeon*, Geunsik Lee*, and Hyesung Park*, "Graphene Antiadhesion Layer for the Effective Peel-and-Pick Transfer of Metallic Electrodes toward Flexible Electronics", *ACS Appl. Mater. Interfaces*. **2021** 13, 18, 22000–22008.
9. Yeonjeong Koo, **Yongchul Kim**, Soo Ho Choi, Hyeongwoo Lee, Jinseong Choi, Dong Yun Lee, Mingu Kang, Hyun Seok Lee, Ki Kang Kim, Geunsik Lee, Kyoung-Duck Park*, "Tip-Induced

Nano-Engineering of Strain, Bandgap, and Exciton Funneling in 2D Semiconductors", *Adv. Mater*. **2021**, 2008234.

10. Sun-Woo Kim, U Jeong Yang, Jae Won Lee, Fredrick Kim, **Yongchul Kim**, Geunsik Lee, Jae Sung Son*, and Jeong Min Baik*, "Triboelectric Charge-Driven Enhancement of the Output Voltage of BiSbTe-Based Thermoelectric Generators", *ACS Energy Letters*. **2021**, 6, 3, 1095-1103.

11. Palas Baran Pati, Eunji Jin, Yohan Kim, **Yongchul Kim,** Jinhong Mun, So Jung Kim, Seok Ju Kang, Wonyoung Choe, Geunsik Lee*, Hyung-Joon Shin*, Young S. Park*, "Unveiling 79-Year-Old Ixene and Its BN-Doped Derivative", *Angew. Chem. Int. Ed*. **2020**, 59, 35, 14891-14895.

12. Ungsoo Kim, Yongjoon Cho, Dasom Jeon, **Yongchul Kim**, Sanghyeon Park, Jihyung Seo, Junghyun Lee, Nam Khen Oh, Geunsik Lee, Jungki Ryu*, Changduk Yang*, Hyesung Park*, "Zwitterionic Conjugated Surfactant Functionalization of Graphene with pH-Independent Dispersibility: An Efficient Electron Mediator for the Oxygen Evolution Reaction in Acidic Media", *Small*. **2020**, 16, 1906635.

13. Jihyung Seo, Junghyun Lee, **Yongchul Kim**, Donghwan Koo, Geunsik Lee, Hyesung Park*, "Ultrasensitive Plasmon-Free Surface-Enhanced Raman Spectroscopy with Femtomolar Detection Limit from 2D van der Waals Heterostructure", *Nano Lett*. **2020**, 20, 1620.

14. Youngsin Park, Christopher C. S. Chan, Robert A. Taylor*, **Yongchul Kim**, Nammee Kim, Yongcheol Jo, Seung W. Lee, Woochul Yang, Hyunsik Im*, and Geunsik Lee*, “Temperature induced crossing in the optical bandgap of mono and bilayer MoS_2 on SiO_2”, *Sci. Rep*. **2018**, 8, 5380.